Biomimetic Functionalization of SiO_2 Surfaces by Membranes Supported on Polymeric Tethers

Christian Daniel

Technische Universität München
Physik Department
Lehrstuhl für Biophysik E22

Biomimetic Functionalization of SiO_2 Surfaces by Membranes Supported on Polymeric Tethers

Christian Daniel

Vollständiger Abdruck der von der Fakultät für Physik der Technischen Universität München zur Erlangung des akademischen Grades eines

Doktors der Naturwissenschaften (Dr. rer. nat.)

genehmigten Dissertation.

Vorsitzender:	Univ.-Prof. Dr. R. Netz
Prüfer der Dissertation:	1. Univ.-Prof. Dr. E. Sackmann
	2. Univ.-Prof. Dr. J. O. Rädler, Ludwig-Maximilians-Universität München

Die Dissertation wurde am 29.06.2010 bei der Technischen Universität München eingereicht und durch die Fakultät für Physik am 13.07.2010 angenommen.

Meinen Eltern

Table of Contents

Fange nie an aufzuhören, höre nie auf anzufangen.

aus dem Volksmund

Zusammenfassung

Die vorliegende Arbeit umfasst im Wesentlichen zwei Teile: Der erste Teil befasst sich mit einer neuen Methode zur biomimetischen Funktionalisierung von Siliziumoberflächen mittels Modellmembranen auf Polymerstützen und der strukturellen Charakterisierung dieser Oberflächen. Der zweite Teil der Arbeit, der einen erheblichen Teil der Zeit in Anspruch genommen hat, bestand aus experimentellen Aufbauarbeiten am Neutronenreflektometer mit Option zur Kleinwinkelstreuung REFSANS an der Forschungs-Neutronenquelle Heinz Maier-Leibnitz in Garching, das im Sommer 2005 erfolgreich in Betrieb genommen wurde.

Die Herstellung und Charakterisierung biomimetischer Festkörperoberflächen ist ein Forschungsgebiet der Biophysik das Anwendungen in der Biosensorik findet. Dabei werden Proteine, Zellbausteine oder ganze Zellen in möglichst nativem Zustand in die Nähe einer Festkörperoberfläche gebracht um dort Untersuchungen mit hoher Auflösung durchführen zu können. Typische Methoden sind dabei die Mikrointerferometrie (RICM), Ellipsometrie, Oberflächen Plasmonen Spektroskopie (SPR), Fourier Transform Infrarot Spektroskopie (FTIR), Kernspinresonanz (NMR) sowie Neutronen- und Röntgen Reflektometrie. Als Substrat werden oft Strom leitende Materialien aber auch Halbleiter eingesetzt. Ein bewährtes und vielseitig einsetzbares Substrat ist Silizium dessen Oberfläche unter biologisch relevanten Bedingungen zu Siliziumdioxid oxidiert. Eine Aufgabe dieser Arbeit war es, SiO_2 Oberflächen, wie sie auch bei Glas vorzufinden sind, so zu funktionalisieren, dass der Einfluss der Rauhigkeit und anderer Oberflächenwechselwirkungen auf Biomoleküle in nm Entfernung reduziert wird und darüberhinaus diese Funktionalisierung mittels oberflächensensitiver Methoden zu charakterisieren.

Der Bedarf einer verbesserten SiO_2 Oberfläche wurde exemplarisch an einer Untersuchung des Einflusses von molekularen Motoren (Myosin V) auf Aktinfilamente, die in der Natur als Fortbewegungsbahnen solcher Motoren vorkommen, nachgewiesen. Dabei wurde gezeigt, dass Motoren, die über eine übliche direkte Anbindung an die Oberfläche gebunden waren, Aktinfilamente auseinanderreissen konnten. Durch Verbesserung der Verankerung an der

Oberfläche, d.h. Motoren wurden in einer fluiden zweidimensionalen Lipidmembran über ein mobil verankertes Bindungselement gebunden, wurden solche Risse nicht mehr induziert und somit wurden wesentlich längere Untersuchungszeiten möglich, siehe Appendix I.

Der Kern dieser Arbeit besteht in der Entwicklung einer Modellmembran die auf kovalent gebundenen Polymerstützen in einer Entfernung von 7–8 nm von der Oberfläche stabil und fluide ist. Die Oberfläche unter der Lipiddoppelschicht konnte dabei ebenfalls mit kovalent gebundenen Polymeren unterschiedlicher Länge passiviert werden. Diese schrittweise Funktionalisierung ermöglicht die Herstellung einer substratgestützten Modellmembran, die zur Oberfläche hin wassergefüllte Zwischenräume aufweist, eine Eigenschaft die bei Untersuchungen transmembraner Proteine von Vorteil ist. Eine so funktionalisierte Oberfläche kann darüberhinaus nach Aufreinigung und erneuter Aufbringung der Lipiddoppelshicht wiederholt verwendet werden. Die Charakterisierung der einzelnen Schritte der Funktionalisierung sowie eine Analyse der hergestellte Modellmembran sind im Hauptteil in Kapitel 1–3 im Detail beschrieben und wurden bereits publiziert [Daniel et al., 2007].

Die experimentellen Arbeiten an REFSANS, d.h. der zweite Teil der Arbeit, ergaben erste Kalibrationsmessungen der Abstrahlcharakteristik eines torsierten Neutronenleiters sowie die Inbetriebnahme und Justage des Instruments und wurden zum Teil publiziert [Kampmann et al., 2004], [Zeitelhack et al., 2006] und [Kampmann et al., 2006], siehe Appendix II–IV. Auf Grund technischer Schwierigkeiten war es im Rahmen dieser Arbeit jedoch nicht mehr möglich mit diesem Instrument weiterführende Experimente durchzuführen. Im folgenden Abschnitt wird daher lediglich ein Überblick dieser mit erheblichem Zeitaufwand verbundenen experimentellen Aufbauarbeiten gegeben.

REFSANS ist ein hochauflösendes Reflektometer mit Option zur Kleinwinkelstreuung, das zur Untersuchung horizontaler Proben entworfen und insbesondere für Experimente an gas-flüssig Grenzflächen optimiert wurde. Das Instrument ist darüberhinaus auch vorteilhaft einsetzbar zur Analyse unterschiedlicher weicher oder fester Proben, die z.B. einen Flüssigkeitsaustausch erforderlich machen oder deren experimentelles Protokoll aus anderen Gründen horizontale Geometrien vorsieht. Eine solche spezielle Probenumgebung kann erst durch Beugung des einfallenden Neutronenstrahls zum Einsatz kommen, wofür ein über eine

Länge von ca. 12 m variables Neutronenleitersystem nötig ist. Auf der Detektionsseite kann ein zweidimensionaler Detektor, der über eine Länge von 2–12 m weit verfahrbar ist, die Messung von Impulsüberträgen in einem extrem weiten Inervall von ca. 0.01-10 nm^{-1} bewerkstelligen. Als Flugzeitspektrometer, das Neutronen der kalten Quelle mit Wellenlängen im Bereich von 0.2–3 nm mit einstellbarer Auflösung bereitstellt, ermöglicht REFSANS damit die gleichzeitige Untersuchung lateraler und vertikaler Strukturen im nm-µm Bereich. Dazu werden Reflektometrie- und Kleinwinkelstreuungsexperimente entweder gleichzeitig durchgeführt oder es werden für spezielle Anforderungen unterschiedliche Geometrien des Instruments so eingestellt, dass die Probe dabei nicht verstellt werden muss, ein Vorteil der insbesondere für Untersuchungen an weicher Materie zum Tragen kommt. Die Vielseitigkeit des Instruments erforderte eine langjährige Planungs- und Herstellungsphase der einzelnen Komponenten, die am Institut für Werkstoffforschung GKSS in Geesthacht durchgeführt wurde.

Im Rahmen dieser Arbeit wurde die Aufbauphase von REFSANS in der Neutronenleiterhalle des Forschungsreaktors FRM-II der Technischen Universität München begleitet. Dabei standen zunächst hauptsächlich organisatorische Aufgaben im Vordergrund, wie z.B. zur Einrichtung dazugehöriger Arbeitsplätze in Büro und Halle oder Auststattung des Labors. Anlieferungen der Bauteile des Instruments über mehrere Monate erforderten eine zeitaufwendige Koordination von Lagerung und Aufbau in der Neutronenleiterhalle. Ein erheblicher Teil der Arbeit befasste sich darüberhinaus mit der Anpassung technischer Details des Instruments die erst während Montage und Justage notwendig wurden, die in Zusammenarbeit mit Werkstätten und externen Firmen durchgeführt wurden. Es wurden z.B. verschiedene Vakuumanschlüsse der Kammern an den Neutronenleiter und die Pumpstation entworfen und gebaut, elektrische Verkabelungen der verfahrbaren Neutronenoptik durchgeführt oder unvorhergesehene Vibrationen im Chopperbereich reduziert. Im Probenraum wurde ein Filmwaagenaufbau, ein Goniometeraufbau mit einer flexiblen Probenumgebung sowie die Softwaresteuerung dazu konzipiert und in Funktion genommen. Schliesslich wurde die Abschirmung erfolgreich aufgebaut und das Instrument konnte den Strahlenschutzbestimmungen entsprechend in Betrieb genommen werden.

Abstract

The present work covers two parts: A first part deals with a new method of biomimetic functionalization of silicon surfaces with model membranes supported on polymeric tethers and with the structural characterization of these surfaces.
The second part, that required a substantial part of the time, dealt with experimental work on assembling the neutron reflectometer with option for small angle scattering REFSANS at the scientific neutron reactor Heinz Maier-Leibnitz in Garching near Munich, which successfully went operational.

Introduction and Motivation

Design of biofunctional systems on solid surfaces is a modern fascinating field in Biological Physics. A selfassembled lipid bilayer on a solid support is one meanwhile classical example of such systems which has been investigated for more than 30 years now. The lipid bilayer model of cell envelopes represents a two dimensional fluid matrix which is suitable for incorporation of proteins, see Figure 1, and also for immobilizing cells under biomimetic conditions.

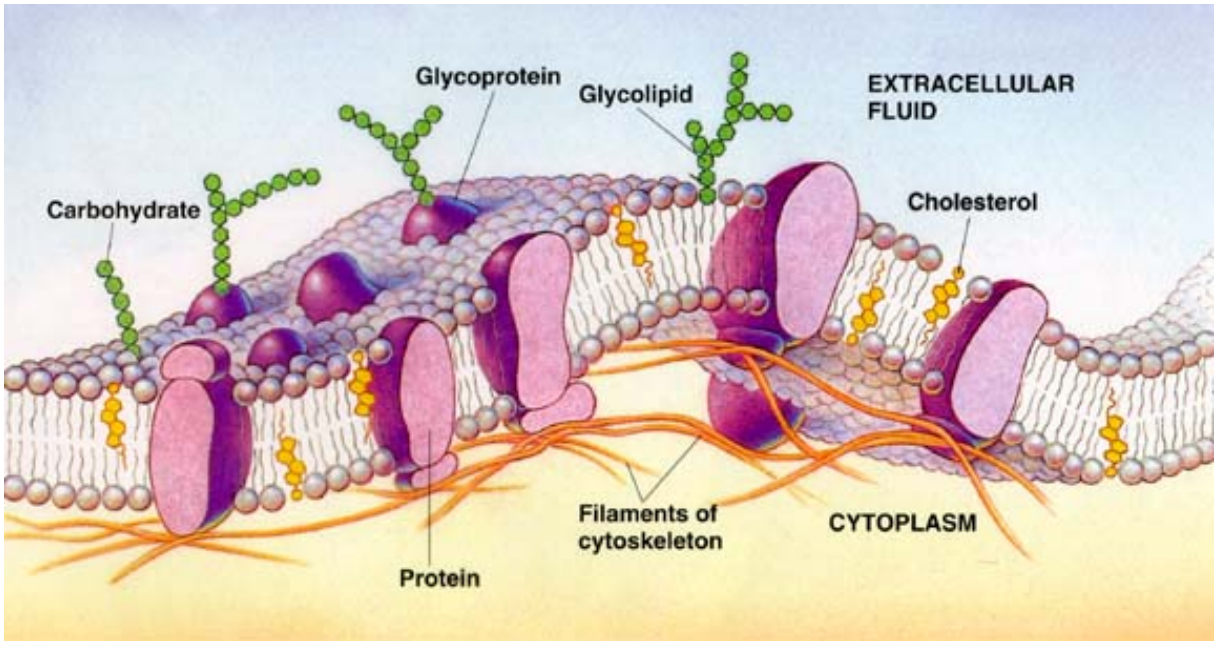

Figure 1 Model of a cell membrane separating the inside of a cell from the extracellular space. Main constituents are lipids, cholesterol, proteins, carbohydrates and actin filaments [Campbell et al., 1999].

On solid surfaces, such model can provide a convenient platform for investigations of biofunctional molecules like proteins or DNA under bioanalogue conditions. Modern more sophisticated systems additionally include enzymatic machineries or ultrathin polymeric cushions in the vicinity of substrates and lipid membranes. The characterization and the

understanding of the self assembly of such complex supported membranes represent current challenges in a field bridging solid state physics and biological physics [Sackmann, 1996]. Applications owe for example towards biomimetic solid surfaces for high throughput proteomics of different sized proteins. The work presented here has been driven by the need of such biofunctional systems which enable investigations by different high resolution surface analysis methods.

The formation of biomimicking surfaces benefits from the combination of molecular genetic engineering with biochemistry, for example by using large molecules for separating bio-analogue complexes from solid inorganic biomolecule-denaturating surfaces. These new possibilities include the design of chimeric systems by combining molecules composed of biologically and chemically functional parts to be coupled to membranes and solid surfaces respectively. The formation of soft cushion supported membranes based on such chimeric molecules is expected to become an effective bottom up approach for engineering biomimicking surfaces because together with other membrane constituents, see Figure 2, they bear the potential to be suited as a toolbox for constructing biofunctionalized surfaces with specific functions on demand.

There are numerous open biophysical questions with respect to such models of the cell surface. Among others these refer to two dimensional organization of biomolecules under non equilibrium conditions or to physical aspects of cell adhesion and cell growth. Furthermore, similar heterostructured systems fabricated on length scales between nanometer and micrometer are of increasing interest since they constitute per se a subject of science of interfaces. These multipurpose samples furthermore enable the application of advanced surface sensitive analyzing methods like surface scattering techniques or surface plasmon resonance spectroscopy for characterization of structure and functionality of interfaces. They are furthermore essential for the design of modern electro-optical biosensing devices, for example employing single or arrays of precisely localized point transistors, quantum dots or microcavities. They can therefore help to develop novel approaches for the development of analytical methods and can furthermore open new fields of research and application including new strategies for materials design.

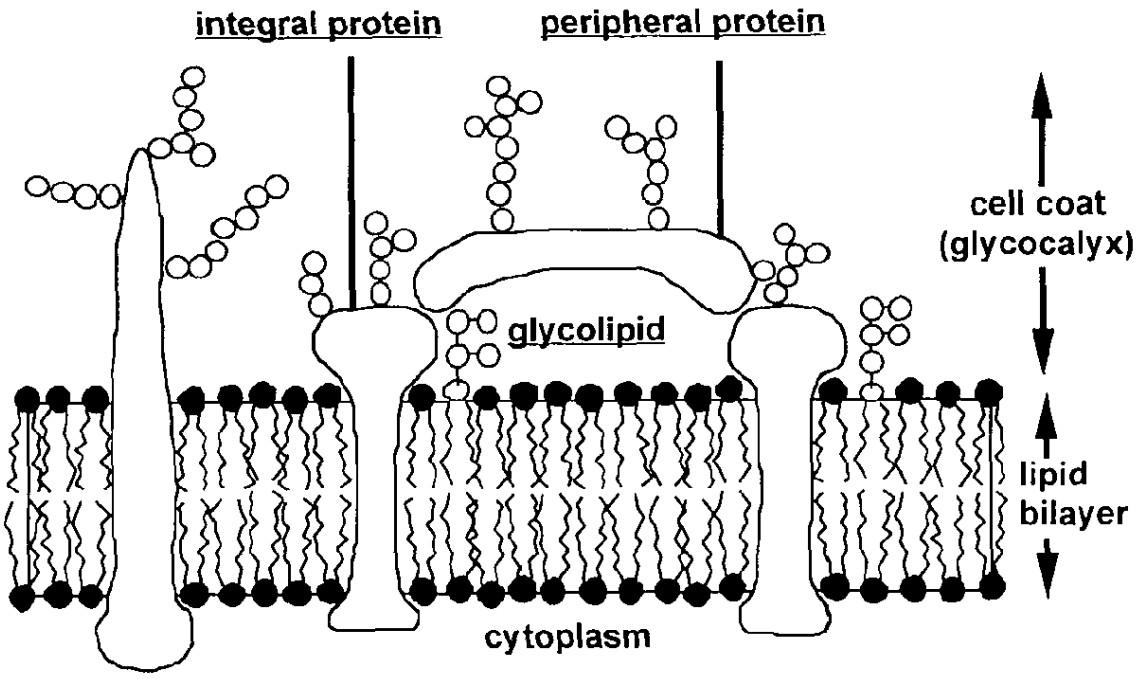

Figure 2 Schematic representation of a constructional model typically envisaged when designing experiments mimicking cell membranes: a lipid bilayer with integral proteins. Sugar moieties and peripheral proteins are attached thereto forming the glycocalyx, the outside part of the membrane [Jossinet et al., 1995].

The present work reports a novel technique for the fabrication of such a biomimicking surface, namely of tethered lipid membranes on passivated silicon oxide devices. The lipid bilayers were separated from the solid surface by an ultra-thin soft polymer cushion that could mimick the extracellular matrix or the actin cortex thereby providing improved model cell membranes. As a template, a SiO_2 surface was functionalized with PEG-lipid tethers under mild conditions and further reacted with polyethyleneglycol (PEG) making available a biologically passivated substrate of variable tether density and flexible cushion height. Adding lipids to this functionalized surface resulted in the formation of fluid tethered membranes, which are continuous over large areas.

Further, data are presented on actin dynamics in two-dimensional motility assays on fluid, solid-supported lipid membranes, as an example of well functioning enzymatic protein machineries on planar surfaces. Molecular motors (Myosin V) were coupled to the membranes via monoclonal antibodies specific to a defined region of the myosin rod which does not interfere with the motor and/or ATPase activity. By using lipidated Fab fragments of

these antibodies, single double-headed motor molecules Myosin V were anchored in the lipid membrane without intermolecular cross-linking. Thus, it was possible to observe and analyze the two-dimensional dynamics of single actin filaments driven by mobile anchored molecular motors for long observation times in the order of minutes. It is demonstrated that mobile molecular motors are functional under this bioanalogue condition.

Alltogether various results related to improved biofunctionalization of solid surfaces are summarized. First, experimental results about actin dynamics driven by molecular motors anchored in fluid lipid membranes are presented, which were obtained in the biophysical laboratory E22 of the Technical University Munich in collaboration with Junshan Zhang. As early experiments merely demonstrating the need for improved biofunctionalized surfaces, they can be found in Appendix I. Second, partially motivated by these results, a new tethered lipid membrane for advanced protein analysis was developed and characterized in collaboration with Luisa Andruzzi and Bert Nickel from the Ludwig Maximilians University Munich. The development and characterization of this new system constitutes the main part of the present thesis, see Chapters 1–3. Third, an unique experimental facility for the investigation of biomaterials on surfaces by neutron scattering techniques has been constructed at the neutron reactor facility “FRM-II” in Garching in collaboration with the REFSANS team from the GKSS Forschungszentrum Geesthacht. At the time of completion of the experimental part of this work, no experiments could be conducted at REFSANS to characterize the new tethered lipid membrane system due to different technical difficulties. However, first standard experiments based on different calibration measurements had been performed, parts of which have been published, see Appendix II–IV.

Chapter 1
Materials and Methods

This chapter presents an overview of all materials and methods used in this study. Further details particularly relevant when presenting experimental results are being given in the following chapters, when deemed appropriate in the context. For example, while all chemicals used are being included here below, certain details on buffers are mentioned in the next chapter dealing with the surface functionalization. Similarly, while a general introduction on reflectometry is being given here below, some details on experimental settings and analysis steps appear more relevant when discussing data in the third chapter. The reader interested in repeating the experimental procedures is recommended to additionally consult the citations mentioned, for example manufacturers data sheets or literature reviews on methods, as these give up to date information and a broader methodological background respectively.

1.1 Chemicals

Lipids and polymers

Zwitterionic 1-stearoyl-2-oleoyl-sn-glycero-3-phosphocholine (SOPC) lipids and amino-terminated poly(ethyleneglycol)-functionalized 1,2-distearoyl-sn-glycero-3-phosphoethanol-amine lipo-polymers (NH_2-PEG_{45}-DSPE), herein also called PEG-lipids, were purchased from Avanti Polar Lipids, Inc. (Alabaster, USA), see Figure 1.1. Amino-terminated poly(ethyleneglycol) (NH_2-PEG_n, n=17, 45), herein also called PEG750 and PEG2000 according to their molecular weight were purchased from Nektar (Huntsville, USA), whereas fluorescently labeled lipids 2-[12-(7-nitrobenz-2-oxa-1,3-diazol-4-yl)amino]dodecanoyl-1-hexadecanoyl-sn-glycero-3-phosphocholine (NBD-PC) were purchased from Molecular Probes (Leiden, Netherlands) and were all used without further purification.

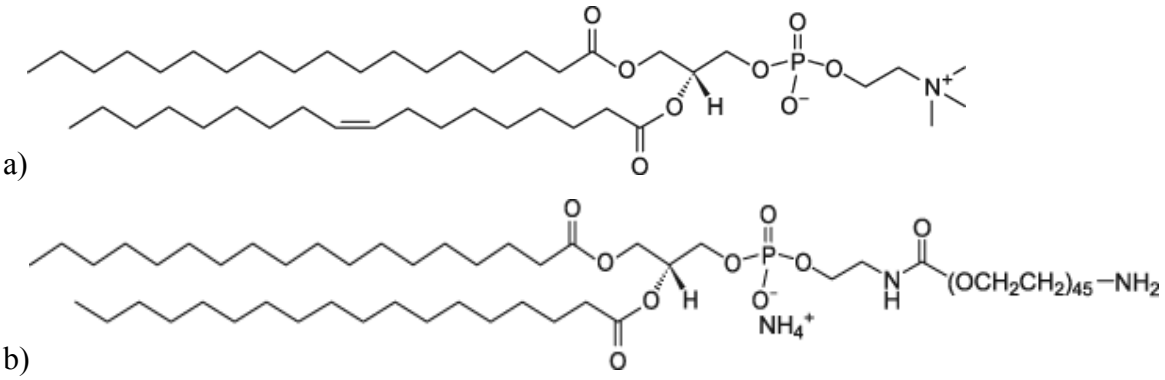

Figure 1.1 Chemical structures of two constituents: (a) 1-stearoyl-2-oleoyl-sn-glycero-3-phosphocholine (SOPC) and (b) 1,2-distearoyl-sn-glycero-3-phospho-ethanolamine-N-[amino-(polyethylene glycol)-2000] (NH_2-PEG2000-DSPE).

Solvents and others

The water used throughout this study, also for cleaning, was de-ionized ultra pure water from a Millipore purification system (specific resistivity 18.2 MW cm, Millipore Corp., Billerica, USA). Anhydrous hexadecane, anhydrous dimethylformamide (DMF), 1-ethyl-3-[3-(dimethylamino)propyl]carbodiimidehydro-chloride (EDC), and N-hydroxysuccinimide (NHS) were purchased from Sigma-Aldrich (Munich, Germany) and octenyltrichlorosilane (OTS) with 90 % vinyl group content was purchased from abcr GmbH (Karlsruhe, Germany) and were all used without further purification.

1.2 Substrate

Silicon wafers, 20x15 mm^2, polished and thermally annealed to form a SiO_2 layer of about 100 nm, were purchased from Holm Siliciumbearbeitung (Tann, Germany). The wafers were cleaned using a modified RCA method, thereby removing organic and metal contaminants [Kern & Puotinen, 1970] and forming OH-groups at the SiO_2 surface:

- immersion in a $NH_4OH/H_2O_2/H_2O$ (1/1/4 by volume) solution at 80 °C for 10 min
- rinsing with deionized water
- immersion in a $HCl/H_2O_2/H_2O$ (1/1/4 by volume) solution at 80 °C for 10 min
- rinsing with deionized water
- immersion in a $NH_4OH/H_2O_2/H_2O$ (1/1/4 by volume) solution at 80 °C for 10 min

The wafers were flushed with nitrogen and dried in a vacuum oven at 120 °C for 5 min directly after the cleaning procedure and, within half an hour, used for further functionalization, see Chapter 2, Scheme 2.1.

1.3 Lipid bilayer deposition

Lipid bilayers on solid surfaces were prepared by deposition from a solution of lipid vesicles, i.e. three dimensional self assembled lipid bilayer shells. First, lipids and fluorescently labeled lipids were disolved in chloroform in a molar ratio of 1:0,005. Then, solvent was evaporated under a fume hood with a stream of dry nitrogen and the remaining sample subsequently stored in a vacuum chamber for at least 12 hours to further remove the solvent. The flask with the dry lipid film sample was then hydrated to a concentration of about 1 mg/ml and a vesicle solution was obtained by incubating it at 40 °C for 2 hours while repeated vortexing. To reduce the vesicle size, two different approaches were used and proved effectual for the later deposition. The vesicle solution was either sonicated for 10 min with a tip sonicator and subsequently centrifuged or was extruded 11 times using a Mini-Extruder with a polycarbonate filter of a pore size of 100 nm from Avanti Polar Lipids, Inc. (Alabaster, USA). After injection of the vesicle solution in the chamber, see chamber setup below, and incubation for about 1 hour, lipid bilayers formed on the solid surface by vesicle fusion. As a final step, the chamber was flushed at least five times with pure water to remove remaining vesicles from the bulk solution.

1.4 Experimental setup

During development of the new tether supported membrane an experimental setup was needed to implement Optical Microscopy experiments for verification of the membrane after deposition and for later characterization of the surface functionalization, the setup at the same time being suitable for high resolution reflectometry experiments, see Figure 1.2.

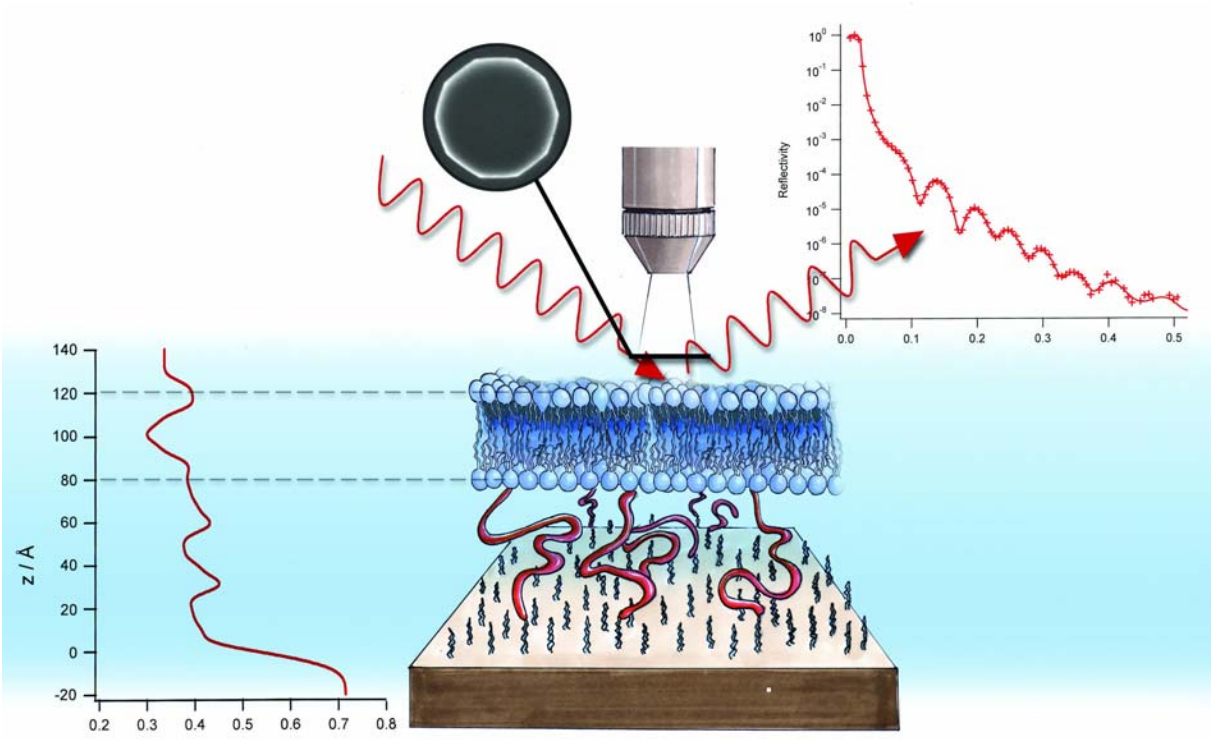

Figure 1.2 Sketch of the experimental setup for characterizing the functionalized surface by reflectivity and microscopy measurements.

1.4.1. Microfluidic chamber setup

The chamber setup used for the characterization of the functionalized surfaces by Fluorescence Microscopy and X-ray Reflectometry is illustrated in Figure 1.3. It has been developed in a previous work by [Reich et al., 2005] in colaboration with Ibidi GmBH (Munich, Germany) and is optimized for this kind of experiments.

Briefly, the chamber material is a rigid thermoplatic polymer (Topas Cyclo Olefin Coplymer a trademark of Ticona GmbH, Fankfurt, Germany) with a low mass density of 1.02 g/cm^3 thereby providing low attenuation for X-rays while being optical transparent. The chamber design includes a microfluidic channel (volume of 50 µl, legth × width × height, 50 mm x 5 mm x 200 µm) which faces the bottom of the silicon wafer embedded within the plastic chamber. The channel is sealed by a thin foil (thickness of 200 µm) which together with the

small channel height permits optical observation of the functionalized surface using standard microscope objectives. A detailed description of the setup is given in [Reich et al., 2005a].

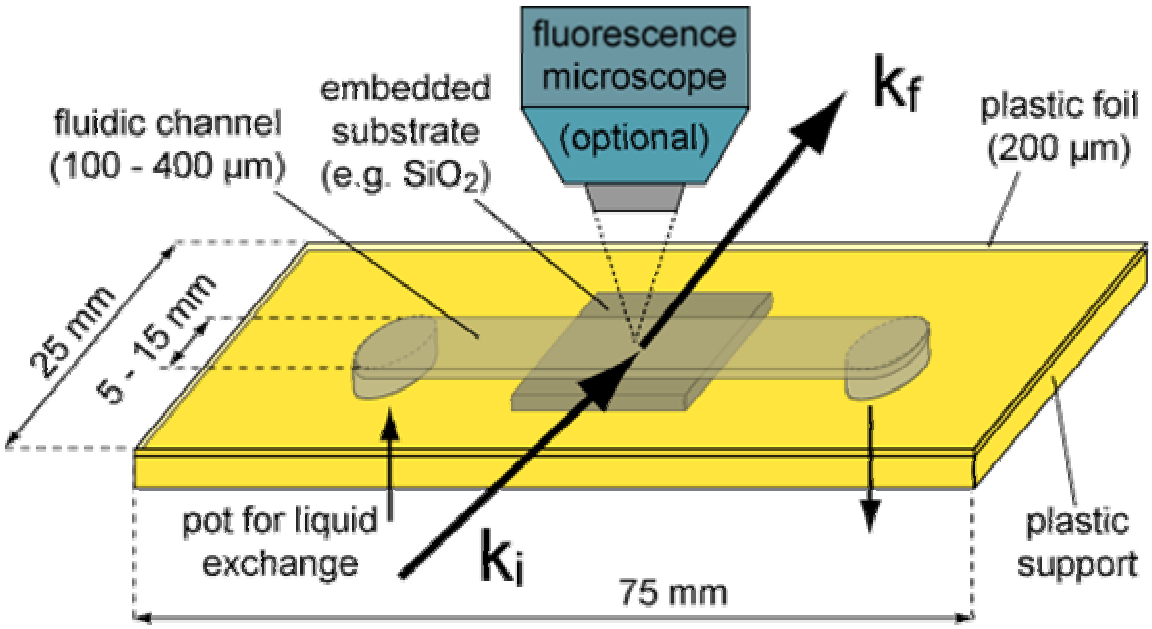

Figure 1.3 Microfluidic chamber setup. The functionalized surface under investigation, in this sketch the upper surface of the grey quadratic silicon wafer, can be hydrated and also further coated by exchanging fluids from left and right pos via the grey fluidic channel. A thin transparent plastic foil forms a sealing of the chamber and makes it suitable for both X-ray Reflectivity (ki, kf) and Optical Microscopy measurements [Reich et al., 2005a].

Traditionally, investigations of solid-liquid interfaces by means of diffraction techniques has been a domain of Neutron Reflectometry. In particular, X-ray scattering investigations of biomolecular samples under water suffer due to strong incoherent interactions of the beam with the aqueous environment, which leads to significant background scattering and beam attenuation. This problem could be reduced with the microfluidic chamber setup above, thereby opening the experimental possibility of utilizing highly brilliant X-ray beams offered by modern synchrotron sources for X-ray Reflectivity investigations with subnanometer resolution.

1.4.2 Fluorescence Microscopy setup

Fluorescence Microscopy was carried out on a portable Axiotech Vario Zeiss fluorescence microscope (Carl Zeiss AG, Oberkochen, Germany), equipped with a high pressure mercury lamp HBO 100 (Osram, Munich, Germany) and a cooled CCD camera Hamamatsu Orca (Hamamtsu, Herrsching am Ammersee, Germany) and an acquisition and image analysis software package Simple PCI (Hamamatsu Corporation, Sewikley, USA).

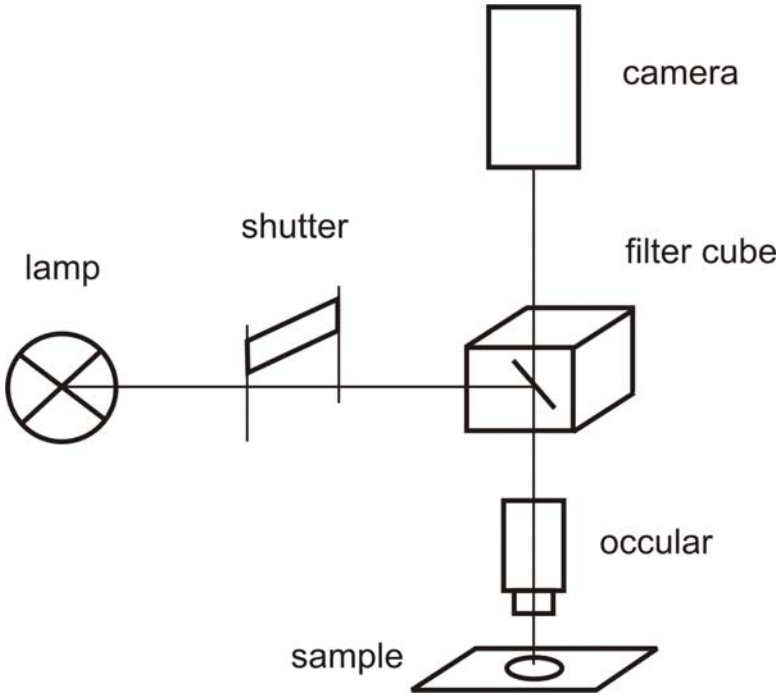

Figure 1.4 Setup of a typical Fluorescence Microscopy experiment.

The portable fluorescence microscope could be transported to the synchrotron facility and proved to be helpful for sample preparation before reflectivity measurements, i.e. to ascertain succesful bilayer deposition. The microscopy setup, although initially designed for direct implementation at a (neutron or x-ray) beamline sample stage, could obviously, for the studies presented here, also be used off-beamline because the compact microfluidic chamber, see Figure 1.3 above, could be easily transported from the preparation laboratory to the beamline experimental hall.

1.4.3 X-ray reflectometer

The X-ray Reflectometry experiments were carried out at the synchrotron beamline D4, see figure 1.5, at HASYLAB Hamburg. A beam energy of 19.9 keV was selected using a Si (111) monochromator, and the data were recorded with a fast scintillation detector Cyberstar (Oxford Instruments, Abingdon, UK).

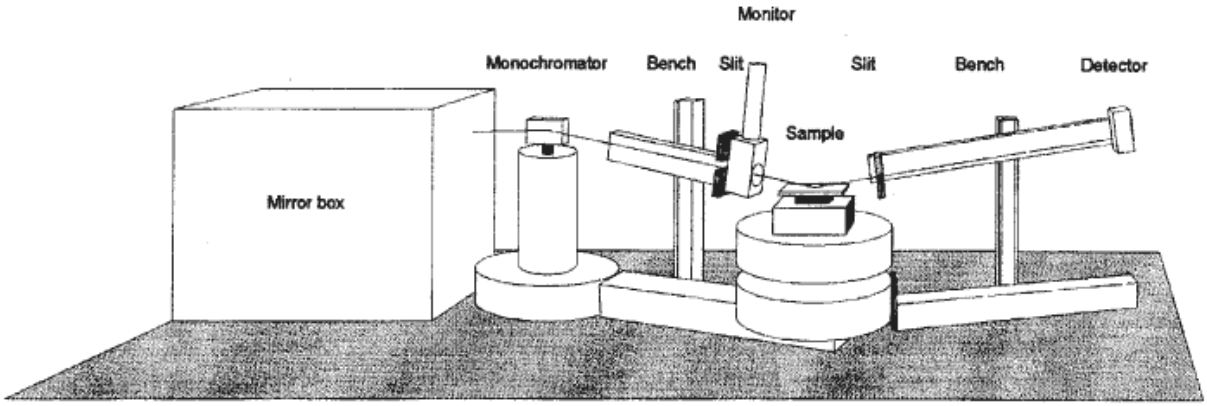

Figure 1.5 Sketch of the X-ray reflectometer at the synchrotron beamline D4 at HASYLAB Hamburg.

1.5 Methods

1.5.1 X-ray Reflectometry (XRR) measurements

The scattering method Reflectometry is widely known and has been reviewed repeatedly in the literature. For example, an extensive introduction and review on Reflectometry, using both the Fresnel's approach and the kinematic (Born's) theory, together with thorough discussions on measured reflectivity profiles of different surface functionalizations is given in [Penfold and Thomas, 1990]. The reader is also referred to [Gibaud & Hazra, 2000], giving an excellent introduction in the method of Specular X-ray Reflectometry and furthermore also elaborates on the analysis of surface roughness and diffuse scattering data.

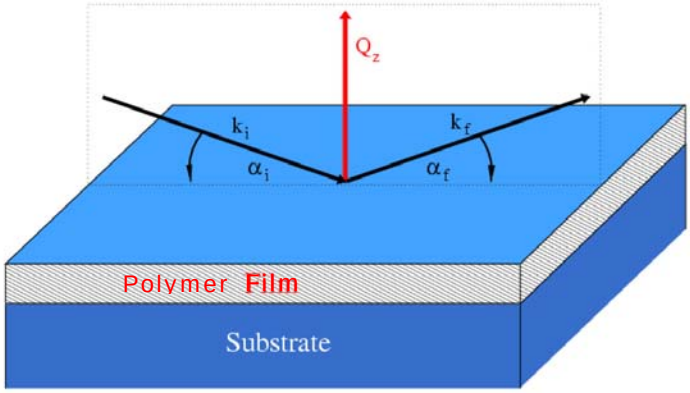

Figure 1.6 Geometry of a typical X-ray Reflectometry experiment. An incident beam (k_i) hits a surface under a small angle (α_i) and is reflected from the surface (k_f) under an angle (α_f) depending on the refractive indizes at the interface. Specular reflectivity measures the perpendicular momentum transfer (Q_z) in the case of equal angles ($\alpha_i = \alpha_f$). Reflections from multiple interfaces (air ↔ polymer film and polymer film ↔ substrate) interfer with each other exhibiting characteristic oscillations, which depend on the substrate's dimension and electron density.

Here, X-ray Reflectometry measurements, were carried out under ambient conditions and in excess water using a microfluidic device, see Section 1.4.1 above. Data were recorded in an intensity range comprising more than 8 orders of magnitude, the background level for all membrane experiments was reached at a reflectivity of $1e^{-8}$ and for samples measured under ambient conditions at $2e^{-10}$.

The reflectivity data were modeled with the software "Parratt32" (version 1.6) provided by Christian Braun from the Hahn-Meitner Institut (Berlin, Germany). The Parratt formalism [Parratt, 1954] based on Fresnel reflectivity uses a layered structure parallel to the surface with stacked slabs of fixed electron density. The spatial resolution, d_{min}, of these experiments can be estimated to be $d_{min} = \pi / q_{max} = 6.3$ Å [Pershan et al., 1994], where $q_{max} = 0.5$ $Å^{-1}$ is the maximum q-value up to which the reflectivity can be measured before it drops below background level. Consequently, slab sizes of 7 Å were used for the model fit to reconstruct the depth profiles of membrane reflectivity data superimposed by a Gaussian roughness of 2.5 Å.

1.5.2 X-ray Photoelectron Spectroscopy (XPS)

X-ray Photoelectron Spectroscopy (XPS), see for example [Moulder et al., 1992] for a review of the method, was performed in a collaboration with K.E. Sohn in the group of E.J. Kramer at UCSB (Santa Barbara, California) on a Kratos Axis Ultra Spectrometer (Kratos Analytical, Manchester, UK).

XPS was carried out in the C 1s region to determine the chemical groups formed close to surface during the different stages of the surface functionalization process using monochromated Al Kα x-rays at 1486 eV at 225W and low energy electrons for charge compensation, see Chapter 2.3 for further details. Spectra were collected at 40 and 80 eV pass energy using a hemispherical energy analyzer and a channel width of 0.05 eV.

1.5.3 Diffusion measurements with Fluorescence Microscopy

Fluorescence studies were done on the microscopy setup described above, see chapter 1.4.2, by using the fluorescently labelled lipids NBD-PC, see chapter 1.1, as a fluorescence probe in SOPC membranes in a molar ratio of 1:0,005. Diffusion constants of such lipids were measured by the Continuous Bleaching method introduced by [Dietrich et al., 1997].

Thereby, an area of fluorescently labelled lipids is continuously illuminated which results in photobleaching of the dye molecules and a continuous decrease in brightness. Diffusion of unbleached molecules from ouside the illuminated area into this area leads to formation of a concentration profile at the rim of the illuminated area. This concentration profile c(x,t) can be deduced from the diffusion equation extended by a photobleaching term:

$$c(x,t) = A(t) \cdot e^{-\frac{x}{\lambda}} + e^{-B_0 \cdot t},$$

where

$$\lambda = \sqrt{\frac{D}{B_0}}$$

is the characteristic decay length, D the diffusion constand and B_0 the bleaching rate.

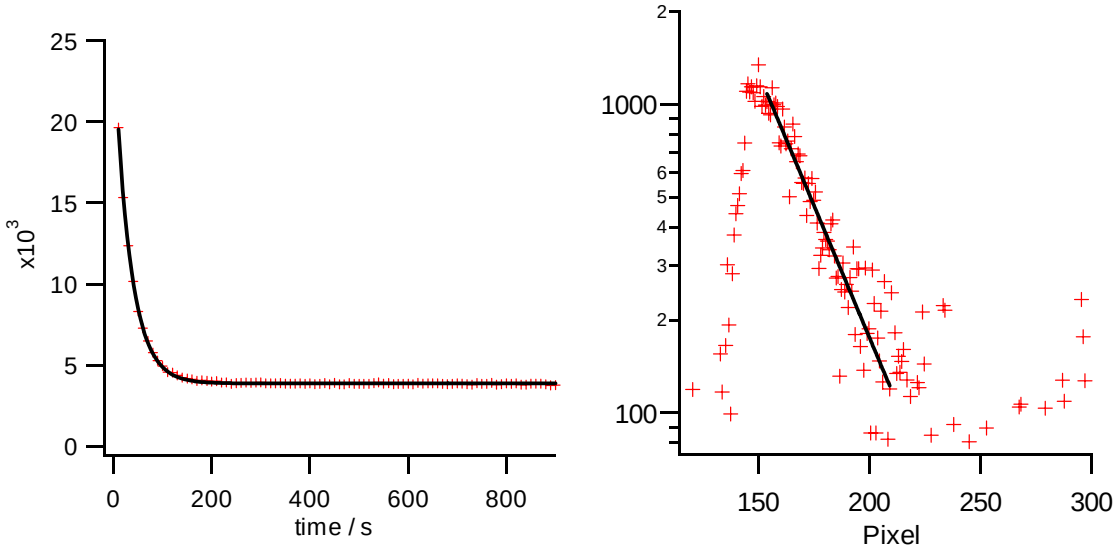

Figure 1.7 Data analysis steps on a representative sample, see text for further details.

The bleaching rate has been determined for each data set by an exponential fit to an average brightness decrease as a function of time at the center of the illuminated area during initial bleaching, see for example figure 1.7 left graph. The decay length has been determined by an exponential fit to the fluorescence decrease as a function of radius at the rim of the illuminated area after continuous bleaching, see for example figure 1.7 right graph.

Chapter 2
Surface Functionalization

2.1 Introduction

The properties of surfaces can be drastically changed by molecular monolayers which, although only a few nanometers thick, became of increasing interest for scientific and technical applications. Such monolayers can either be transferred to solid surfaces from air-water interfaces by the Langmuir-Blodgett (LB) technique or can be directly self-assembled at surfaces by chemisorption. Self-assembled monolayers (SAMs) of organosilanes chemisorbed from solution to SiO_2 surfaces provide highly ordered molecular platforms for further bottom-up nanofabrication.

Often, silanized polymers are directly used as surface reactive groups for immobilization onto oxide surfaces. Examples present in the literature include terpolymers containing a surface-reactive moiety and linear polymers as hydrophilic cushion in the side-chains [Seitz et al., 2000]. Tamm and co-workers reported on grafting a tripartite molecule consisting of a lipid attached to a poly(ethylene-glycol) molecule with a molecular weight of 3400 Dalton and bearing a silane reactive group for substrate attachment by LB transfer and thermal annealing [Kiessling et al., 2003]. Similarly, Purrucker and co-workers [Purrucker et al., 2004] reported grafting of 2-methyl-2-oxazoline based lipopolymers using LB transfer followed by thermal annealing to induce covalent coupling of the silane to the surface. More recently, Atanasov and co-workers has grafted a short tetra(ethylene-glycol)-lipid to an oxide surface without LB transfer [Atanasov et al., 2005]. In all cases, membrane proteins have been successfully embedded in the membranes. However, these approaches have in common that the silanization process is being performed directly with macromolecules, e.g. lipopolymers, which bears the disadvantage of steric hinderance at the surface binding site and is

furthermore not compatible with a true bottom up approach for engineering the first few nanometers above the surface.
In some cases, the functionalization has been divided in two steps; first a silane based surface modification was employed to provide a reactive group which is functionalized in a second step by the lipopolymer. For example, Shen and co-workers first modified an oxide surface by benzophenone and, in a second step, a lipid-containing poly(2-ethyl-2-oxazoline) has been grafted to this surface by photo-crosslinking [Shen et al., 2001]. However, such approaches require harsh experimental conditions, e.g. UV-light or strong acidic solvents, which limit the variety of macromolecules possibly used for the functionalization. A similar two step strategy has been employed for gold substrates; in a first step a thiopeptide was chemisorbed to a gold surface, and in a second step, its COOH terminus was activated and DMPE lipid was covalently linked forming a thiopeptide-tethered lipid monolayer [Bunjes et al., 1997]. Since the terminal COOH group is not stable as such over a silanisation process, this strategy can not be directly applied on oxide surfaces. Therefore a new strategy to overcome these difficulties had to be developed.

Here, in an optimized three step synthesis (see Chapter 2.2) it was possible to activate a carboxilated SAM under mild conditions and selectively couple to silicon dioxide surfaces either PEG-lipid tethers or pure PEG-polymers or a combination of both via covalent bonds. To optionally condense the lipopolymeric film laterally, unreacted COOH groups were further coupled to PEG polymers of variable chain length (PEG750, PEG2000), a process denoted backfilling.

This novel design principle allows to activate oxide surfaces for surface-tethered fluid lipid membranes. It benefits from the possibility to functionalize “pockets” between continuous elevated membranes and surfaces which can be used to host transmembrane proteins for sophisticated protein analysis at surfaces. This represents a significant improvement over supporting the membrane on bare silicon oxide or on a continuous cushion layer. A further advantage of this functionalization strategy for elevating a membrane above the surface is, that tether density and spacer length can be controlled, thereby making it possible to tune mechanical properties of the membrane [Seifert et al., 2006] and to further improve its ability to host transmembrane proteins.
The characterisation of the chemical bonds by X-ray Photoelectron Spectroscopy (XPS) and the investigation of films by X-ray reflectivity for their structure are presented in Chapter 3.

2.2 Surface chemistry

Self assembled monolayers (SAMs) were used to graft amphiphilic molecules (lipopolymers) and polymers directly to a SiO_2 surface as anchoring platform for a lipid membrane. The step by step assembly of the PEG/PEG-lipid film is summarized in Scheme 2.1. Startingly, octenyltrichlorosilane (OTS or VTS[†]) was chemisorbed to a silicium dioxide surface using silane coupling (Scheme 2.1b)). In a subsequent three step synthesis, the vinyl group (-CH=CH_2) of the OTS-SAM was oxidized by permanganate-periodate resulting in a carboxyl-group (COOH) functionalization of the free SAM terminus (Scheme 2.1c)). Secondly, the COOH group was activated using N-hydroxysuccinimide (NHS) resulting in an amide bond stable towards hydrolytic cleavage but capable of prompt reaction with amino-terminated molecules (Scheme 2.1d)). In the last step, it was possible to selectively couple different aminoterminated PEG_{45}DSPE (2) or PEG_n (n=17, 45) polymers (1) to the NHS modified surface of SAM under mild conditions (buffer solution $NaHCO_3/HCO_3^-$ at pH=8,5). In the Scheme 2.1e) three different outcomes of this condensation has been presented *e) left:* PEG-polymers, *e) right:* PEG-lipid tethers and *e) bottom:* mixed PEG-lipid tethers and PEG-polymers layer surface ("backfilling"). PEG-lipid tethers surfaces Scheme 2.1 *e) right* have been prepared at both low and high concentrations of amino-terminated PEG_{45}-lipid.
The NHS chemistry has proven to be a useful tool in organic chemistry for producing chemical bonds under mild conditions [Bunjes et al., 1997]. It allows for the formation of amide and ester bonds between carboxylic and amino or hydroxyl groups even at room temperature in aqueous solution.

A diploma thesis evolved from the work presented here, [Hertrich, 2008], which includes further sketches of each step and pictures of laboratory equipment together with parameter settings employed, see pages 3–9 and 15 therein, and is therefore recommended for the reader interested in details of the surface functionalization procedure.

Contact angle measurements with water as wetting liquid were performed on the samples to check how the wettability of the surface changed after the various stages of the synthesis. The

[†] The terminal vinyl group (V) together with the second functional part trichlorosilane (TS) has given the molecule another trivial name VTS, which disregards the actual length of the hydrophobic tail of the molecule. The only SAM used throughout this work is octenyltrichlorosilane (OTS), however due to easier literature citation and disscussion, the more common name VTS is sometimes used.

advancing and receding contact angles of VTS were 90º and 78º respectively, whereas the advancing and receding contact angles for oxidized VTS were 35º and 20º in agreement with values previously reported in the literature [Li et al., 2002]. The advancing and receding contact angles for VTS-PEG and VTS-PEG-lipid surfaces were about 30º and 19º respectively for both, which is attributed to the presence of the PEG at the surface.

X-ray Photoelectron Spectroscopy (XPS) analysis was carried out on PEG and PEG-lipid thin films to characterize the chemical groups formed in the near-surface region after each step of the synthesis, see Chapter 2.3.

Scheme 2.1

Synthesis of Surface-Tethered PEGs and PEG-lipids.

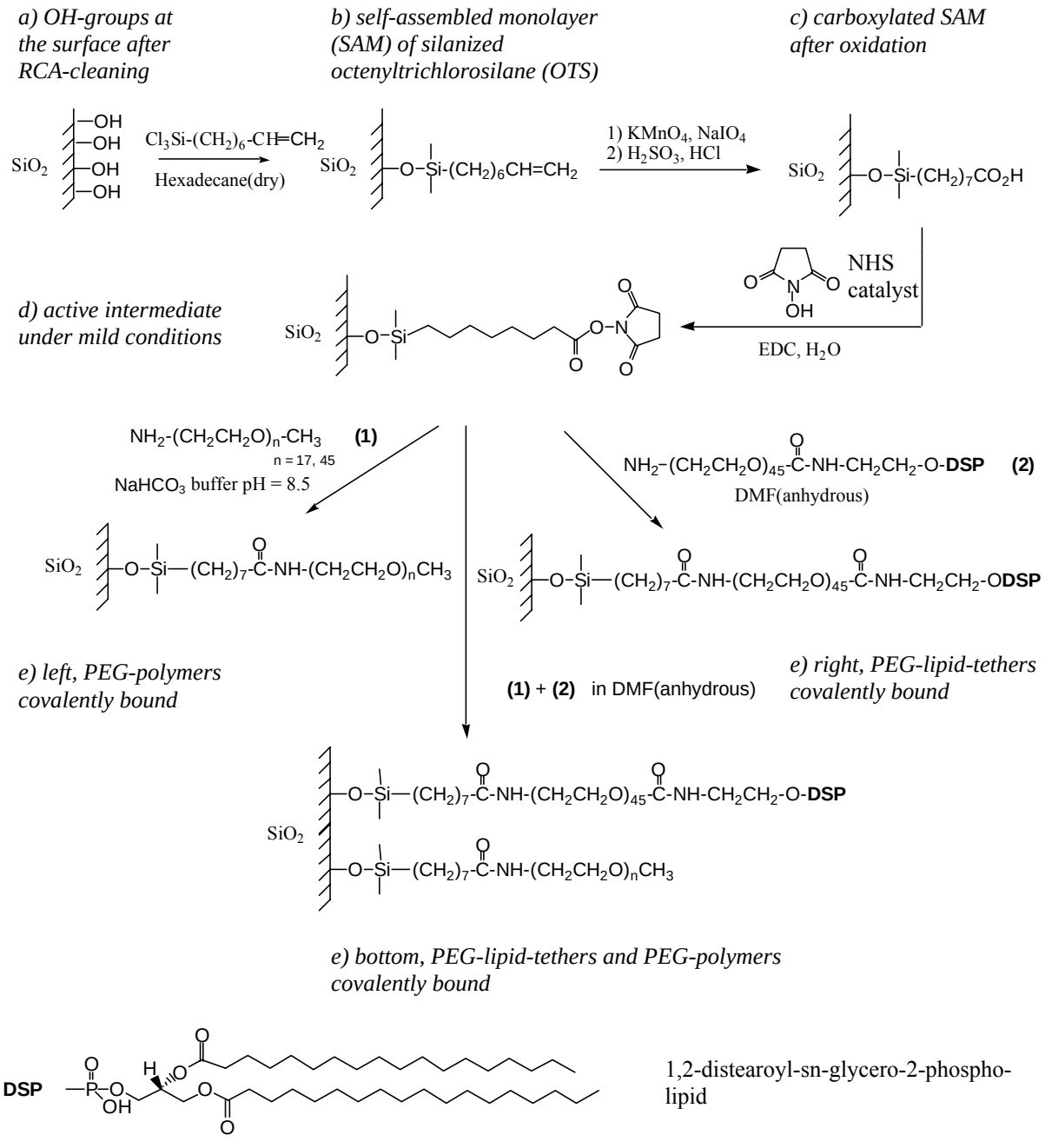

2.3 X-ray Photoelectron Spectroscopy (XPS) results

High resolution X-ray Photoelectron Spectroscopy (XPS) was done in collaboration with Karen E. Sohn from the Department of Materials, UCSB (Santa Barbara, California). XPS was carried out in the C 1s region to determine the chemical groups formed close to surface during the different stages of the synthesis process. The binding energy of the 1s electrons depends on the different bonding environments for the carbon atoms, which are hence detectable by XPS. Table 2.1 shows the expected binding energies for the relevant carbon bonds.

Table 2.1

XPS Binding Energies of the 1s electrons near the Carbon Ionization Edge.

Bond	Binding Energy (eV)
C-C	285
C-O-C	286.5
O=C-O	289.2

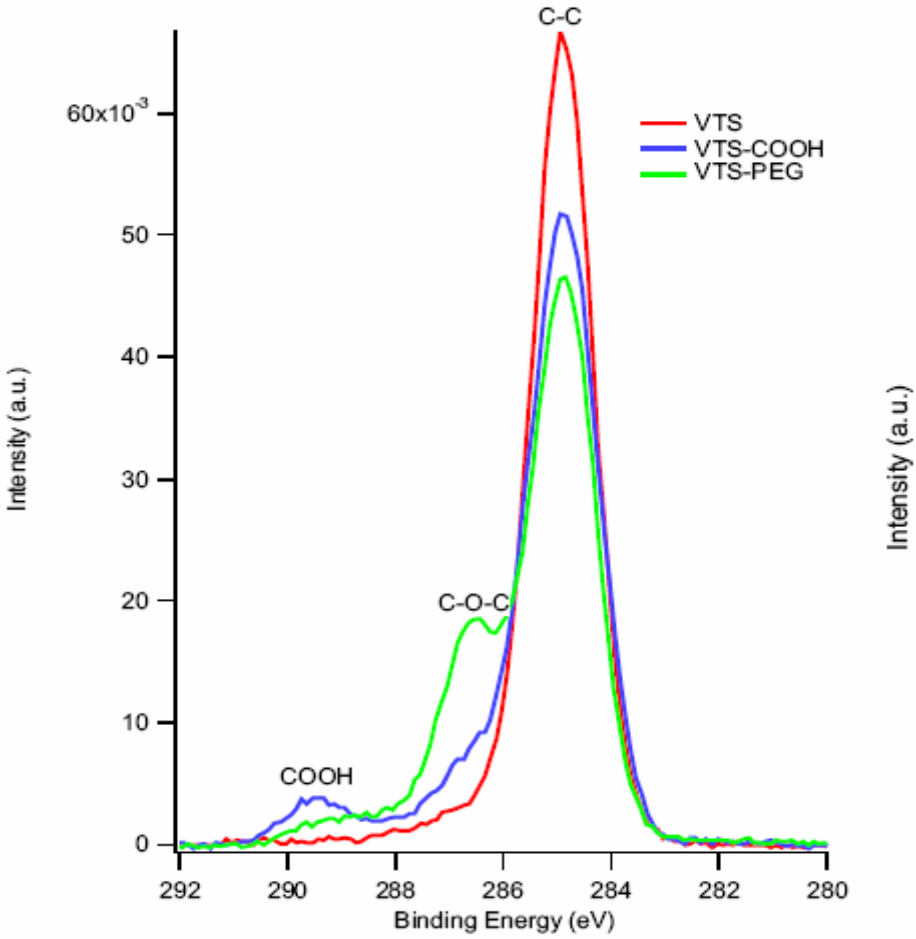

Figure 2.1 XPS data proving the functionalization scheme, i.e. the conversion of the VTS vinyl group to COOH and then the addition of the PEG750. Not all of the carboxyl groups were converted to the NHS derivative, indicated by the small COOH peak in the XPS of the PEGylated sample.

Figure 2.1 shows high resolution scans of the C 1s signal of dry VTS, VTS-COOH and VTS-PEG750 samples. The VTS sample shows an intense peak at 285 eV due to C-C bonds whereas oxidized VTS shows an additional peak at 289.5 eV due to COOH groups. PEG-functionalized VTS shows main peaks at 286.5 eV due to C-O-C bonds and at 285 eV due to the C-C bonds. It also shows an additional small peak at 289.5 eV due to residual terminal COOH groups that most likely had not reacted because of the large size and steric hindrance of the amino-terminated PEG molecules.

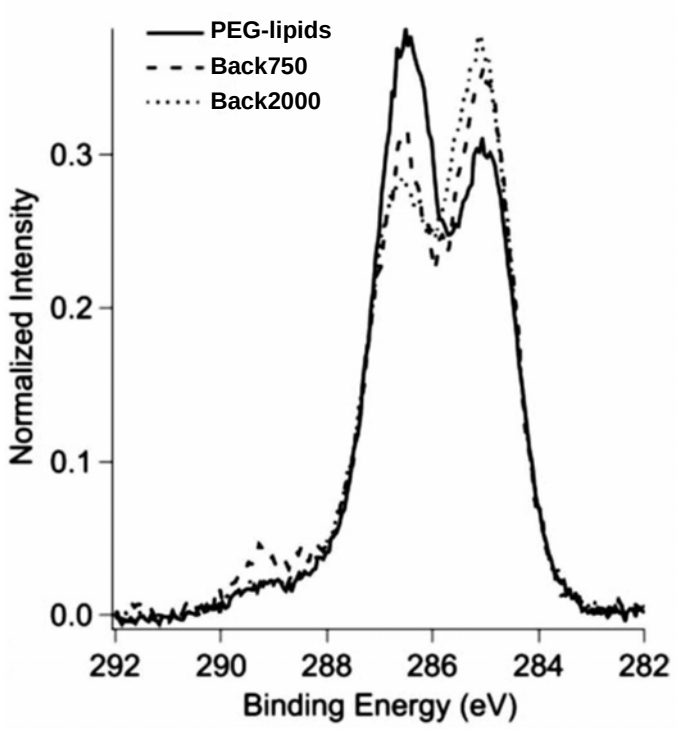

Figure 2.2 High resolution scan of functionalized surfaces: PEG-lipid tethers (continuous line), additionally "backfilled" with PEG750 (dashed) and PEG2000 (dotted) polymers, denoted as Back750 and Back2000.

Figure 2.2 shows high resolution scans of the C 1s signal of dry VTS-PEG-lipid_LC (low coverage), Back750 and Back2000 (further densified with PEG750 and PEG2000 respectively) samples. The VTS-PEG-lipid_LC sample shows an intense peak at 286.5 eV due to the C-O-C bonds along the PEG2000 chain and an additional peak at 285 eV caused by the C-C bonds in the lipid chains and VTS. When the samples were condensed with PEG750 and PEG2000 molecules, a shift was seen in the intensity of the two main peaks. The C-C peak increases relative to the C-O-C peak indicating that the extra molecules are causing the lipid chains to stand up, exposing more alkyl groups at the surface. This trend is in agreement with X-ray reflectivity data presented below in the text. However, the Back2000 sample still has a higher C-O-C peak than the Back750 sample, which is expected due to the larger number of C-O-C bonds in the higher molecular weight PEG molecules. These two findings are an indication that the uppermost surface is constituted from a mixture of upstanding lipids and passivating polymer moieties.

2.4 X-Ray Reflectivity (XRR) of the surface in ambient conditions

2.4.1 VTS-PEGylated (PEG2000 and PEG750)

In order to generate different PEGylated reference samples, two silicon wafers have been functionalized with PEG2000 and PEG750 polymers. Their normalized reflectivity data as a function of the scattering vector are shown in Figure 2.3a) the upper curve representing the data of the sample functionalized with PEG2000 and the lower curve representing the data of the sample functionalized with PEG750. For better visualization, the reflectivity data are plotted as R/q^{-4} to account for the Fresnel-decay at high q-values and the second curve is divided by a factor of 10. The reflectivity graphs of the functionalized surfaces show at least two pronounced local minima which implies a layered structure of the samples (Kiesig fringes). All data were analyzed using the Parratt formalism [Parratt, 1954] where the electron density profiles, Figure 2.3b), were modeled by boxes of different thicknesses and electron densities. The rounded steps of the profiles resulted from varying roughnesses between the boxes. The electron density graph also shows, as a reference, a measured profile of a bare silicon wafer with a roughness of 4.7 Å represented by a dashed line.

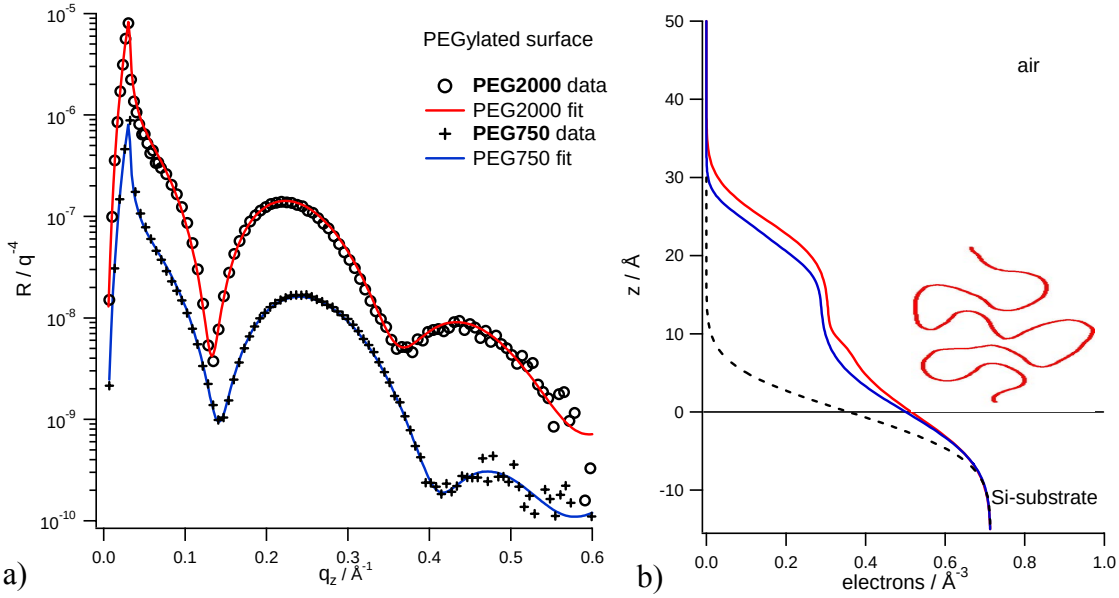

Figure 2.3 (a) XRR fringes in air of VTS-PEG2000 (upper curve) and VTS-PEG750 (lower curve, shifted), and (b) electron density profiles for VTS-PEG2000 and VTS-PEG750 and sketch.

The position of the first minimum of the PEG2000 film appears at a slightly lower q-value than of the PEG750 film, as expected for a thicker film. The corresponding electron density profile clearly shows the somewhat thicker layer of PEG2000.

The shorter molecules PEG750 deposit as a layer of (22 ± 5) Å thickness which is about equal to their Flory Radius (20 Å), indicating that this surface is covered with polymers in the mushroom regime. On the other side, for PEG2000, a thickness of (25 ± 5) Å is smaller than the corresponding Flory Radius (35 Å), which means these polymers are more likely in a collapsed mushroom conformation.

These results show that the grafting density, i.e. the number of molecules per surface, of PEG750 molecules is higher than of PEG2000. This capability of PEG750 molecules to graft at higher grafting density than PEG2000 molecules, possibly even more so than PEG2000 lipopolymeric molecules, is likely the reason for the lipid tails to be pushed upward, out of the lipopolymeric film, after the backfilling procedure, a squeezing out effect as discussed further below.

2.4.2 High and low PEG2000-DSPE tether grafting density

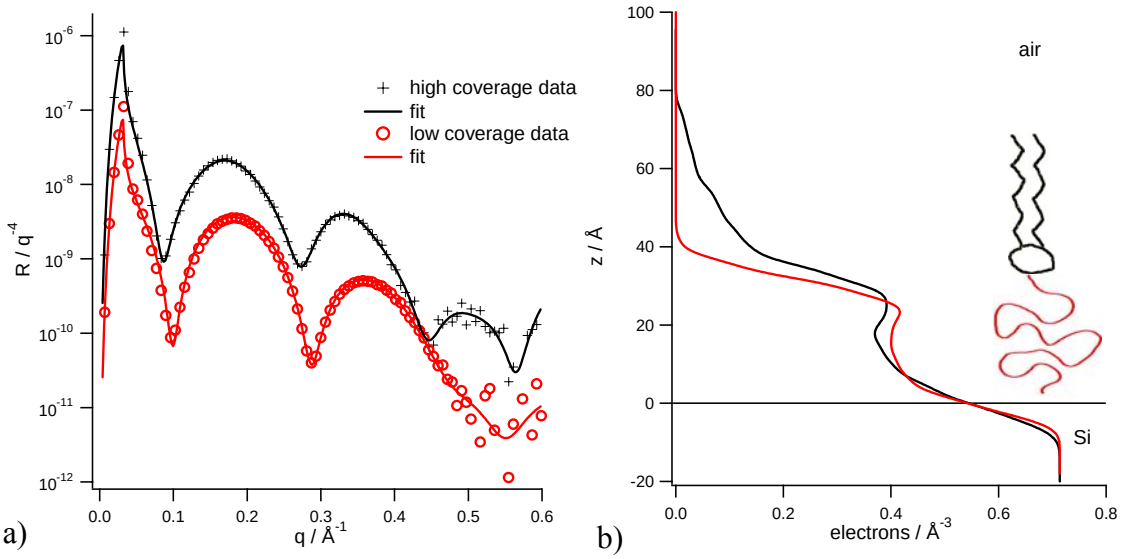

Figure 2.4 (a) XRR data of PEG2000-DSPE lipopolymers in air prepared from high (upper curve) and low (lower curve, shifted) concentration solutions and (b) corresponding electron density profiles for high concentration and low concentration samples and sketch.

Reflectivity data of surfaces functionalized with PEG2000-DSPE lipopolymers at low concentration and at high concentration are shown in Figure 2.4a). The electron density profile of the low concentration sample, Figure 2.4b) lower curve, shows that this surface layer is thicker (by about 1 nm) than the pure PEG2000 polymer functionalized surface, as discussed above (see Figure 2.3). The higher density sample data, Figure 2.4.a) upper curve, has a first minimum at a lower q-value than the lower density sample data, Figure 2.4a) lower curve, and even gives rise to a third oscillation at about 0.5 $Å^{-1}$. The higher concentration sample hence exhibits additional electron density in the region beyond $z > 40$ Å providing evidence that more material is bound to the substrate.
The higher extend of the electron density for PEG2000-DSPE compared to PEG2000 is due to the electrons of the lipid moieties. For the low concentration sample they can not be distinguished explicitly from the polymer moiety. On the other side, the additional electron density at the high concentration sample is a clear indication of lipids which are exposed above the PEG region. This hydrophobic tails at the surface of the deposited layer are expected to help the formation of flat lipid bilayers by vesicle spreading since they can serve as first pinning points for vesicles and at the same time be flexible tethers for growing bilayers.

These results also show that the low concentration PEG2000-DSPE surface is not fully covered and that therefore there is free space available at the surface which allows for further functionalization of the unreacted surface sites with PEG in a subsequent reaction, denoted backfilling.

2.4.3 Low PEG2000-DSPE tether grafting density subsequently backfilled with PEG750 and PEG2000 polymers

Figure 2.5 shows the reflectivity plots of surfaces functionalized with a low concentration of PEG2000-DSPE lipopolymers and subsequently backfilled with PEG2000 and PEG750 polymeric molecules. The curves look similar and both electron density profiles show an intensity increase in the region beyond $z > 40$ Å above the surface. For the PEG2000 sample, a lower intensity profile appears in the PEG region ($z < 30$ Å).

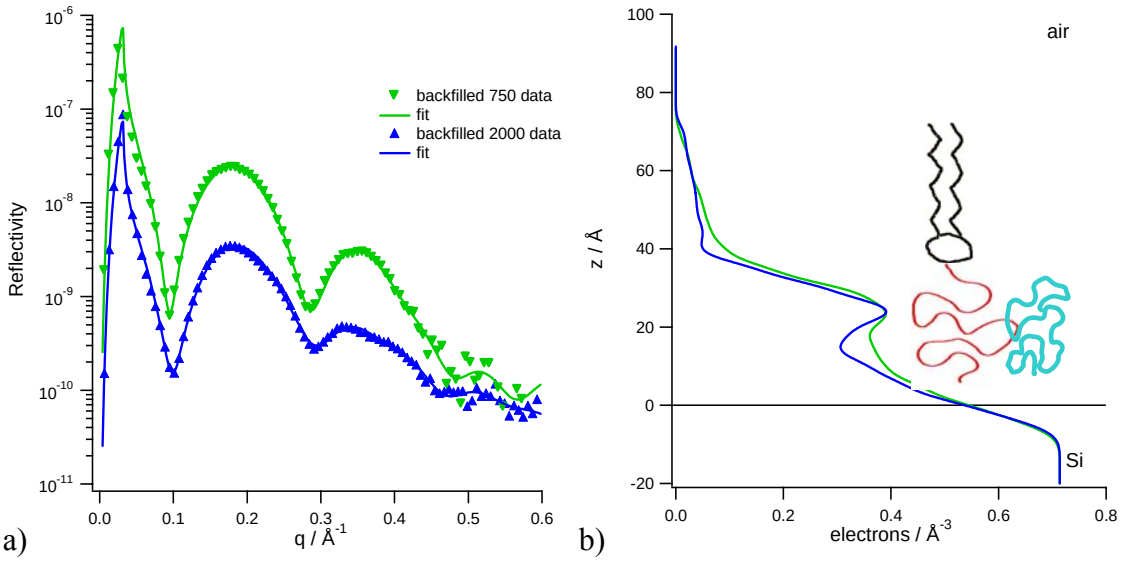

Figure 2.5 (a) XRR fringes observed in air for the case of low concentration PEG2000-DSPE lipopolymers samples backfilled with PEG750 (upper curve) and PEG2000 (lower curve, shifted), and (b) corresponding electron density profiles and sketch of the model fit.

After the process of backfilling, lipids can be observed on top of the surface, as in the case for the high coverage sample of pure lipopolymers (see Figure 2.4b)). This proves the potential of the backfilling process to cause lipid tails to stand up above the PEG-layer. Interestingly, this effect can not only be observed for backfilling polymers of the same length than the tethers (PEG2000) but also for shorter ones (PEG750). Hence, underneath lipid bilayers deposited on such surfaces, potentially more space free of polymers will be available when backfilled with shorter backfilling polymers than tethers, forming "water pockets" for incorporation of transmembrane proteins.

A process of backfilling was generally done at high concentrations and for extended periods of time to allow for saturation of the surface. It is also clear, that less PEG2000 polymers bind to the surface than the sterically favoured PEG750, as can be seen from the electron density profile Figure 2.5b) in the region 0–30 Å, which is consistent with the findings from the samples which were functionalized with pure polymers as discussed above with reference to Figure 2.2. As a result more lipids are being "squeezed out" for the shorter backfilling polymer, appearing in the electron density profile (Figure 2.5b)) above 40 Å.

2.5 Discussion

The aim of these studies under ambient conditions was to characterize lipopolymeric films obtained by stepwise functionalization of self-assembled monolayers and to determine the potential of the "backfilling" approach for advanced membrane applications.

The overall thickness of pure lipopolymeric layers, see Figure 2.4b), corresponds well to similar DSPE-PEG-layers bound to a gold surface as measured by ellipsometry (40 ± 1 Å) by [Munro et al., 2004]. [Elender et al., 1996] reported the thickness of the PEG-moiety, without lipids, of a physisorbed DSPE-PEG layer after Langmuir-Blodgett transfer (at 25 mN/m) to be about 25 Å in ambient conditions as measured by ellipsometry on a SiO_2 surface. This is in good agreement with data presented in Figure 2.3b) and in Figure 2.4b) showing the PEG region below 30 Å.

On the other side, here the lipid region could be determined first by the fact that additional electron density profile was measured above the PEG region only at lipopolymeric samples and not above the simple polymeric samples. Second, also the mentioned "squeezing out" effect, which explains why high coverage samples and backfilled samples have additional electron density above the PEG region while low coverage samples do not, is an ascertaining pointer for the assignment of lipids to this part of the electron density profile. Other workers, [Bolze et al., 2002], determined the thickness of DSPE-PEG monolayers at the air-water interface for different polymer length by X-ray reflectivity, but could not find a consistent model – including the lipid moiety – describing the data for PEG2000 tethers in dry and humid state. They argued along the same lines as Ahrens [Ahrens et al., 2000] which proposed a laterally inhomogeneous monolayer of lipid islands embedded in PEG covered regions appearing at the surface. Although such a model can not be excluded, here the understanding of the vertical lipid distribution at the solid surface is based on a crowding effect in the PEG region which most probably leads to vertically displaced lipids as indicated by the gradual decay in the electron density profile.

Binding of pure polymers PEG2000 and PEG750 to the wet oxydized self assembled monolayer forms uniformly covered surfaces. The thickness of about (25 ± 5) Å for PEG2000 and (22 ± 5) Å for PEG750 corresponds to a collapsed mushroom and a mushroom

conformation respectively [de Gennes et al., 1987]. Measurements by ellipsometry and neutron reflectivity [Fick et al., 2003], gave similar results for the thickness of PEG2000, (24.2 ± 1.2) Å and (32.2 ± 7.9) Å respectively.

2.6 Outlook

A polymer driven staggering of the lipids in vertical direction has already been reported in a thorough X-ray reflectivity study combined with grazing incidence diffraction analysis by Kuhl [Kuhl et al., 1998], however only for measurements at the air water interface and for shorter DSPE-PEG750. A further more detailed structure of the lipid region for samples on solid surfaces with polymeric tethers of different length remains to be determined in future experiments. Such X-ray reflectivity measurements would have to be done very close to the detection limit of the method due to the short length and the low electron density of the short lipid chains, hence having a poor contrast to air. A better approach would therefore be to increase the contrast for better "visibility" of the lipids for example by deuterating the lipid chains and choosing neutron reflectometry as measuring technique instead.

A possible experimental way to further unravel the "squeezing out" effect would be to compare precise concentration dependant measurements, in the range between the low coverage and the high coverage samples, with hydration dependant measurements. An estimation of polymer driven forces, using disjoining pressures as measured by [Elender et al., 1996], could then be compared to such steric crowding forces within the PEG moiety. This approach of course implies that one could distinguish the lipids from the PEG region at different hydrations, which has not been shown so far. There are also some problems to be expected with selforganization of such monolayers at high humidity conditions [Bolze et al., 2002], but they could possibly be circumvented by adding lipids to shield the hydrophobic lipid tail region by forming bilayers. On the other hand having lipid bilayers instead of monolayers above the PEG moiety will add new forces to the system, e.g. Helfrich repulsion, which should be considered and carefully discussed.

2.7 Conclusion

It has been shown that a SiO_2 surface which was first silanized with a self assembled monolayer (SAM) can beneficially be functionalized by covalently linking polymers (PEG2000, PEG750) or lipopolymers (DSPE-PEG2000) or both consecutively ("backfilling"). They form layered structures of about 2-6 nm as could be measured by X-ray Reflectometry. The wet chemistry procedure leads to different coverings which can simply be influenced by changing concentration and reaction time. Lipopolymeric surfaces of high coverage and those of low coverage but subsequently backfilled with polymers reveal lipid anchors at the surface which can readily be used for bilayer spreading.

In summary, the wet chemistry approach for functionalizing SiO_2 surfaces with lipopolymers leads to well understood polymeric films with thicknesses in the nanometer range. In particular the backfilling process proves to be a promising approach for having lipid tethers above the polymer moiety while improving surface passivation at the same time. The advantage of this system, i.e. the modular architecture, now seems obvious and indicates that constituents of different length, for example longer polymer tethers and shorter polymers for backfilling, can lead to cushions of even better suitability for future membrane applications.

Chapter 3
Tethered Lipid Bilayers

3.1 Introduction

The initial concept of coupling lipid bilayers, e.g. model membranes, directly to polar surfaces, e.g. glass slides, by an ultrathin water layer of about 1–2 nm proved to be succesful for different biophysical investigations, such as the epitactic coupling between monolayers in supported bilayers [Merkel et al., 1989]. Later, as functional investigations of proteins at solid surfaces made use of solid supported bilayers, the rather low thickness of the intermediate water layer generated a steric problem for integral proteins. As a consequence, different ideas for lifting the membrane from the surface, i.e. tethering the lipid bilayer on a cushion and thereby increasing the intermediate space, have been followed and reviewed, [Knoll et al., 2000] and [Sackmann and Tanaka, 2000].

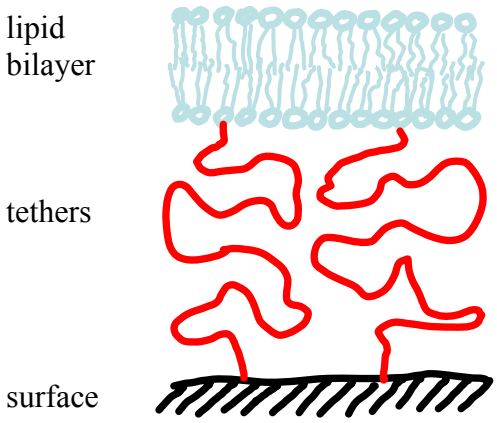

Figure 3.1 Sketch of a Tethered Lipid Bilayer

Main strategies can be differentiated depending on the type of tethers used, e.g. solid pillars, polymers, proteins or lipo-moieties. Further distinction can be made with respect to different types of functionalization to the substrate, e.g. by employing electrostatic forces, hydrophobic

interaction or by covalent binding. Different substrates can be used for tethering, distinguishable by topology, e.g. planar or curved, rough or polished, or by material properties of substances like silicon, gold, polymers or even mercury [Moncelli et al., 2004]. Furthermore the strategy of anchoring tethers into membranes may be different, e.g. either into the tail region of lipid compounds or specifically or unspecifically bound to their head groups. Finally and typically overlooked, different preparation procedures of tether functionalization and membrane spreading can have main impact on the possible use of tethered membranes. For functionalization with tethers of very high grafting density it is possible to perform polymerization directly at the surface by stepwise binding monomers on an initiator layer coupled to the surface and by terminating the reaction with a lipid moiety. Another approach is to make use of previously synthezised lipopolymers functionalized with a surface coupling group and to bind these molecules to the surface in the grafting procedure. This latter approach has been followed in the concept presented in this work, because it generally leads to a lower grafting density, allowing for more free space underneath the bilayer elevated thereby.

Structural characterization of such elevated membranes uses different methodology, including optical and impedance methods, though high resolution structural data, i.e. in the nm-range, are scarce. Only few literature data about elevation height of tethered membranes above solid surfaces are available, e.g. obtained optically by Fluorescence Interference Contrast Microscopy (FLIC) [Kiessling and Tamm, 2003] or by Neutron Reflectometry (NR) [Wong et al., 1999]. Tethered lipid bilayers have not been studied by X-ray Reflectometry (XR) before. The focus of the present chapter lies in presenting X-ray Reflectometry measurements along with fluorescence imaging analysis as a prove for the tethered lipid bilayers introduced by this thesis. Later in the chapter, structural data from literature about investigations on similar samples, e.g. grafted lipopolymer monolayers instead of bilayers, will also be discussed.

3.2 X-ray Reflectivity and Fluorescence Microscopy characterization

In the beginning of this studies the high z-resolution in X-ray Reflectivity has been used to verify the existence of tethered lipid membranes prepared on different functionalized surfaces. Ocasionally, in the process of finding good bilayer spreading conditions, the existence of a none fluid lipid bilayer was assumed from Fluorescence Microscopy experiments only. Upon additional X-ray Reflectivity measurements of these samples no (bi)layered structure could be identified, i.e. no Kiessig fringes could be observed. Such samples would have been misinterpreted by fluorescence microscopy only. Due to the higher resolution of the reflectivity measurements we were in the position to revise our picture of grafting and spreading conditions already in the early stage of our experiments and also throughout later sample development experiments. As a first result, the complementary structural characterization of samples by the two methods, i.e. optically in the x-y plane by Fluorescence Microscopy and in the z-direction by X-ray Reflectometry, proved to be a very successful experimental approach for sample development. The suitable microfluidic chamber setup has been described in Chapter 1.2.

3.2.1. X-ray Reflectivity of tethered lipid bilayers in water

X-ray reflectivity experiments were carried out to elucidate the detailed structure of the elevated bilayers perpendicular to the surface. All samples showed pronounced Kiessig fringes. Hence the data were modelled with the Parratt formalism [Parratt, 1954] using a stratified structure composed of slabs oriented parallel to the surface. Due to the high q-range assessable at the synchrotron radiation facility, up to 0.5 $Å^{-1}$, the resolution of these experiments lied in the subnanometer range, $d_{min} = \pi / q_{max} = 6.3$ Å [Pershan et al., 1994]. The analysis of all membrane data was therefore done by assuming the electron density profile consisting of 7 Å slabs with a gaussian roughness of $\sigma = 2.5$ Å in between the slabs. This roughness then defines the smallest error, i.e. $\pm 2\sigma$, for the interpretation of features within the structure of the modelled electron density profile.

3.2.1.1 Bilayers cushioned on tethers

Figure 3.2a) shows a plot of the reflectivity of an elevated membrane on a surface grafted with PEG-lipids at high surface density and a fluorescence image of the same sample.

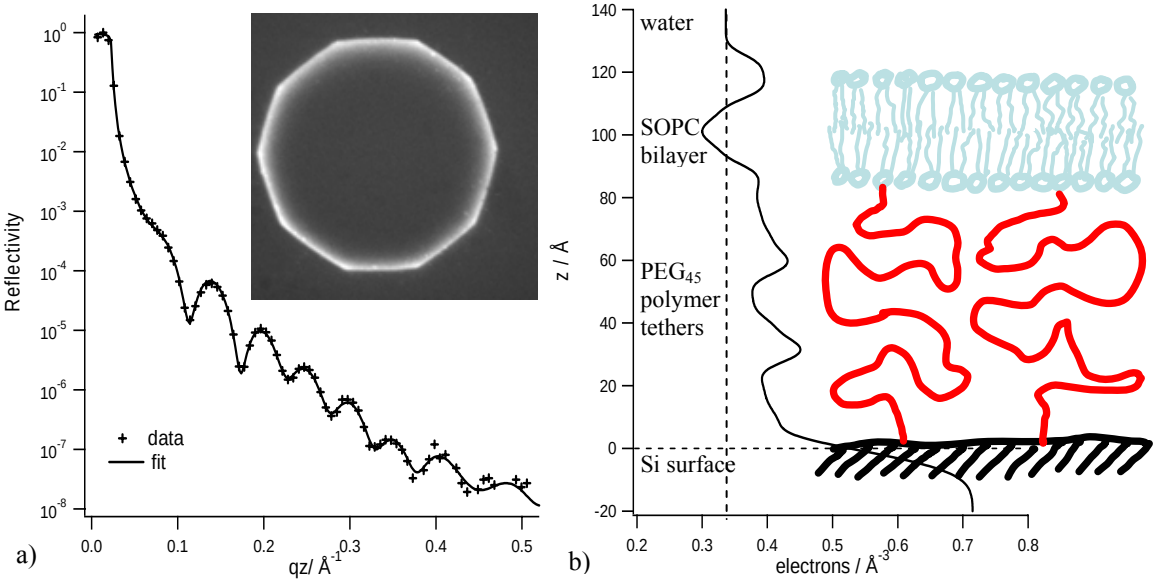

Figure 3.2 (a) Reflectivity data and modelled fit of an elevated SOPC bilayer on a silicon surface functionalized with PEG_{45}-DSPE polymer-lipid tethers anchored in the bilayer as a function of q-value. (b) Electron density profile perpendicular to the surface along with a sketch of the model used for fitting to the data. From top to bottom: the level above 130 Å is water, the footprint of the bilayer is shown between 120–80 Å, the higher electron density below the bilayer represents the PEG polymers and the lowest electron density increase at 0 Å represents the Si surface roughness. Inlet: Fluorescence image of the same membrane upon continuous bleaching; the bright ring, formed by fluorophores diffusing into the imaged area, indicates fluidity of the membrane.

The solid line represents the result of the best fit, which was obtained by assuming slabs of fixed thickness and roughness and by minimizing χ^2 while varying the electron density of the slabs. The corresponding electron density profile is shown in Figure 3.2b) along with a sketch representing a model of the crosssection of the sample.

The repeat distance of the Kiessig fringes in Figure 3.2a) suggests a first estimate of the overall thickness of the sample $d = 2\pi / \Delta q$ which is about 120 Å. The uppermost increase in the electron density profile to values above the water level, at about z = 120 Å, is due to the

lipids, specifically due to the higher electron density of their phosphate headgroups. The decrease below the water level is typical to the alkyl region of lipids and the subsequent increase again due to the headgroups. These three layers are the typical footprint of a bilayer, the thickness of which is about 4 nm, see for example [Nagle et al., 2000] and Figure 2b therein for a precise bilayer profile. With a bilayer thickness of 44 Å the elevation height between the lower headgroup and the SiO_2-surface is (80 ± 5) Å. The electron density (ρ_e) below the bilayer is at every height, i.e. for z < 80 Å in Figure 3.2b), above the water level (ρ_e (water) = 0.336 / $Å^{-3}$). This is due to grafted polymer tethers, electron density of PEG is 0.397 / $Å^{-3}$, and possibly due to additional incorporated lipids since ρ_e (lipid) > ρ_e (water) when considering both head and tail region together.

At closer inspection of the electron density profile underneath the elevated bilayer, i.e. lying in the range of 20 Å < z < 70 Å, a structure appears similar to a bilayer footprint. This structure is shifted to higher electron densities than a bilayer footprint in water. Also, the contrast between the lipid headgroup region and the tail region of this structure is significantly smaller than for the elevated bilayer. This indicates that a bilayer underneath the elevated bilayer, if at all present, is not fully covering the surface. Together with the overall increased electron density of this structure, in fact due to PEG underneath the elevated bilayer, this model favours an intrepretation of the data by formation of a patchy coverage of the surface with bilayer segments or micelles allowing for PEG moieties besides them. However, the lateral structure underneath the elevated bilayer was not the aim of this experiment and can also not unambiguously be determined hereby. It remains to be determined, e.g. by offspecular neutron scattering experiments when using the contrast matching technique by deuteration of lipids and water subphase. Nevertheless, the clear finding from these data of a high grafting density sample is the large elevation height of the bilayer above the SiO_2-surface of 8 nm.

3.2.1.2 Bilayers cushioned on tethers and backfilled polymers

Two further elevated membranes were spread on surfaces “backfilled” with PEG (see Chapter 2.2) prior to vesicle deposition and characterized by X-ray Reflectometry in Figure 3.3.

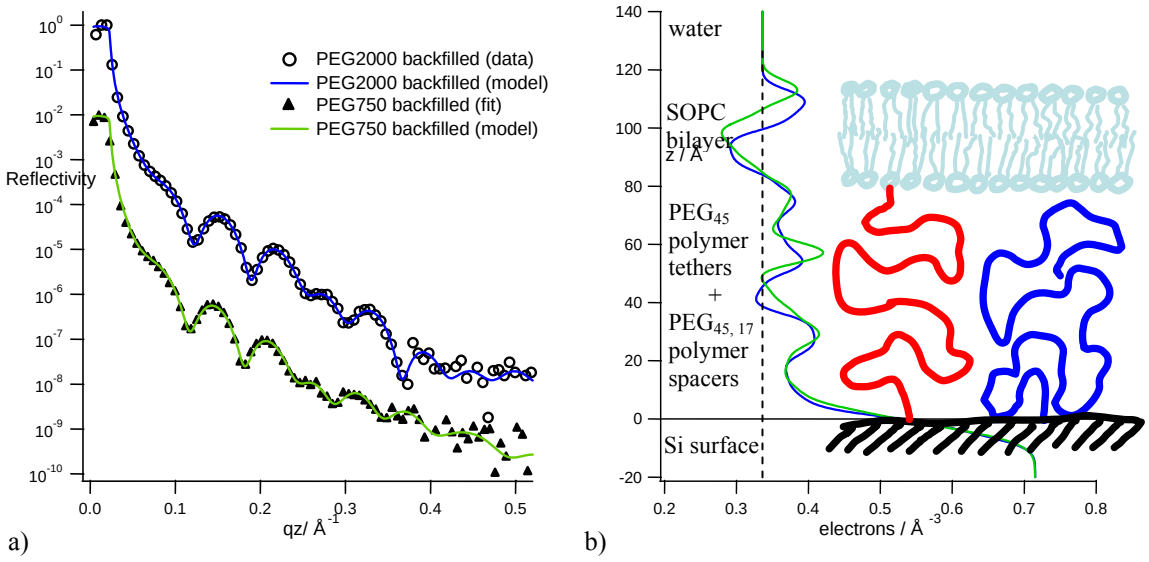

Figure 3.3 (a) Reflectivity, data and modelled fits, of elevated SOPC bilayers on a silicon surface functionalized with PEG_{45}-DSPE polymer-lipid anchors backfilled with PEG_{45} (upper curve) and backfilled with PEG_{17} (lower curve) as a function of the q-value. (b) Electron density profile perpendicular to the surface resulting from the model used for fitting to the data.

The reflectivity model fit is superimposed on the data in Figure 3.3a). Figure 3.3b) shows the electron density profile as a result of modelling to the data with 7 Å slabs as explained above. It reveals similar features as the high coverage sample discussed before. First, a typical bilayer footprint can be seen in the range of 70 Å < z < 120 Å. The elevation height of the PEG750- and PEG2000-backfilled samples, i.e. (72 ± 5) Å and (69 ± 5) Å respectively, is about 1 nm smaller than of the not-backfilled sample before. Second, a similar less pronounced bilayer footprint below the elevated bilayer indicates bilayer patches or micelles between the bilayer and the surface as before. Furthermore, the overall electron density increase above the level of water for z < 70 Å is again due to PEG and additional lipids. However, this increase is not as high as for the high coverage sample in Figure 3.2b). This finding is consistent with the refelectivity data in ambient condition (before vesicle deposition) in Figure 2.4 and 2.5 (Chapter 2), showing the high coverage sample with the highest grafting density.

3.2.2. Discussion of Membrane Reflectivity Data

The most significant result of these reflectivity experiments is the large cleft, of 7 to 8 nm, between the tethered elevated membranes and the SiO_2 surface. Others have shown that amorphous PEG2000 films grafted to solid surfaces at low density reveal similarly high hydration induced swelling, as measured by neutron reflectometry [Fick et al., 2004]. They determined a significant increase from ~25 Å in the dry state to ~70 Å in the fully hydrated state, which is in excellent agreement with the thickness increase we measured in the PEG-region of our samples after vesicle spreading (see also Chapter 2 for results on surface functionalized samples measured under ambient conditions).

In another experiment similar to ours, [Kiessling and Tamm, 2003] have used longer polyethylene glycol cushions (PEG3400) and have measured by Fluorescence Interference-Contrast Microscopy (FLIC) an elevation height of (3.9 ± 0.9) nm only. In contrast to our experiments they have used terraced SiO_2 surfaces required by the method to obtain high resolution. When reducing the lateral terrace dimension by a factor of two, from 5 x 5 μm^2 to 2.5 x 2.5 μm^2, they measured a drastic height decrease to (0.9 ± 1.0) nm. According to their interpretation, this decrease could be due to capillary forces at the edges of terraces, which "may tend to pull the membrane down". Then, such effect could already be caused by the larger terraces (5 x 5 μm^2), which means the real elevation height without terraces could be much higher then 3.9 nm, explaining the difference to the results presented here. Furthermore, they transferred the PEG-lipid monolayer from the air water interface at a surface pressure of 32 mN/m (Langmuir-Blodgett transfer). At such high pressures the PEG conformation has passed the mushroom to brush transition and is expected to be and remain after transfer in an extended state larger then the Flory Radius. On the other side, in order to obtain covalent binding of the silanized PEG-lipids with the substrate, they annealed the samples to 70 °C for 40 minutes. This high temperature might have lead to a substantial collapse of the PEG-chains while grafting. Alltogether, the differences between their experimental conditions and ours seem to be good reasons for the elevation height measurement difference by a factor of two.

A second important finding of these X-ray Reflectivity measurements of tethered membranes under water is that the elevation height can be changed by subsequent passivation of a lipopolymer grafted surface with additional covalently bound polymers, denoted

"backfilling". With only tethers underneath the membrane, i.e. no backfilling, the height results to (80 ± 5) Å. Samples with tethers and polymers backfilled show a reduced height of (72 ± 5) Å and (69 ± 5) Å for backfilling with PEG750 and PEG2000 respectively.

The influence of backfilled polymers to the membrane distance above the surface will be discussed below. Before, with regard to the tethers only samples, there is a somewhat obvious but important fact to be considered. Due to the experimental procedure, tether surface density (number of tethers per unit area) for backfilled samples is lower than for samples with tether high grafting density intended for no backfilling (see also results from measurements under ambient conditions, Chapter 2). Due to lateral steric hinderance, tethered polymers at high grafting density are extending more in vertical direction then at low grafting density. This, by its own, explains the higher elevation height of the high grafting density sample versus lower elevation heights of backfilled samples, i.e. considering tether density only without involving the influence of backfilled polymers.

However, two further explanations arrise relating the lower elevation height of backfilled samples to properties of the polymeric cushion. First, the polymer conformations of tethers, bound at two ends to surface and membrane, lose conformational entropy compared to simple grafted backfilled polymers, which are bound at only one end to the surface. This excess free energy of tethers results in an vertical repulsive force. The total force lifting the membrane is proportional to the summation of the forces excerted by each of the tethers immobilized at two ends. Samples with lower tether density and backfilled polymers immobilized at one end only will therefore excert a smaller total lifting force than the high grafting density sample, thereby leading to a smaller elevation height of these backfilled samples. Second, additional polymers below the membrane, i.e. backfilled polymers, induce depletion forces causing an attraction of the membrane to the surface. Free ends of backfilled polymers are sterically excluded from the near membrane interface. This reduces the osmotic pressure induced by the polymeric macromolecules between membrane and solid surface thereby leading to an effective attraction.

The structure of the intermediate cushion layer between the elevated membrane and the silicon surface has not been targeted by the present experiments. Nevertheless, a model can be suggested by combining information from these reflectivity measurements and from fluorescence experiments presented in the next section, which will be discussed in the

conclusion section at the end of this chapter. However, it seems appropriate at this stage to elaborate on the possibility of having two stacked lipid bilayer structures grafted on the silicon surface. This assumption has been excluded experimentally, because the upper bilayer could not be "peeled off" neither by thorough washing, which is a normally sufficient procedure therefore, nor after rigorously removing the water, drying the surface under vacuum and rehydrating the sample thereupon. Subsequent reflectivity measurements showed again the fully covered bilayer structure as discussed above and no major change in the bilayer structure of the intermediate cushion region. It could hence be concluded that the elevated bilayer is robustly tethered to the surface and not merely adhered to a second underlying bilayer.

3.2.3. Fluorescence Imaging of Tethered Lipid Membranes.

The formation of membranes was assessed by fluorescence microscopy imaging after vesicle deposition of SOPC vesicles containing 1 wt% of NBD labeled lipids on the functionalized surfaces (see Chapter 2). Continuous membranes formed on all samples and were found to be homogeneous across the entire sample area (about 1 cm^2). A representative fluorescence image is shown in Figure 3.4. These membranes were found to be stable upon thorough washings and repeated drying/rehydrating cycles. This stability for repeated usage is likely due to incorporated PEG-lipid tethers within the membrane which were covalently bound to the underlying SiO_2 surface.

It should be noted that deposition of SOPC vesicles on a pure PEG film, without PEG-lipid tethers, did not lead to formation of any membrane (data not shown). However, membrane formation occurred more readily on backfilled samples than on samples with tether functionalization only. This effect was likely due to more tether lipid tails becoming available for membrane formation at the upper PEG-lipid interface, as well as to improved density and homogeneity of the PEG-Lipid film after backfilling with PEG.

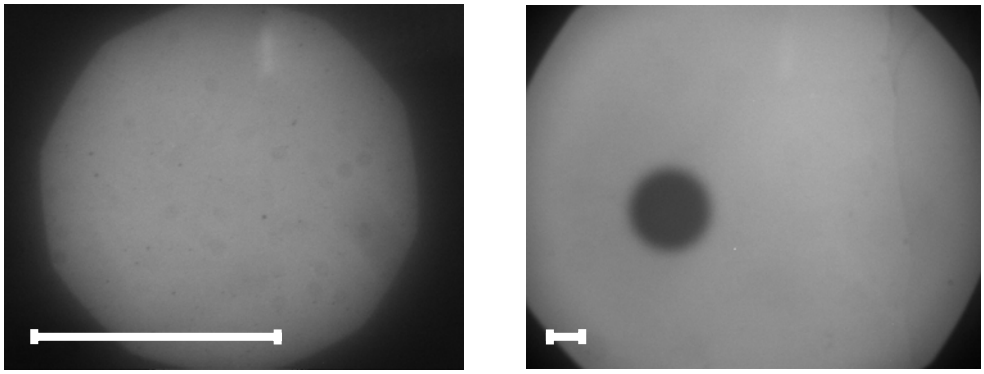

Figure 3.4 Fluorescence image of a homogeneous lipid membrane on a representative sample (backfilled with PEG2000 polymers), left before bleaching (objective 63x) and right after bleaching a small spot (objective 10x). Scale bar 25 µm.

The membranes were found to recover almost completely after fluorescence bleaching. To quantify the fluidity of the membrane, a sample spot with a diameter of about 40 µm was illuminated until complete bleaching of the dyes, as shown in Figure 3.4, and subsequent formation of a bright ring indicating fluidity of membrane components, as shown in the inset of Figure 3.2. Then, the recovery of fluorescence intensity due to diffusion of unbleached lipids into the illuminated spot was followed as a function of time in the absence of continuous illumination. This was done to test whether the whole membrane was fluid or if it exhibited a substantial fraction of immobile lipids.

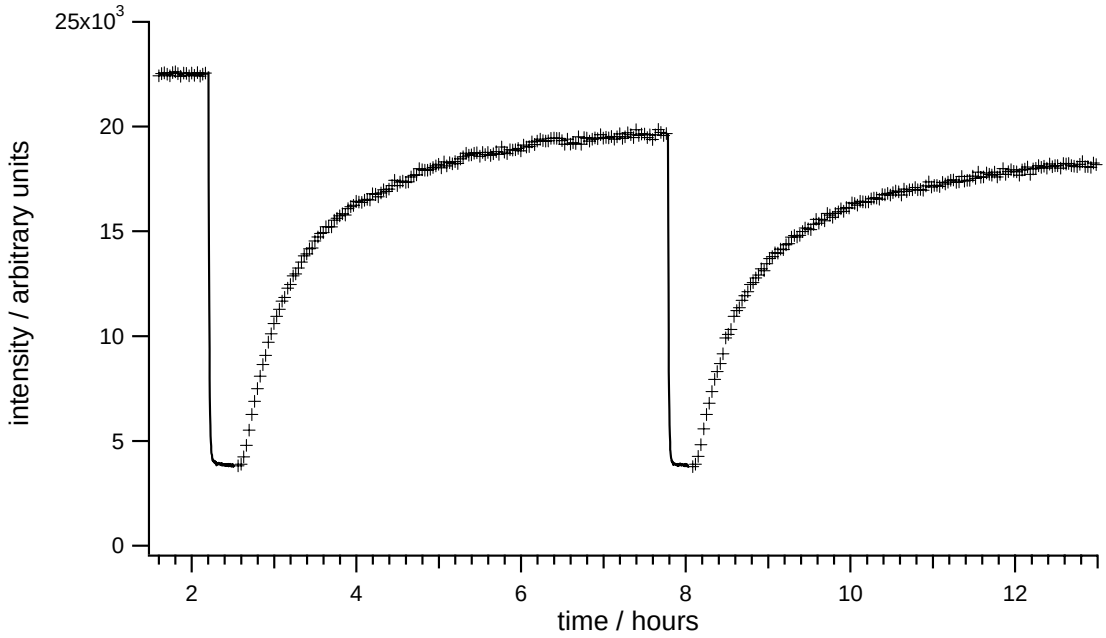

Figure 3.5 Fluorescence intensity recovery due to diffusion of unbleached lipids into the illuminated spot on a representative sample.

A SOPC membrane deposited on bare silicon dioxide was investigated and used as a reference of a model fluid membrane (data not shown). Both elevated membranes and silicon dioxide supported membranes were found to be similarly fluid with recoveries above 90%, as shown in Figure 3.5.

Furthermore, diffusion constants of fluorescently labelled lipids in both types of membranes were determined for comparison. The corresponding diffusion constants calculated according to the continuous bleaching method (see Chapter 1.5.3) were found to be: 2.2 $\mu m^2\ sec^{-1}$ for reference membranes directly on SiO_2 and 2.1 $\mu m^2\ sec^{-1}$ for tethered membranes.

3.2.4. Discussion of Fluorescence Data

These data compare well with previous reports, where diffusion constants were in the same range [Almeida et al., 1992 and Naumann et al., 2002]. Measurements of diffusion constants in tethered bilayers and in bilayers supported directly on silicon have shown that similar high diffusion constants exist in both cases [Wagner et al., 2000]. The somewhat higher absolute values of the diffusion constants measured here, i.e. about ~2 versus ~1 $\mu m^2/s$ measured

there, could be inherent to their different analyzing technique FRAP versus continuous bleaching here, a difference which is known and for example also shown in a PhD thesis [Purrucker, 2004], see Figure 2.13 therein. In that work, diffusion coefficients have been determined for different molar fractions of lipopolymer tethers, leading to the conclusion that the increase in the molar fraction of lipopolymers does not seem to influence the diffusion coefficients ($D = 0.9-1.6\ \mu m^2 s^{-1}$) or the mobile fractions (> 85 %) within the lipopolymer fraction between 0 and 20 mol%. Furthermore the increase in the spacer length caused no distinct decrease in the diffusion coefficients or in mobile fractions, suggesting that the higher steric demands of the intermediate polymer chains did not increase the viscosity of the water reservoir. All these results suggested that no diffusivity variation is to be expected for tethers of different length and molar ratios within the membrane. It is on the other hand noteworthy that others have measured higher diffusion constants for tethered membranes than they had expected before, thereby showing a sensitive variation of the diffusivity of their "free-standing" membranes [Nagle, 2000].

In summary, these fluorescence data prove the formation of fluid homogenous membranes supported on PEG-lipid films with diffusion constants and high fluorescence recoveries similar to those of known silicon oxide supported fluid bilayers.

3.3 Conclusion and Outlook

A novel architecture of solid-supported fluid membranes elevated via PEG tethers from surfaces is reported. The elevation height varying from 7 to 8 nm is large enough for the formation of "water pockets" between the elevated membrane and the surface. The silicon surface has been modified under mild chemical conditions to covalently bind a PEG cushion of tunable thickness. This type of architecture will potentially allow for studies of transmembrane proteins among others.

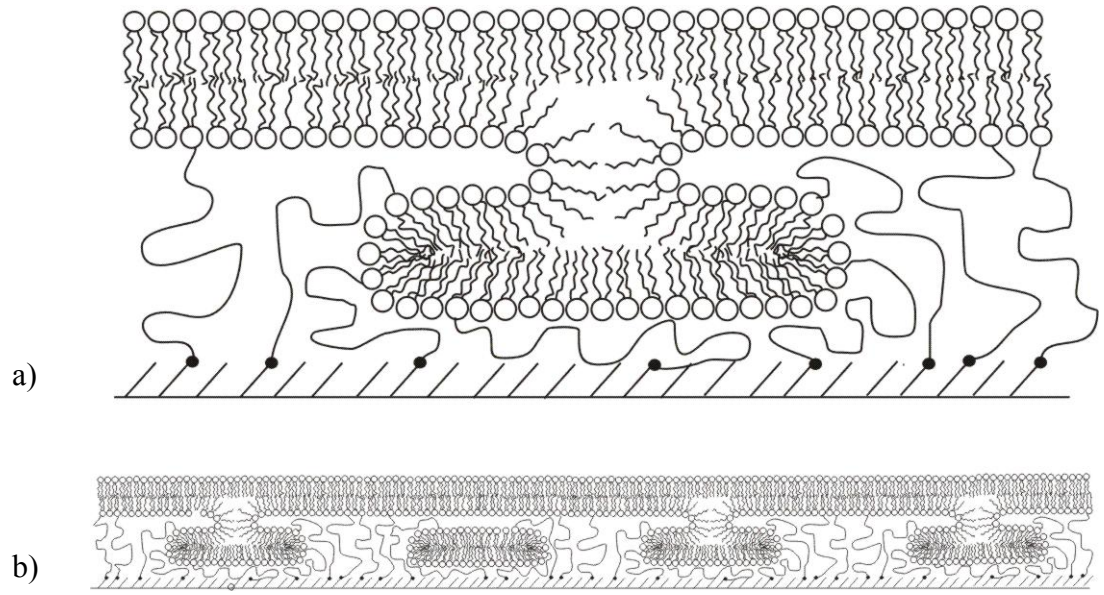

Figure 3.6 Suggested tethered lipid bilayer model: (a) enlarged view showing the bilayer beeing selfassembled on a cushion made of polymers and micellular structures and (b) the uniform lipid bilayer above the polymer tether region, including multiple lipid micelles, possibly interconnected to the upper bilayer.

Structural studies of the supported membranes by synchrotron X-ray Reflectivity allowed the determination of the thicknesses of the different interfacial films with sub-nanometer resolution. The elevation height was measured to be 8 nm for membranes deposited on functionalized surfaces with high tether density and 7 nm for membranes deposited on functionalized surfaces with low tether density and additional "backfilled" polymers.

Imaging studies with Fluorescence Microscopy revealed homogeneity and fluidity of all membranes independent from differences in tethering architecture.

Experimental evidence presented in this work proves the existence of the high quality lipid model membrane lifted away from the denaturing solid surface, the structure of the intermediate cushion region could not be unambiguously determined. However, the electron density profile of this intermediate region suggests the presence of lipid bilayer structures included in the polymeric cushion, which possibly have the form of micellular islands or of patchy bilayers with spaces in between for the polymeric moieties. The model sketched in Figure 3.6 shows such micellular bilayers interconnected with the upper lipid bilayer. This assumption of the interconnection arrises from the fluorescence recovery measurements upon bleaching. The high recovery above 90% is been observed even after repeated recovery measurements. This means that fluorescently died lipids diffuse into such micellular structures. The formation of such interconnections between lipid bilayer structures is also known to be favoured by the presence of PEG in a so called process of hemifusion.

A further path to follow has been paved by these experiments in that they have shown the next steps to go. In a direct next step a more detailed structural analysis for understanding the equilibrium height of the elevated membranes is necessary. Therefore, investigating the space between membrane and surface by neutronscattering techniques and selective deuteration of constituents seems the most promising approach towards such a thorough structural characterization. A further discussion of possible reasons explaining different elevation heights should then be based on detailed information about the samples constitution in between membrane and surface, e.g. polymeric conformation and relative molar composition of constituents at the surface.

Some of the potentials of the system towards applications, in particular with respect to protein analysis, have been outlined in the introductory part of this thesis. More precise and diverse methodical characterization of the system for fundamental investigations seem feasible. For example, temperature, hydration and pH dependent measurements of such self organized macromolecules will allow for a detailed thermodynamic and electrochemical analysis of lipopolymeric complexes at surfaces, for example, as indicated in [Albertorio, 2005] and [Hertrich, 2008].

Appendix I

Motility gliding assay: Myosin V anchored on a fluid solid supported membrane

A1. Introduction and Summary

The use of lipid coupled supramolecular protein assemblies as an interfacial matrix allows the assembly of complex machineries such as chemomechanical actin/myosin systems on semiconductor devices or other solid surfaces. In general, biofunctionalization of solid surfaces by ultra-thin polymer films, polymer/lipid composite films (see Chapters 1–3) or supported membranes with reconstituted proteins (for example herein) provides a powerful strategy to generate biointerfaces between inorganic and biological materials.

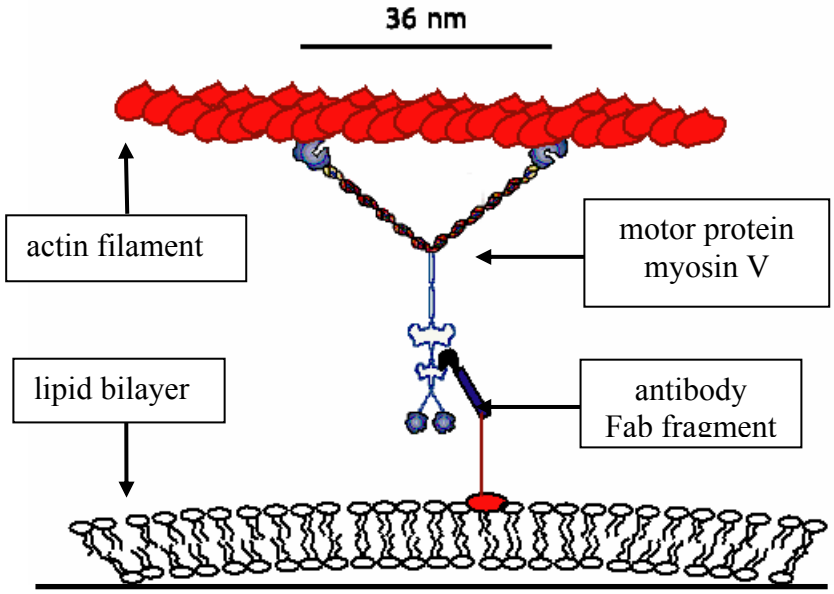

Figure AI.1 Schematic of the investigated system: actin dynamics driven by Myosin V molecular motors being coupled to a solid supported fluid lipid bilayer via monoclonal antibodies.

Motility gliding assays have been used over years to elucidate the functionality of strokes of motorproteins. Details of such power strokes, like molecular mechanism of force generation and angles of motor steps have been assessed thereby [Rief et al., 2000]. Different enzymatic motors like Heavy Meromyosin (HMM), Moysin II or Myosin V, a progressive motor with step length of 36 nm, have been used to analyze gliding single actin filaments conformations. However, long observation times were not possible when immobilizing the motor proteins to a passivated surface by hydrophobic interaction between their tail domain and for example hydrophobic nitrocellulose directly grafted on a glass surface. Typically, experiments lead to rupture of actin filaments at high concentrations of motor molecules (and ATP) which merely showed that the power stroke of such a motor protein (or a cooperative stroke of a group of proteins) is larger than the rupturing force for actin but which would set the limit for further experimental investigations. Therefore the need for a biomimetic surface functionalization arrose which would allow the motor protein to function more smoothly, i.e. without destroying the actin trail, and still be observable with the usual fluorescence microscopy method. Experimental evidence of such improved systems became possible by this work in a close colaboration with Junshan Zhang, a colleague with expertise in the biochemical preparation of the experimental constituents.

Here, actin dynamics in two-dimensional motility assays on fluid, solid-supported lipid membranes are presented. Myosin V molecular motors were coupled to membranes via monoclonal antibodies specific to a defined region of the myosin rod which did not interfere with motor and/or ATPase activity, see Figure AI.1. The single double-headed motor molecules were anchored in the lipid membrane without intermolecular cross-linking by using lipidated Fab fragments of these antibodies. Thereby, it was possible to observe and analyze two-dimensional dynamics of single actin filaments for long observation times, in the order of minutes, in the presence of either adenosindiphosphate (ADP), for bound but inactive motors, or adenosintriphosphate (ATP), for active motors.

A1.2 Results

In our early experiments, when motor proteins were directly coupled to a nitrocellulose-functionalized surface, fragmentation of actin filaments during classical motility assays seemed to be inevitable. Long filaments existed only for a short period of time (for less then a

few minutes), before braking in parts, such that after an incubation with ATP for about 10 minutes, only short filaments were observed. A typical breaking event is shown in Figure AI.2.

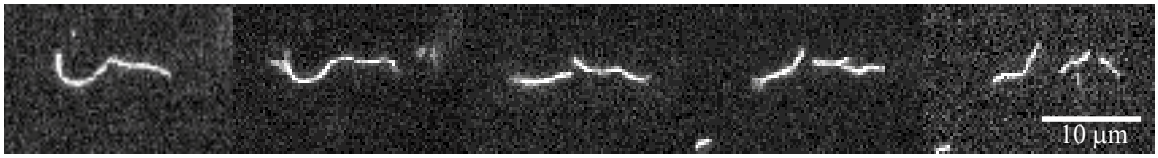

Figure AI.2 Myosin V motility gliding assay on a nitrocellulose passivated surface: actin filaments rupture by motor protein forces.

An actin filament with a length of ~12 µm breaks into shorter pieces which have various length ranging from ~2 µm to ~8 µm which is within the range of persistence length of F-actin. Presumably, it is the cooperation of a group of Myosin V binding to the same filament that should be responsible for the fragmentation. It is also possible that rigor heads hinder the sliding motion of actin by creating local loops and eventually rupturing the polymer chain.

In a first attempt to improve the substrate-protein interaction towards a more natural environment we first made use of the same surface immobilization principle as before but substituted nitrocellulose with lipids. The motor proteins were thereby coupled by hydrophobic interaction to lipid monolayers and bilayers directly deposited on glass by the Langmuir-Blodgett and the Langmuir-Schaeffer technique respectively. These attempts had no success, i.e. no motility assay could be detected on a pure lipid monolayer and only very few binding events of the motor protein could be observed directly adhered on a lipid bilayer. Therefore, we established a more sophisticated system involving specific binding of the motorprotein to an antibody exhibiting lipid anchors immobilized in a fluid lipid membrane, see Figure AI.1.

Fluid lipid bilayers were constructed to mimic an in vivo environment for Myosin V. The motor proteins were immobilized via Fab fragment prepared from monoclonal anti-myosin antibodies on the surface of the solid supported lipid bilayers. The gliding motion of actin filament over fluid lipid bilayers differed from that observed in conventional motility assays.

Such differences were improved stability of long actin filaments (>10 µm), see Figure AI.3, and higher flexibility in track changing of short actin filaments (<1 µm), data not shown.

Figure AI.3 Demonstration that actin filaments do not rupture on a fluid membrane support. In contrast to this, filaments are ruptured after ATP addition to a nitrocellulose fixed motility gliding assay (compare to Figure AI.2).

In a further example of such a motility assay on a fluid membrane a single actin filament longer than 30 µm is shown in Figure AI.4. The analysis of conformational changes of single actin filaments, which can be considered as a model system to study fundamental properties of semiflexible filaments, becomes feasible. These results confirm the assumption that two dimensional fluidity of a bilayer provides high flexibility to Myosin V when attached to the surface via such a bilayer.

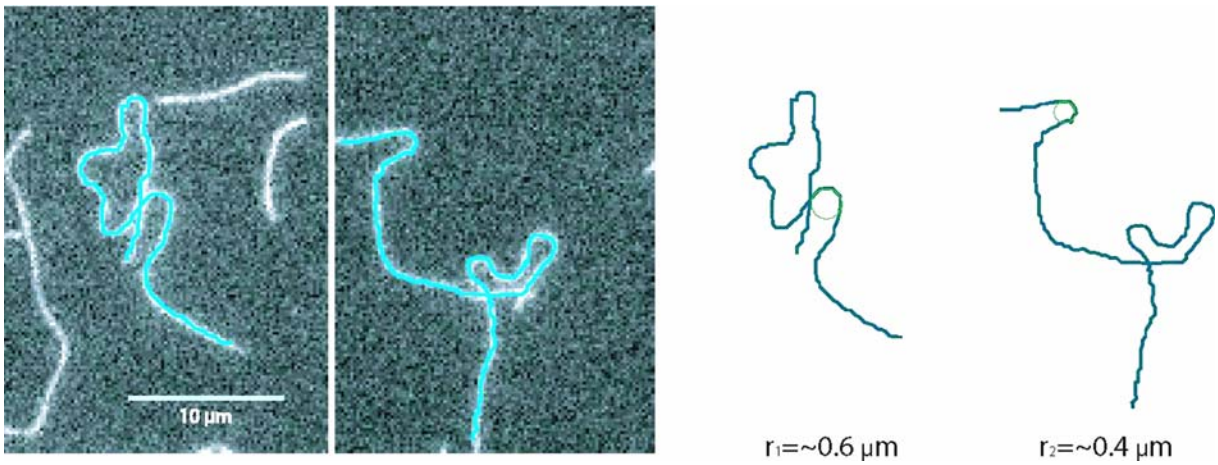

Figure AI.4 Motility gliding assays on fluid membranes representing a biocompatible environment for the analysis of conformational changes of single actin filaments. Bending with a radius of curvature as low as 0.4 µm could be observed. Note that very long filaments (> 30 µm) exist even after long sliding times (> 10 min).

A1.3 Conclusion and outlook

In this appendix it was shown that the type of surface functionalization strongly influences structure and function of a protein assembly under investigation in the vicinity of a solid surface. Anchoring the motor protein to a fluid solid supported membrane via a lipid coupled antibody improved the interactions between actin and the motor protein towards higher flexibility, i.e. including many conformational changes, of the semiflexible gliding actin polymer chain and towards longer experimental observation times. These first set of experiments of the present PhD work clearly showed that a further improvement of supported bilayers and a better control of the distance of the functional entity to the solid surface was desirable. As a result, a new versatile surface functionalization by polymer tethered lipid membranes has been developed and is being presented in the different chapters of the thesis.

Foreword to Appendix II–IV

Constructions at the neutron reflectometer with option for small angle scattering REFSANS

The experimental work on assembling the neutron reflectometer with option for small angle scattering REFSANS at the scientific neutron reactor Heinz Maier-Leibnitz in Garching demanded a substantial part of the time invested during this PhD work and is herein reported by cummulative attachment of three publications. The instrument went operational in summer 2005 and parts of the work were published in [Kampmann et al., 2004] and [Kampmann et al., 2006], see Appendix II and IV. Another important achievement were the first measurements of neutron beam characteristics after passing a twisted neutron guide, which were published in [Zeitelhack et al., 2006], see Appendix III.

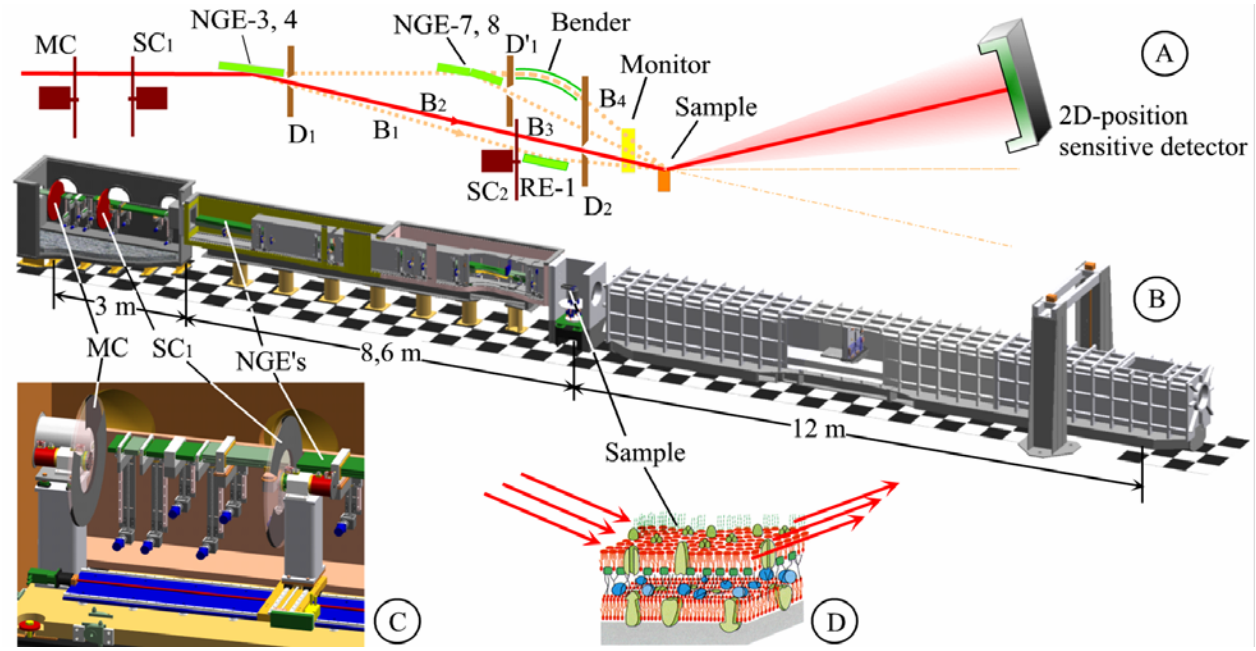

Figure AII.1 Schematic of REFSANS: A neutron beam (red line) is scattered by a sample (D) and measured with a two dimensional detector (A), which can be positioned within a vacuum chamber (B). Different beam settings (B_1-B_4) allow for varying incidence angles, achieved by positioning neutron guide elements (NGEs, green). Further parts: master and slave chopper (MC, SC) for time of flight settings and diaphragms (D) for restricting the beam. Note the overall length of the instrument of about 24 m.

REFSANS is a high resolution reflectometer with an option for measuring small angle neutron scattering, see Figure AII.1. It is dedicated to the analysis of horizontal samples, in particular to experiments at the air water interface. The instrument is furthermore perfectly suitable for the analysis of solid or soft matter surfaces, which for example need fluid exchange or horizontal geometries for other experimental reasons. Such versatile sample environment requires bending of the incident neutron beam, which is being achieved by a 12 m variable neutron guide system. A two dimensional position sensitive detector within a vacuum tight scattering tube can be positioned at different distances from the sample, which theoretically allows momentum transfer measurements in an extremly broad range from about 0.01-10 nm^{-1}. As a time of flight device suitable for transmitting neutrons from the cold source in the wavelength range from 0.2–3 nm, REFSANS thereby allows the analysis of lateral and vertical structures in the nm-μm range. Therefor, measuring reflectivity and small angle neutron scattering can either be done simultaneously or the instruments geometrical settings can, for special applications, be set without changing the sample position, which is specifically advantageous for the analysis of soft matter samples. This versatile instrument has been planed and produced over many years at the Institut für Werkstoffforschung GKSS in Geesthacht.

Part of the present work consisted in assisting the construction phase of REFSANS in the neutron guide hall of the scientific reactor FRM-II of the Technical University Munich. In the beginning, different mainly organisational tasks were required: installing of working places in the instrument's office, in the experimental hall and in the laboratory. Different parts of the instrument were delivered over many months and required time consuming coordination of their delivery, storage and assembly in the neutron guide hall. A major part of the experimental work dealing with the setting up of the instrument involved meticulous adjustments and sometimes rebuild of technical parts. Collaborations with workshops and external companies speeded up the constructions, for example in designing and building connections to the neutron guide and between different vacuum chambers and the pump station, in electrically connecting the movable neutron guide elements or in reducing unexpected vibrations in the chopper system. Sample environments have been constructed including a film balance setup for simultaneous neutron scattering and optical microscopy measurements or a versatile goniometer setup together with a customized software control. Finally, the shielding has been build and fulfilled the radiation protection requirements so that the instrument has succesfully been put into operation.

Figure AII.2 Photos of the entire instrument during construction (top) and of the chopper system during a test phase (bottom).

Figure AII.3 Photos of setting up the neutron guide elements (left) and the vacuum pump station (right).

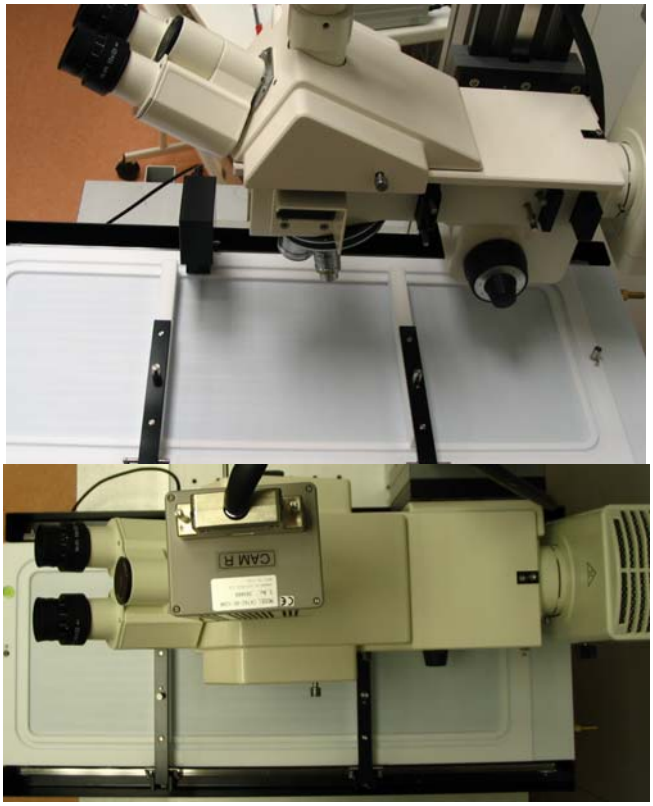

Figure AII.4 Photos of the combined setup film balance with optical microscopy for the sample environment, side view (top) and top view (bottom).

Available online at www.sciencedirect.com
SCIENCE DIRECT®
Physica B 350 (2004) e763–e766
PHYSICA B
www.elsevier.com/locate/physb

The potential of the horizontal reflectometer REFSANS/FRM-II for measuring low reflectivity and diffuse surface scattering

R. Kampmann[a,*], M. Haese-Seiller[a], V. Kudryashov[a], V. Deriglazov[c], M. Tristl[b], Ch. Daniel[b], B. Toperverg[c], A. Schreyer[a], E. Sackmann[b]

[a] *Institut für Werkstoffforschung, GKSS Forschungszentrum, Max-Planck-Str. 1, D-21502 Geesthacht, Germany*
[b] *Fakultät für Physik, Department E22, TU-München, D-85747 Garching, Germany*
[c] *Petersburg Nuclear Physics Institute, Gatchina 188350, Russian Federation*

Abstract

The reflectometer REFSANS being built at the high flux reactor FRM-II in Munich is dedicated to the analysis of surfaces, interfaces and phase boundaries at the air–water interface of liquid/soft matter. Novel time-of-flight design and neutron optics have been developed to make it a most flexible device for the comprehensive analysis of samples with horizontally aligned surfaces. The potential of REFSANS for measuring low reflectivity and off-specular scattering is outlined.

PACS: 28.20.Cz; 29.40.Cs; 29.40.Gx

Keywords: Neutron absorption; Gas-filled counters; Ionization chambers; Proportional counters; Avalanche counters; Tracking and position-sensitive detectors

1. Basic design of REFSANS

At the new research reactor FRM-II in Munich/Germany the horizontal reflectometer REFSANS is being built at the end of the cold neutron guide NL-2b being tilted by 90° to achieve a cross-section of 12 mm in height and 170 mm in width at its end [1]. The main components of the reflectometer are the 3-double-disc chopper, its ~12 m long neutron guide system with in parts novel neutron guide elements, the sample chamber and the scattering tube in which a 2D-position-sensitive detector (active area: 500 mm × 500 mm; spatial resolution: ~2 mm × 2 mm [2,3]) can be positioned at distances between ~2 and 12 m from the sample (Fig. 1).

REFSANS is designed as a time-of-flight machine to cover simultaneously a large region of momentum transfers. The chopper device is a generalization of that proposed by van Well [4]. It consists of three double discs the window of each of which can be opened between 0° and 120°. The first pair of disks, the master chopper (MC) is fixed

*Corresponding author. Tel.: +49-4152-87-1316; fax: +49-4152-87-1338.
Email-address: reinhard.kampmann@gkss.de (R. Kampmann).

0921-4526/$ - see front matter © 2004 Published by Elsevier B.V.
doi:10.1016/j.physb.2004.03.198

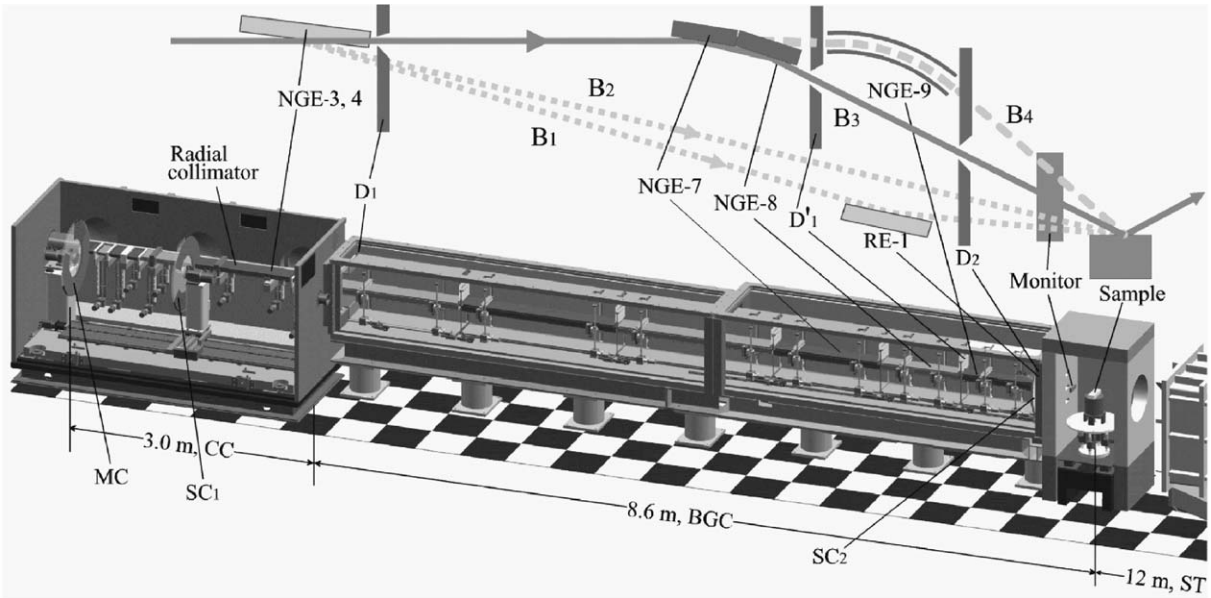

Fig. 1. Schematic view of REFSANS (MC: master chopper; SC_1, SC_2: slave choppers; D: diaphragm; CC: chopper chamber; BGC: beam guide chamber; NGE: neutron guide element; RE: reflector element; B_1 to B_4: beam settings).

at the end of the NL-2b, whereas, the second pair of disks (slave chopper, SC_1) can be positioned at distances between $\sim$5 cm and 2.2 m from the MC to adjust the wavelength resolution between $\sim 0.5^{\circ}\% < \Delta\lambda/\lambda < 15\%$ FWHM [5].

2. Performance of REFSANS at low λ-resolution

The horizontally aligned sample surface may be positioned at a height of $\sim$115 mm below the mean height of NG-2b to illuminate the sample with different beam settings covering a very broad range of momentum transfer (Fig. 1).

The MC and SC_1 are usually operated with equal opening angles and rotation speeds, and SC_1 opens at that moment when the MC closes [4,5]. Such a 2-disc chopper transmits neutrons in the range from 0 to $\lambda_{max} = 2\lambda_0$ with $\lambda_0 \sim \lambda_{max}/2$. SC_2 is operated at about half the distance between MC and the detector, it allows to operate REFSANS in the wavelength region of high transmission ($\lambda_{min} < \lambda < \lambda_{max} \sim \lambda_0$) . The 3-double-disc device results in much higher mean beam intensities and significantly improved wavelength resolution [5].

In the following the performance of REFSANS is discussed for the case of low resolution or highest beam intensity: MC and SC_1 are operated at a distance of $\sim$2 m and the distances form SC_1 to the sample as well as from the latter to the detector are $\sim$10 m. The 3-disc chopper restricts the transmitted wavelength range to 0.4 nm $< \lambda <$ 1.6 nm, the area of high luminosity of the cold source. The openings of the collimation entrance and exit slits are set such that the resolutions in incidence angle and wavelength are almost equal $\Delta\theta/\theta \sim \Delta\lambda/\lambda \sim 7\%$. These settings result in a resolution of the momentum transfer of $\Delta q/q \sim 10\%$ [5].

For the case of a time of flight device one has to distinguish between the peak $I_{peak}(\lambda, \Delta q)$ and the mean $I_{mean}(\lambda, \Delta q)$ intensity: $I_{peak}(\lambda_i, \Delta q)$ is the peak neutron flux in the detector plane at a given point in time t_i within a chopper revolution, when neutrons with the mean wavelength $\bar{\lambda}_i$ arrive at the detector plane. $I_{mean}(\lambda, \Delta q)$ is obtained by multiplying $I_{peak}(\lambda_i, \Delta q)$ with the chopper transmission.

Peak and mean intensities calculated with these beam settings and assuming a surface size of

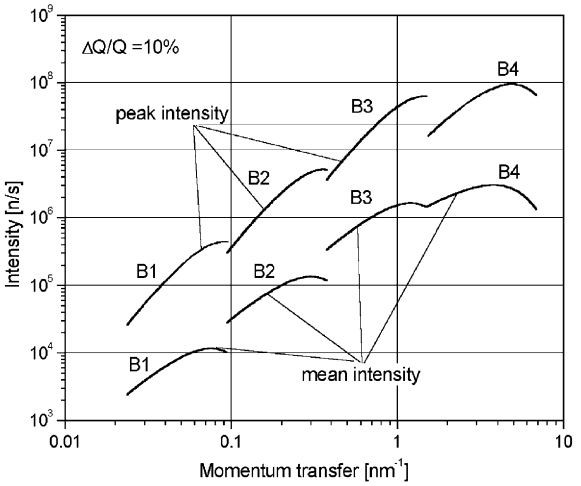

Fig. 2. Peak and mean (time averaged) beam intensities I_{peak} and I_{mean} for the conventional reflection geometry. The 3-disc chopper is assumed to be operated with $\lambda_{min}=0.4$ nm and $\lambda_{max}=\lambda_0=1.6$ nm. Intensities are shown for q-resolutions of 10%. The beams B_1–B_4 (see Fig. 1) have different incidence angles of 3, 12, 48 and 192 mrad.

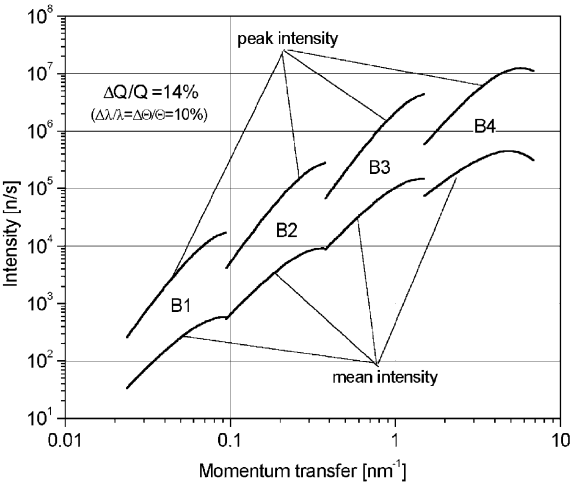

Fig. 3. Calculated peak and time averaged beam intensities I_{peak} and I_{mean} of 13 beams B_1–B_4 horizontally focused in the detector plane.

60 mm × 60 mm are shown in Fig. 2. Beams B_1–B_4 altogether cover an extremely broad range of momentum transfer from ~0.02 to ~7 nm^{-1}. It is pointed out that maximum peak intensities of $I_{peak}(\lambda, \Delta q) > 10^8$ n/s are to be expected at low q-resolution.

The times for measuring sections of reflectivity curves $t_{meas}(q, \Delta q)$ can be derived directly from the reflectivity $R(q)$, the mean flux and the minimum number of neutrons N_c to be collected in one resolution interval $(q, q+\Delta q)$, if the background is neglected: $t_{meas}(q, \Delta q) = N_c/(R(q)\ I_{mean}(\lambda, \Delta q))$.

For example, Fig. 2 shows that beam B_4 has a mean intensity of $I_{mean}\ (q, \Delta q/q = 10\%) > 10^6\ s^{-1}$ over the q-range ($\sim 1.5\ nm^{-1} < q < 7\ nm^{-1}$). If we assume in this q-range e.g. (i) a minimum reflectivity of $R \sim 10^{-8}$, (ii) a negligible background and, (iii) if we require in each q-interval at least $N_c = 100$ neutrons then we find a total measuring time of only $t_{meas}(q, \Delta q) < 10^4$ s. Thus, within only ~3 h REFSANS will allow the measurement of a reflectivity curve with $R \sim 10^{-8}$ with a resolution of $\Delta q/q = 10\%$ over the q-range from $\sim 1.5\ nm^{-1} < q < 7\ nm^{-1}$. Such a run would deliver more than 100 counts in each of the 15 q-intervals.

The minimum measurable reflectivity R_{min} may be estimated from the peak flux and the detector background $I_{b,d}$: $R_{min}(q, \Delta q) \sim I_{b,d}/I_{peak}(q, \Delta q)$. The background of the area detector of REFSANS in the area where the specularly reflected neutrons are measured is smaller than $I_{b,d} < 0.01$/s. With $I_{peak}(q, \Delta q = 10\%) > 10^8$/s we conclude that reflectivities as low as $R_{min}(q, \Delta q = 10\%) < 10^{-10}$ will be accessible at REFSANS even for the case of horizontally aligned samples.

It is pointed out that due to these high beam intensities at low q-resolution and the large 2D-position-sensitive detector REFSANS is expected to offer excellent conditions for analyzing diffuse surface scattering. This may be measured in conventional scattering geometry with a slit-height smeared beam.

REFSANS allows further to perform reflectivity measurements in point focussing geometry. In this case very high beam intensities will be achieved by means of (i) focussing 13 beams in the detector plane [1,5] and (ii) operating REFSANS with low wavelength resolution. Then beam intensities up to $10^7\ s^{-1}$ can be obtained in reflection geometry from a sample surface with a size of ~80 mm × 60 mm (Fig. 3). The performance of the REFSANS in this setting may be compared with illuminating the sample surface with 13 beams

from modern SANS instruments such as D22 at ILL. In this scattering geometry REFSANS will offer new perspectives for GI-SANS investigations as well as for measuring specular reflectivities as low as 10^{-7} from samples with a strong incoherently scattering substrate such as H_2O [5].

3. Summary

The novel time-of-flight instrument REFSANS allows of comprehensive analyses of the air/water interface. In this paper it has been shown that REFSANS (i) will allow to measure extremely low specular reflectivity and (ii) will offer new perspectives for measuring off-specular scattering and grazing incidence SANS (GI-SANS).

Acknowledgements

The authors would like to acknowledge technical support from R. Kiehn, A. Vogel and the FRM-II staff. The present work has been supported by the Federal Ministry of Education, Research, and Technology (BMBF) of Germany (Contract No. 03-KA5FRM-1 and 03KAE8X3).

References

[1] R. Kampmann, M. Haese-Seiller, M. Marmotti, J. Burmester, V. Deriglazov, V. Syromiatnikov, A. Okorokov, F. Frisius, M. Tristl, E. Sackmann, Appl. Phys. A 74 (Suppl.) (2002) 249.
[2] M. Marmotti, M. Haese-Seiller, R. Kampmann, Proceedings of the International Conference on Neutron Scattering (ICNS-2000), Appl. Phys. A 74 (Suppl.) (2002) S252.
[3] R. Kampmann, M. Marmotti, M. Haese-Seiller, V. Kudryashov, Proceedings of the European Conference on Neutron Scattering (ECNS 2003), Physica B, these proceedings.
[4] A.A. van Well, Physica B 180 & 181 (1992) 959.
[5] R. Kampmann, et al., to be published.

Available online at www.sciencedirect.com
SCIENCE DIRECT®
ELSEVIER
Nuclear Instruments and Methods in Physics Research A 560 (2006) 444–453

NUCLEAR INSTRUMENTS & METHODS IN PHYSICS RESEARCH Section A
www.elsevier.com/locate/nima

Measurement of neutron flux and beam divergence at the cold neutron guide system of the new Munich research reactor FRM-II

K. Zeitelhack[a,*], C. Schanzer[b], A. Kastenmüller[a], A. Röhrmoser[a], C. Daniel[c], J. Franke[e], E. Gutsmiedl[a], V. Kudryashov[d], D. Maier[a], D. Päthe[a], W. Petry[a], T. Schöffel[a], K. Schreckenbach[a], A. Urban[a], U. Wildgruber[e]

[a]*ZWE FRM-II, TU München, D-85747 Garching, Germany*
[b]*Physik-Department E21, TU München, D-85747 Garching, Germany*
[c]*Physik-Department E22, TU München, D-85747 Garching, Germany*
[d]*GKSS Forschungszentrum GmbH, D-21502 Geesthacht, Germany*
[e]*Max-Planck-Institut für Metallforschung, D-70569 Stuttgart, Germany*

Received 11 August 2005; received in revised form 9 December 2005; accepted 16 December 2005
Available online 18 January 2006

Abstract

A sophisticated neutron guide system has been installed at the new Munich neutron source FRM-II to transport neutrons from the D_2 cold neutron source to several instruments, which are situated in a separate neutron guide hall. The guide system takes advantage of supermirror coatings and includes a worldwide unique "twisted" guide for a desired phase space transformation of the neutron beam. During the initial reactor commissioning in summer 2004, the integral and differential neutron flux as well as the distribution of beam divergence at the exit of two representative and the twisted neutron guide were measured using time-of-flight spectroscopy and gold-foil activation. The experimental results can be compared to extensive simulation calculations based on *MCNP* and *McStas*. The investigated guides fulfill the expectations of providing high neutron fluxes and reveal good quality with respect to the reflective coatings and the installation precision.

PACS: 29.30.Hs

Keywords: Neutron guide; Neutron flux; Beam divergence; Cold neutrons; Supermirrors; Neutron spectrum

1. Introduction

The new high flux research reactor FRM-II, now called Research Neutron Source Heinz Maier-Leibnitz in Garching is designed as a multipurpose facility for the use of neutrons in basic research and technical applications [1]. It is a 20 MW heavy water moderated reactor operated with a single fuel element of enriched ^{235}U (93% enrichment). The compact core design provides an unperturbed maximum thermal neutron flux of $8 \times 10^{14}\,n/cm^2/s$ (high energy cut-off $E = 0.625\,eV$). Inside the D_2O-moderator tank a cold neutron source (CNS) [2] is placed in 40 cm distance to the reactor core axis, close to the thermal flux maximum. The CNS moderator cell is a vessel of 30 cm in diameter and about 30 cm in height. It is designed to contain maximal 15 l of liquid deuterium at 25 K temperature and 150 kPa pressure. Inside the CNS a flux of $0.9 \times 10^{14}\,n/cm^2/s$ of cold neutrons (energy $E \leqslant 4.5\,meV$) is expected [3]. The CNS supplies cold neutrons to three individual beam tubes schematically shown in Fig. 1. Two tubes feed *PANDA* (SR-2), the triple axis spectrometer for polarized cold neutrons and the tomography station *ANTARES* (SR-4), which are located in the experimental hall of the reactor building. The third tube (SR-1) is used to channel neutrons from the reactor towards the experimental areas in the external neutron guide hall via a sophisticated neutron guide system [4], which is briefly described in Section 2.

*Corresponding author. Tel.: +49 89 289 14703; fax: +49 89 289 14989.
E-mail address: karl.zeitelhack@frm2.tum.de (K. Zeitelhack).

0168-9002/$ - see front matter © 2006 Elsevier B.V. All rights reserved.
doi:10.1016/j.nima.2005.12.215

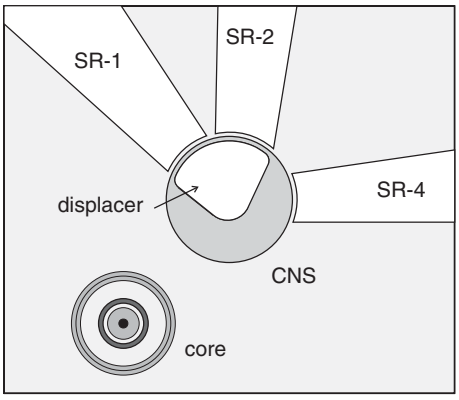

Fig. 1. Schematic horizontal cross-section of the D_2 cold neutron source CNS mounted in the thermal flux maximum in the D_2O moderator tank. The beam tube SR-1 feeding the neutron guide system closely faces the displacer of the CNS.

On March 2nd, 2004 FRM-II reached criticality for the first time and was commissioned during the following months at increasing reactor power until it reached its nominal power of 20 MW on August 24th. During the commissioning, functionality and radiation shielding of the complete neutron guide system were checked. A proper quality of the neutron guide system is of crucial importance for the performance of the attached neutron beam instruments. Therefore, a detailed experimental verification of the beam properties at the end positions of the neutron guides was of fundamental interest. Due to reasons of radiation protection and space limitations, we had to restrict the measurements to three cold neutron guides where existing monochromator or chopper shieldings enabled access during the initial commissioning. The integral and spectral neutron flux as well as the distribution of beam divergence were measured at the end position of neutron guides NL1, NL6a and the twisted guide NL2b using a versatile ToF-spectrometer described in Section 3. The results are presented in Section 4. In addition, standard gold-foil activation was employed to determine integral neutron fluxes separately. NL1 and NL6a were chosen as representatives of a supermirror coated and a standard ^{58}Ni coated neutron guide, respectively. The investigation of the twisted guide NL2b was of special interest due to its unique concept.

Detailed simulation calculations using *MCNP* [5] and *McStas* [6] were performed to describe the performance of the CNS and the neutron transport properties of the guides NL1 and NL6a. The experimental verification of the simulations should allow reliable predictions for guides not accessible to measurements and for new guides to be installed in the foreseen upgrade.

2. Cold neutron guide system

The extensive neutron guide system at FRM-II schematically shown in Fig. 2 extracts neutrons from the cold neutron source (CNS) through beam tube SR-1, which closely faces the CNS with its displacer. The displacer is a fractional volume of the cold source vessel, which is filled by D_2-gas at 20 MW reactor power and thereby provides a view into the interior of the CNS moderator. The beam tube is filled with He and has a total length of 4 m. Six primary neutron guides (NL1–NL6) start at a distance of 2 m from the centre of the cold source. The first units of each guide have a length of 2.2 m and are mounted in a common guide housing inside SR-1. All those units are coated with Ni–Ti supermirrors with $m = 2$ except NL4, which has $m = 1.2$ at the side walls with m denoting the reflectivity range of the specific coating normalized to the critical angle of natural Ni. The six guides are installed with directions of $\pm 1.0^\circ$, $\pm 6.6^\circ$ and $\pm 8.75^\circ$ to the axis of the beam tube and have cross-sections of $170 \times 50\,\mathrm{mm}^2$ (two guides), $170 \times 60\,\mathrm{mm}^2$ (2) and $120 \times 60\,\mathrm{mm}^2$ (2), respectively. A conical mirror box is mounted to the source side end of the guide housing to improve the illumination of the guides for neutrons with wavelength $\lambda > 10$ Å. It consists of polished Cu-plated aluminium coated with supermirrors $m = 2.2$. Outside the biological shielding of the reactor, the primary shutter common to all six neutron guides is mounted subsequent to the beam tube SR-1. Along their path through the tunnel (18 m) in the reactor hall and the casemate (10 m) leading to the neutron guide hall, each primary guide is subdivided in width or height in up to three individual secondary beams using beam dividers and benders. All guides are curved and except for neutron guide NL2a their length of direct sight ends already in the casemate in order to minimize background radiation in the neutron guide hall. The short direct sight is achieved by small radii of curvature, but the loss of low wavelength neutrons of the spectrum is compensated by supermirror coatings with m up to three and/or multichannel guides in the curved sections. The neutron guides are continued in the experimental area of the neutron guide hall to the different experimental positions up to 70 m far from the reactor core. The design of each neutron guide is adapted to the specific instrumental requirements taking advantage of modern techniques like high m supermirror coatings with high reflectivity to optimize transmission and beam divergence or neutron spin selective supermirrors to obtain polarized beams. A compilation of characteristic parameters of the guide system according its present status is given in Table 1.

3. Experimental setup

For the measurements of integral (Φ_{int}) and spectral neutron flux ($\mathrm{d}\Phi/\mathrm{d}\lambda$) as well as the distribution of beam divergence at the end position of the neutron guides, a versatile fully remote controlled time-of-flight (ToF) spectrometer was built. Fig. 3 shows a schematic view of the experimental setup. It consisted of a Gd-coated single disk chopper (disk diameter $\mathrm{d} = 25$ cm, slit width $s = 1.5$ mm, revolution frequency $= 4600$ rpm), a Cd-cladded

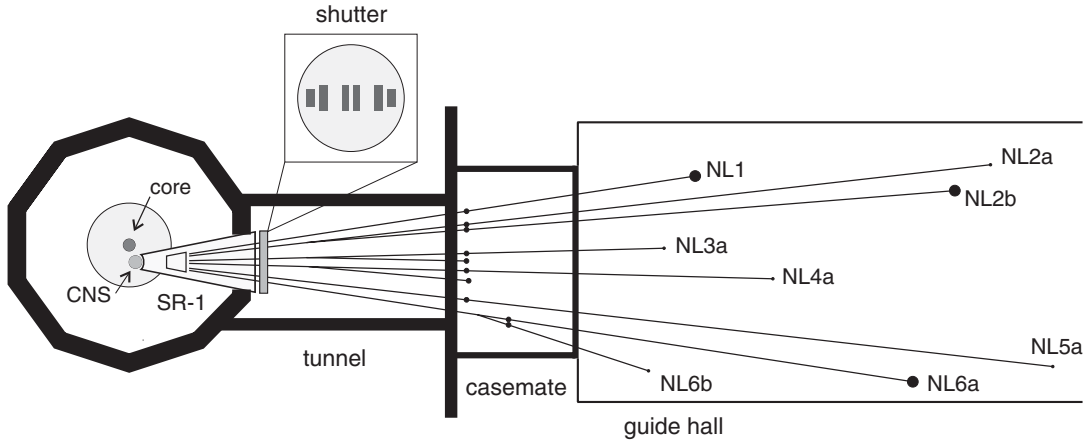

Fig. 2. Schematic view of the cold neutron guide system installed during the commissioning of FRM-II. Six primary neutron guides (NL1–NL6) extract neutrons from the cold neutron source CNS at beam tube SR-1. The inset shows a rear view of the primary beam shutter subsequent to SR-1. Neutron flux and beam divergence were investigated at the indicated end positions of NL1, NL2b and NL6a.

Table 1
Characteristic parameters of the cold neutron guides presently installed in the guide hall of FRM-II: beam cross-section at the end position; critical wavelength λ_{crit}; radius of curvature; total length; supermirror coating and special properties

n-Guide	Width × Height (mm^2)	λ_{crit} (Å)	R_{curv} (m)	Length (m)	SM-coating	Specialty
NL1	60 × 120	1.8	1000	36	$m = 2.5/m = 2$	
NL2a	44 × 100	1.9	2000	60	$m = 2$	s-Shape
NL2b	170 × 12	2.8	400	57	$^{58}Ni/m = 2$	Twisted
NL3a	50 × 116	2.0	460	33	$m = 3/m = 2$	
NL3b	50 × 45	2.4	1500	20	$m = 2/m = 1.2$	
NL4a	50 × 50	3.0	480 (vert) 2100 (horiz.)	56	$^{58}Ni/m = 2$	Vert. s-shape
NL4b	50 × 110	4.7	390	45	$^{58}Ni/m = 2$	
NL5a	29 × 170	1.7	1640	68	$m = 2/m = 2$ pol.	Polarizing
NL6a	60 × 120	2.9	1000	54	$m = 2.2/m = 2/^{58}Ni$	
NL6b	10 × 120	7.6	84	37	$m = 2/^{58}Ni$	VCN

λ_{crit} characterizes the low wavelength cut-off of the transmission of the bent section. VCN: guide for very cold neutrons.

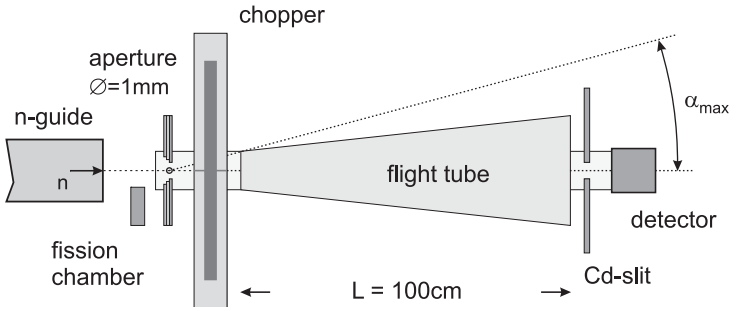

Fig. 3. Schematic view of the experimental time of flight setup to measure the differential neutron flux and beam divergence at the end position of selected neutron guides.

flight tube (length $L = 1\,m$) filled with air and a square shaped ^{3}He-counter ($\square = 2.5 \times 2.5\,cm^2$, length $L = 15\,cm$, ^{3}He-pressure $p = 3.5\,bar$) for neutron detection. The wavelength resolution of the ToF-setup varied from $\Delta\lambda/\lambda \approx 0.01$ to ≈ 0.06 for $\lambda = 10\,Å$ to $\lambda = 1.8\,Å$, respectively.

The entrance aperture of the spectrometer was defined by a hole with diameter $d = 1\,mm$ in a sandwich plate covering the front side of the chopper housing at a distance of 15 mm to the chopper disk. The plate consisted of LiF-tiles, Boron loaded rubber and Cadmium along the neutron propagation and acted as a beam catcher.

At the exit of the flight tube a Cd-slit with variable width ($d = 0.5 - 20$ mm) and a height of $h = 100$ mm was placed in front of the ^{3}He-detector. Chopper, flight tube and detector were mounted on a common step motor driven lever arm rotating horizontally around an axis passing exactly through the entrance aperture.

During flux measurements, the lever arm was continuously swept between $\pm\alpha_{max}$ covering the full divergence of the neutron beam for $\lambda \leqslant 15$ Å. The Cd-slit width was adapted to the particular beam intensity to avoid saturation of the ^{3}He-detector. To study the horizontal beam divergence, the Cd-slit width was set to $d \leqslant 1$ mm corresponding to an angular resolution of $\Delta\alpha \leqslant 0.1^\circ$ and the lever arm was rotated in steps measuring the intensity at various angles. For the measurement of the vertical beam divergence the Cd-slit and detector unit was rotated by 90° and moved vertically on a motor driven linear stage.

A fission chamber detector was mounted in front of the chopper to monitor the incident beam intensity. The fission chamber covered a part of the neutron guide cross-section without influencing the beam passing to the spectrometer. Readout of the detectors and data acquisition were performed with a PC-based multichannel scaler module for ToF-applications, which was developed in the FRM-II detector lab [7]. Furthermore, wavelength dependence of ^{3}He-efficiency and beam attenuation in air and detector wall material were taken into account in the data analysis.

In addition, the integral neutron flux Φ_{int} was measured by standard gold-foil activation via the reaction $^{197}Au(n,\gamma)^{198}Au$ followed by β-decay (half-live $T_{1/2} = 2.69$ days) with subsequent emission of a characteristic 411.8 keV gamma. The foils had a diameter $\varnothing = 11$ mm and a thickness $d = 20\,\mu$m. The exposure time was chosen to achieve an activity 10^4–10^5 Bq, which was measured by a calibrated Ge-spectrometer. The neutron capture cross-section of ^{197}Au for cold and thermal neutrons is proportional to the wavelength λ. Φ_{int} was deduced from the activity data using an average capture cross-section $\langle\sigma\rangle$, which was weighted by the measured spectral neutron flux distribution.

4. Results

4.1. Neutron spectrum of the LD_2-cold source

In addition to the transport properties of the neutron guides, the measured differential neutron spectrum and distribution of beam divergence are strongly determined by the distribution of neutrons emitted by the Cold Source (CNS), which is characterized by the spatially dependent double differential neutron flux density $d^2\phi/d\lambda\,d\Omega$. During the commissioning phase when the reactor power changed by more than two orders of magnitude the operational parameters of the CNS like the amount of liquid deuterium condensed in the CNS-vessel, the D_2-vapour to liquid ratio in the displacer, and the void factor of the boiling liquid due to the heat entry by γ-radiation varied considerably. Best available values for these parameters were used for the *MCNP*-calculations [5] of reactor and CNS to provide a realistic description of the differential flux density in the 25 K cold D_2 moderator of the CNS and at the position of the beam tube nose of SR-1. For liquid deuterium the scattering data sets by Bernnat et al. [8] were employed and an ortho/para ratio of $R = 4:1$ was assumed. For zircalloy, light and heavy water enhanced $S(\alpha,\beta)$ scattering data sets were used.

As an example Fig. 4 shows a schematic view of the CNS for the period when the reactor was operated at ≈ 220 kW. At this condition the displacer still contains liquid deuterium resulting in a deuterium level below the top of the beam tube nose. To illustrate the spacial inhomogeneity of illumination, the beam tube nose of size 135×215 mm^2 has been divided into five equally sized horizontal slabs and Fig. 5 displays the calculated differential neutron flux density within the acceptance of SR-1 averaged over each

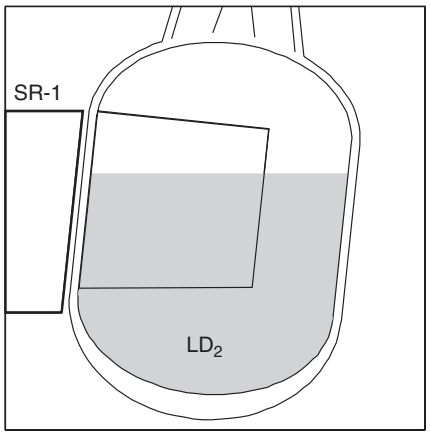

Fig. 4. Schematical cross-section of the CNS filled with 12.91 deuterium when the reactor is operated at ≈ 220 kW. The displacer is still filled with liquid D_2.

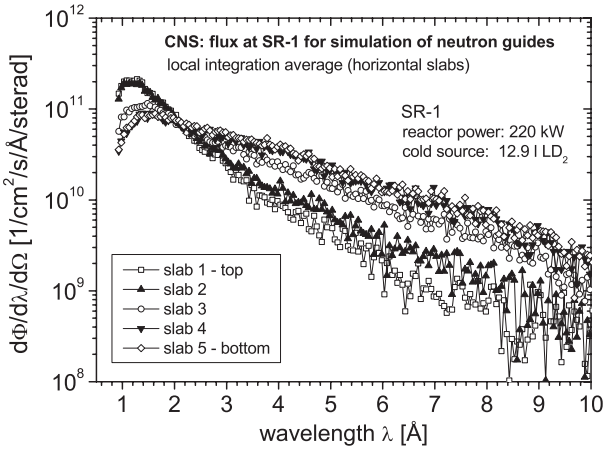

Fig. 5. Simulated differential neutron flux density at the nose of beam tube SR-1 during the 220 kW commissioning period of FRM-II for neutrons with the momentum pointing into SR-1. The rectangular nose window has been divided into five horizontal slabs. The shown distribution of the flux density is averaged for each slab.

slab. Passing from top of the beam tube nose (slab 1) to the bottom (slab 5) the differential flux density varies considerably and turns from a thermal-like to a cold neutron spectrum. To provide a proper input source for the *McStas* neutron transport calculations [6] the area of the beam tube nose was divided into an array of 5×5 pixels. For each pixel the averaged differential flux density was extracted from the data and fitted by an analytical function based on three Maxwellians. A modified version of the *McStas* component *Source_gen* was used, which reads in the intensity and temperature parameters of the Maxwellians for each pixel, totally 150 values. In the simulation, *Source_gen* generates neutrons of random wavelength, start position and emittance angle. Dependent on the wavelength, an intensity is assigned, which is calculated from the Maxwellian functions of the corresponding pixel.

4.2. Measurements at ^{58}Ni-coated neutron guide NL6a

The primary guide NL6 has an initial cross-section $60 \times 120\,\mathrm{mm}^2$. To optimize transmission and length of direct sight, the curved section of NL6 is coated with a combination of ^{58}Ni and supermirrors. At a distance of $\approx 26\,\mathrm{m}$ from the CNS, silicon wafers with supermirror coatings are installed in the guide channel reflecting a partial beam into a side-channel (NL6b, $10 \times 120\,\mathrm{mm}^2$) to supply the instrument MIRA with very cold neutrons ($\lambda \geqslant 8\,\text{Å}$). The main guide is continued as a straight guide (NL6a) to the back-scattering spectrometer SHPERE having ^{58}Ni-coating at all sides. The measurements at NL6a were performed in April 2004 when the reactor was operated at $\approx 220\,\mathrm{kW}$ and the filling of the cold source ($\approx 12.9\,\mathrm{l}$) deviated from nominal filling (15 l). The ToF-spectrometer was mounted directly behind the vacuum window at the end of NL6a, centered at the beam axis in about 54 m distance to the CNS.

4.2.1. Flux measurements at NL6a

The spectral neutron flux density $\mathrm{d}\Phi/\mathrm{d}\lambda$ measured at the exit of NL6a is shown in Fig. 6. In the wavelength region of interest ($1.2\,\text{Å} < \lambda < 15\,\text{Å}$), the relative statistical error is less than 4.5% and thus, error bars have been omitted. Besides an overall smooth distribution the curve reveals a fine structure of several dips, which can be attributed to Bragg edges of the materials, which neutrons have to pass through [9]. The prominent dip at $\lambda \simeq 4.05\,\text{Å}$ originates from aluminium (Al[200]), which is used for the CNS moderator cell ($d \simeq 2\,\mathrm{mm}$), the beam tube nose ($d \simeq 6\,\mathrm{mm}$) and the vacuum windows ($d \simeq 2\,\mathrm{mm}$) of the neutron guide. The dip at $\lambda \simeq 5.15\,\text{Å}$ is probably due to zirconium, which is contained in the vacuum tube of the CNS being built of zircalloy. The integration over the spectral flux density results in an integral neutron flux at 220 kW reactor power of $\Phi_{\mathrm{int}} = 3.2 \times 10^7\,\mathrm{n/cm^2/s}$ at the exit of NL6a.

In Fig. 6 the experimental results are compared with *MCNP*/*McStas* calculations. No scaling is applied to the data. The general features of the measured spectral

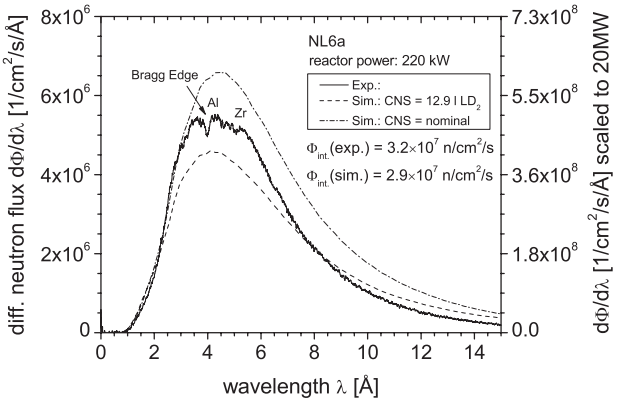

Fig. 6. Measured (solid line) and calculated (dashed line) differential neutron flux density at the end position of neutron guide NL6a at $\approx$ 220 kW reactor power and the CNS filled with 12.9 l deuterium (left scale). On the right scale the data are extrapolated to 20 MW reactor power. A calculation with the CNS being operated in nominal conditions at 20 MW is shown (dash dotted line) for comparison.

distribution like integral flux, cutoff-wavelength and position of the flux maximum can be reasonably described. However, there is a clear discrepancy in the shape of the distributions with the flux density of cold neutrons ($\lambda \geqslant 6.5\,\text{Å}$) being overestimated in the calculations. This discrepancy might be due to various reasons: (i) finite accuracy of the assumptions for operational parameters of the *MCNP* model; (ii) approximation of the neutron distribution at the interface between *MCNP* and *McStas*; (iii) implementation of the supermirror coated silicon wafers installed in the guide into *McStas*.

To estimate the attainable flux at 20 MW reactor power we performed calculations assuming the CNS being operated with complete D_2-filling at nominal conditions, e.g. the displacer is filled with D_2-vapour. These predict a maximum integral neutron flux density of $\Phi_{\mathrm{int}} = 3.3 \times 10^9\,\mathrm{n/cm^2/s}$ at the exit of NL6a. For comparison, the result of the calculations is included in Fig. 6.

4.2.2. Beam divergence at NL6a

In general, the distribution of beam divergence at the end of a neutron guide is determined by its reflective coating, which is characterized by the reflectivity and the critical angle of reflection $\Theta_{\mathrm{crit}}(\lambda)$. Originally, $\Theta_{\mathrm{crit}}(\lambda)$ is reserved for the edge of total reflection, but it is common to use this expression also to describe the range of supermirror reflectivity. Furthermore, the dependence of Θ_{crit} on the coating and the neutron wavelength is usually described by the equation

$$\Theta_{\mathrm{crit}}(\lambda) = 0.1^\circ/\text{Å} \times m \times \lambda. \quad (1)$$

The prefactor $0.1^\circ/\text{Å}$ represents the critical angle of natural Ni and m defines the reflectivity range of the specific coating normalized to the critical angle of natural Ni. For ^{58}Ni the regime of total reflection extends to $m = 1.2$ and has a reflectivity $\approx 99.5\,\%$. Neglecting geometry effects due to the bending, the beam divergence of a guide coated with

^{58}Ni is expected to have a flat intensity distribution within the boundaries $\pm\Theta_{crit}(\lambda)$ even for the 54 m long guide NL6a with many reflections of the neutrons.

The horizontal beam divergence measured with respect to the beam axis is displayed in Fig. 7 for selected wavelengths ($\Delta\lambda/\lambda = \pm 5\%$). The widths of the distributions correspond well to the critical angle Θ_{crit} of the ^{58}Ni-coating. For wavelengths below or close to the critical wavelength $\lambda_{crit} \simeq 2.9$ Å the curves show a strong angular dependence caused by geometry effects and variation of coating of the single bent section. These structures are fading with increasing wavelength revealing a weak oscillatory structure independent of the wavelength. These oscillations can be attributed to the inclined supermirror coated Si-wafers mounted in the guide that cover only a part of the cross-section and the specific geometrical setup of the ToF-spectrometer in the divergence measurements. The entrance aperture and the detector slit define an optical system that only images a specific region inside the neutron guide. This region varies with increasing angle of observation with respect to the neutron beam axis. Due to the reflecting walls of the neutron guide, the same region is observed at several specific angles with a periodicity determined by the cross-section and the length of the guide. Therefore, a spacial inhomogeneity in the neutron flux density translates into an oscillation in the angular intensity distribution.

Fig. 8(a) shows the vertical beam divergence measured at the exit of NL6a. Again, the widths of the distributions agree well with the critical angle $\Theta_{crit}(\lambda)$. However, the distributions exhibit a pronounced wavelength independent oscillatory structure which is unexpected at the first glance. At a reactor power of ≈ 220 kW and insufficient D_2-filling as present during the experiment, the CNS including its displacer had a level of liquid D_2, which was below the top of the beam tube. This causes a vertically inhomogeneous emittance of the CNS as discussed in Section 4.1 and shown in Fig. 5. Due to the optical conditions of the divergence measurement setup, this inhomogeneity directly translates into an angular oscillation which is also reproduced by the simulation calculations shown in Fig. 8(b).

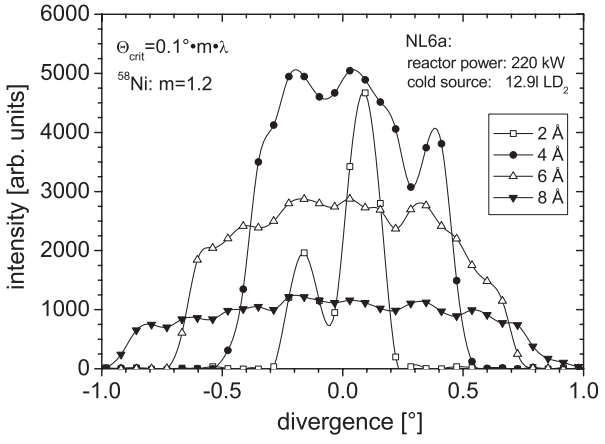

Fig. 7. Horizontal beam divergence on the centre line at the exit of ^{58}Ni-coated neutron guide NL6a measured at ≈ 220 kW reactor power for selected wavelengths. At small wavelengths the distributions show strong angular dependence due to geometry effects of the single bent guide.

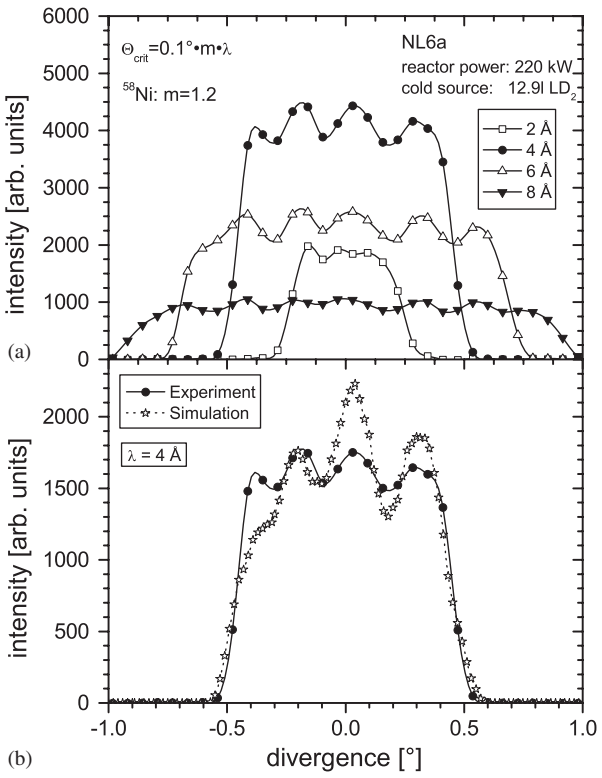

Fig. 8. (a) Vertical beam divergence on the centre line at the exit of ^{58}Ni-coated neutron guide NL6a for selected wavelengths. The pronounced oscillatory structure is caused by the specific experimental conditions at low reactor power when the displacer in the CNS still contains liquid D_2. (b) Comparison of measured and simulated vertical beam divergence at the exit of NL6a for $\lambda = 4$ Å neutrons.

4.3. Measurements at supermirror coated neutron guide NL1

NL1 is a single bent guide with cross-section 60×120 mm^2 and a total length of 36 m. The bent section (20 m) is subdivided into two equally wide channels and has supermirror coatings of $m = 2$ and $m = 2.5$ at the convex and concave walls, respectively. The combination of narrow channels and high m supermirrors at the concave walls account for the envisaged short critical wavelength of $\lambda_{crit} = 1.8$ Å. At the end, a straight single channel section (8 m) with supermirrors $m = 2$ achieves a phase space homogenization and guides the neutrons to the reflectometer for material science N-REX$^+$. The ToF-spectrometer was mounted inside the monochromator shielding of the reflectometer in a few centimeter distance to the vacuum end window of NL1 (≈ 36 m to CNS). It was adjusted to the vertical centre of the guide and could be continuously moved in the horizontal plane lateral to the beam axis by remote control. The measurements were performed at 9.5 MW and 13.5 MW reactor power. In this

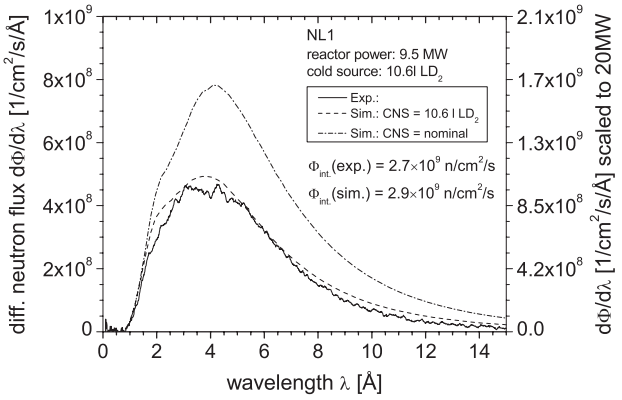

Fig. 9. Measured (solid line) and calculated (dashed line) differential neutron flux density at the end position of neutron guide NL1 at 9.5 MW reactor power and the CNS filled with 10.6 l D_2. On the right scale the data are extrapolated to 20 MW reactor power. A calculation with the CNS being operated in nominal conditions at 20 MW is shown (dash dotted line) for comparison.

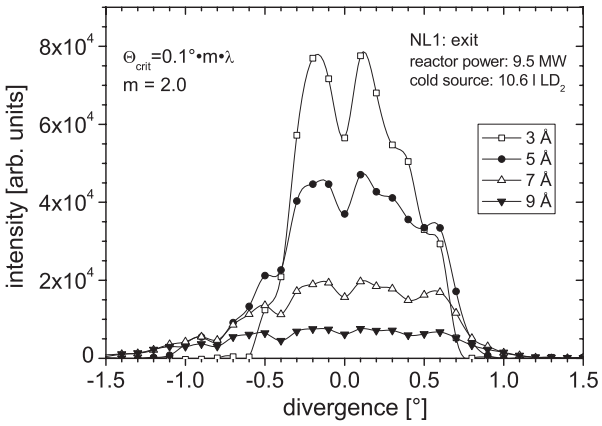

Fig. 10. Horizontal beam divergence on the centre line at the exit of supermirror coated neutron guide NL1 for selected wavelengths. At 0° the setup directly views at the central wall of the bent section causing a dip in intensity.

period the CNS was filled with only 10.6 l D_2, considerably deviating from its nominal filling of 15 l.

4.3.1. Flux measurements at NL1

The spectral neutron flux density $d\Phi/d\lambda$ measured at the centre of the guide at a reactor power of 9.5 MW is shown in Fig. 9. Error bars are omitted as the relative statistical error was less than 5%. The distribution is characterized by the short critical wavelength $\lambda_{crit} = 1.8$ Å and reveals again several dips due to Bragg edges. An integral neutron flux $\Phi_{int} = 2.7 \times 10^9$ n/cm^2/s at 9.5 MW is deduced.

The corresponding simulation calculations based on the given operational parameters of the CNS during the measurement show satisfactory agreement with the measured data regarding integral flux, cutoff-wavelength and position of the flux maximum. However again, there is a systematic over-estimation of the intensity of cold neutrons ($\lambda \geqslant 6.5$ Å) in the calculation. For comparison, the dash dotted curve in Fig. 9 displays the calculated differential flux assuming the CNS operated at nominal conditions and 20 MW power. This calculation predicts an attainable integral neutron flux $\Phi_{int} = 9.8 \times 10^9$ n/cm^2/s.

In addition, the homogeneity of Φ_{int} in the horizontal midplane was proven by moving the ToF-spectrometer perpendicular to the beam and Au-foil activation measurements were performed to determine Φ_{int} independently at two lateral positions. The results are in good agreement and reveal an increase of approximately 25% in flux towards the concave curvature of the single bent guide, which mainly originates from the spacial inhomogeneity at short wavelengths contributing to the distribution of the integral flux.

4.3.2. Beam divergence at NL1

The beam divergence of NL1 is characterized by the supermirror coating ($m = 2$). Unlike ^{58}Ni, a supermirror has a larger maximum reflection angle according Eq. (1), but the reflectivity decreases usually from 99.5% at $m = 1$ to about 88–90% at $m = 2$. The horizontal beam divergence measured on the centre line at the exit of NL1 is displayed in Fig. 10 for selected wavelengths. The boundaries of the distributions correspond well to the critical angle Θ_{crit} for $m = 2$. At large angles the intensity is suppressed due to the reduced reflectivity of the supermirror in combination with the large number of reflections imposed by the narrow channels in the bent section. The dip in intensity appearing in all curves at 0° is due to the direct view to the central wall of the divided section in this setup.

The corresponding vertical beam divergence measured at the exit of NL1 is shown Fig. 11(a). The curves are symmetric and the boundaries are consistent with a supermirror of $m = 2$. The distributions show a pronounced wavelength independent angular oscillation in intensity. Again, the reason is a vertically inhomogeneous illumination of the guide caused by the operation of the CNS with only $\frac{2}{3}$ of the nominal D_2-filling. The measured beam divergence is well reproduced by the simulation calculations shown exemplarily for $\lambda = 5$ Å neutrons in Fig. 11(b).

4.4. Measurements at twisted neutron guide NL2b

The neutron guide NL2b has been specifically designed to deliver cold neutrons with adequate beam cross-section and divergence to the reflectometer *REFSANS* for the study of liquid and biological samples. In order to provide the desired beam geometry, a straight twisted neutron guide is attached to the preceding single bent guide. In the twisted section, the initial beam cross-section of 12 mm width and 170 mm height rotates 90° around the beam centre line on a length of 36 m. [4]. The 170 mm high side walls are coated with ^{58}Ni while the narrow side walls are coated with supermirror $m = 2$. As a result, at the end

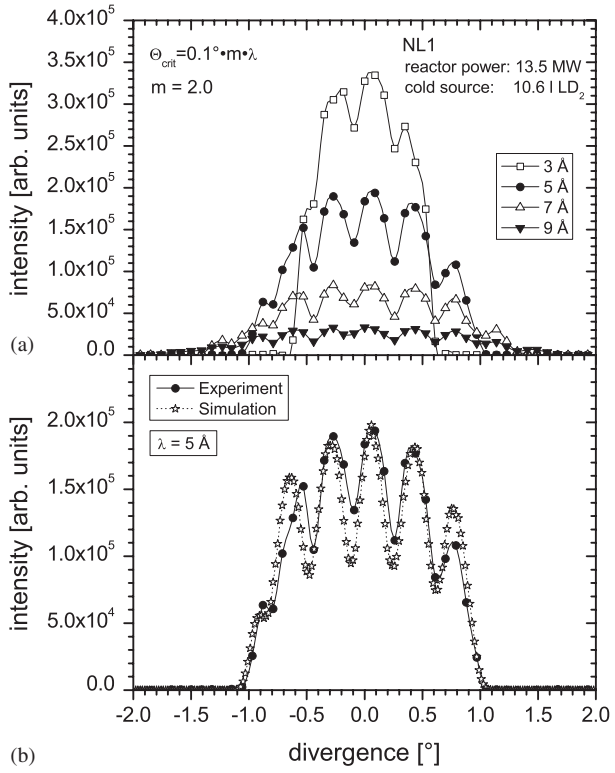

Fig. 11. (a) Vertical beam divergence on the centre line at the exit of super mirror coated neutron guide NL1. The angular oscillation of the intensity is caused by a vertically inhomogeneous illumination of the guide due to the insufficient filling of the CNS. (b) Comparison of measured and simulated vertical beam divergence at the exit of NL1 for $\lambda = 5$ Å neutrons.

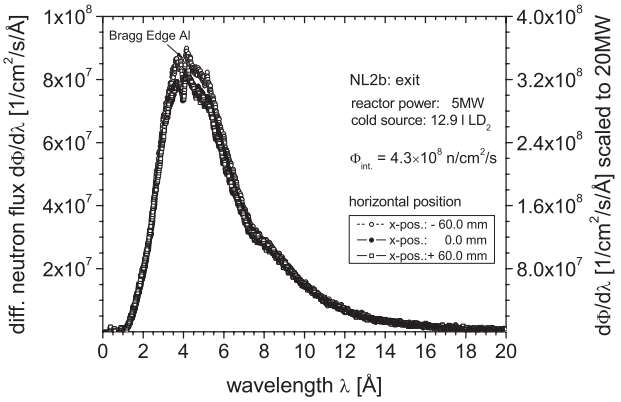

Fig. 12. Differential neutron flux density at the end position of twisted neutron guide NL2b measured at 5 MW reactor power at the centre position ($x = 0$ mm) and the positions $x = \pm 60$ mm in the horizontal plane lateral to the beam axis. The distributions indicate a homogeneous neutron flux along the total width (170 mm) of the guide.

position the guide should exhibit a broad width combined with broad horizontal divergence corresponding to the supermirror coating and a small height combined with small vertical divergence corresponding to the ^{58}Ni-coating.

The reported measurements were performed during the 2 and 5 MW commissioning period of FRM-II with the CNS filled with about 12.91 D_2. The ToF-spectrometer was mounted inside the chopper vessel of *REFSANS* at the end position of NL2b in about 57 m distance to the CNS.

4.4.1. Flux measurements at NL2b

The spectral neutron flux density $d\Phi/d\lambda$ at the beam centre line ($x = 0$ mm) and the positions $x = \pm 60$ mm in the horizontal plane lateral to the beam axis measured at 5 MW reactor power is presented in Fig. 12. In the wavelength region of interest, the relative statistical error was less than 4.5%. The three distributions are rather similar with a small increase in intensity towards the concave curvature of the bent guide. The shapes of the distributions correspond to the critical wavelength $\lambda_{crit} = 2.8$ Å of the bent section and show the prominent Bragg-edge of aluminium. The integrated total flux Φ_{int} varies from 4.2×10^8 to 4.5×10^8 n/cm^2/s at 5 MW. This is confirmed by Au-foil activation measurements performed independently at positions $x = 0$ mm and $x = \pm 45$ mm. An extrapolation to 20 MW reactor power predicts an integral neutron flux $\Phi_{int} \simeq 1.7 \times 10^9$ n/cm^2/s at the entrance of the focussing neutron optics of the reflectometer.

At present, the experimental results cannot be compared to simulation calculations based on *MCNP* and *McStas*, as there exists no proper implementation of the "twist" of the guide in the *McStas* code yet.

4.4.2. Beam divergence at NL2b

The distribution of beam divergence was measured at 1.6 and 1.8 MW reactor powers at the positions $x = 0$ mm and $x = \pm 60$ mm in the horizontal midplane at the exit of NL2b. Fig. 13 shows the horizontal beam divergence for selected wavelengths. All distributions are centered at 0° and the boundaries correspond to the envisaged critical angle $\Theta_{crit}(\lambda)$ of a supermirror with $m = 2$ (see Section 4.4). At the positions $x = \pm 60$ mm, the distributions show pronounced dips in intensity at certain angular positions independent on the wavelength. These dips may be attributed to geometry effects but detailed simulations would be required for a final explanation. At $x = +60$ mm, data points are missing for $\alpha \geqslant 1.3°$ due to an early shutdown of the reactor.

The corresponding distributions of the vertical beam divergence are shown in Fig. 14. As envisaged, the intensity is concentrated within a narrow band of beam divergence. However, the width of divergence is significantly smaller than expected for a ^{58}Ni coating. At large angles the intensity appears to be suppressed, but the beam divergence extends to the boundaries given by the critical angle of ^{58}Ni. Moving from left to right in the horizontal plane lateral to the beam axis, the curves show a systematic shift of the centre of the distributions. This could indicate an incomplete rotation of the phase space of the neutrons by less than 90°.

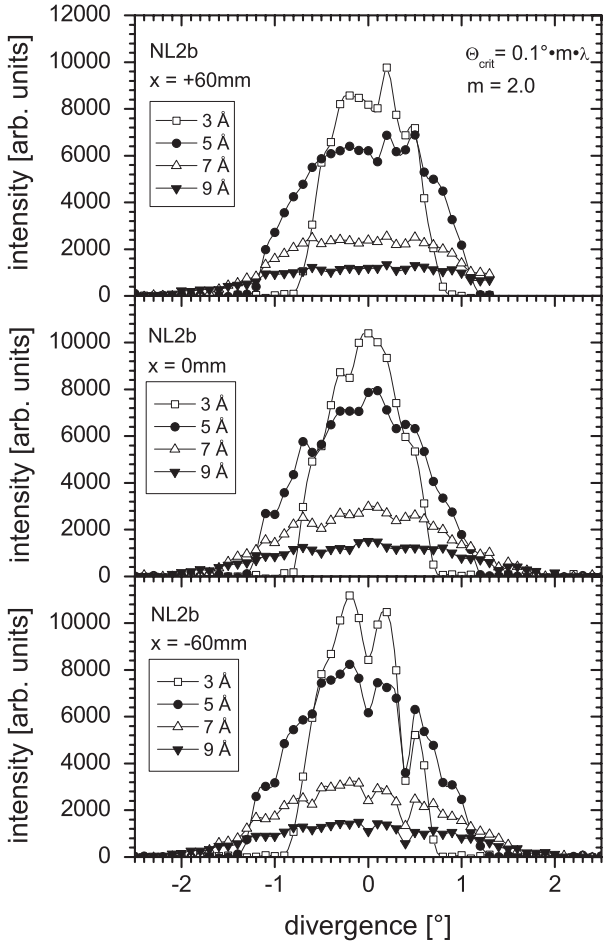

Fig. 13. Horizontal beam divergence measured at 1.6 MW reactor power at the exit of 170 mm wide twisted neutron guide NL2b at centre position ($x = 0$ mm) and $x = \pm 60$ mm in the horizontal plane lateral to the beam axis. The boundaries of the distributions centered at 0° correspond to a supermirror of $m \simeq 2$.

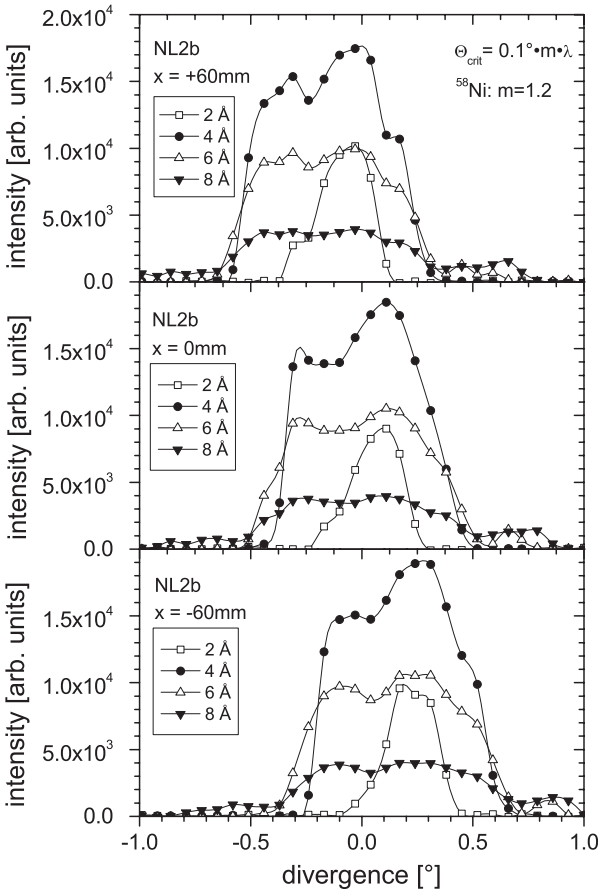

Fig. 14. Vertical beam divergence measured at 1.8 MW reactor power at the exit of 170 mm wide twisted neutron guide NL2b at centre position ($x = 0$ mm) and $x = \pm 60$ mm in the horizontal plane lateral to the beam axis.

4.5. Summary

During the commissioning of FRM-II, the spectral neutron flux density $d\Phi/d\lambda$ as well as the distribution of horizontal and vertical beam divergence have been studied at the exit of two cold neutron guides representing a "standard" ^{58}Ni-guide and a guide taking advantage of advanced supermirror coating. The investigated guides provide high neutron fluxes and reveal good quality with respect to reflective coatings and installation precision.

The experimental results can be compared to detailed Monte Carlo calculations taking into account available data on the operational conditions of reactor and CNS during the measurements. The calculations are in reasonable agreement regarding the characteristics of the measured distributions. An explanation for the systematic discrepancy between measured and computed intensities of cold neutrons requires further examination. Nevertheless, the present results allow reasonable predictions for the cold neutron guides not accessible or yet to be installed.

In addition, the performance of the unique twisted guide was studied. The measurements show that the phase space of the neutrons at the end position of the guide has the desired shape, i.e. a broad width combined with large horizontal divergence and a small height with narrow vertical divergence. This indicates a rotation of the phase space in the twisted section. An unambiguous quantification of the transmission of the twisted section requires the information about the neutron flux at its entrance, which is not accessible to a direct measurement. Detailed interpretations of the experimental results might be obtained from future Monte Carlo simulations based on a complete modelling of the twisted guide.

Acknowledgements

The authors would like to thank all the numerous colleagues that contributed to the work presented. Special thanks go to the FRM-II Radiation Safety Department, in particular to S. Wolff for the assistance in the Au-foil activation measurements. In addition, we would like to greatly thank E. Steichele for his suggestions and the fruitful discussions during the measurement campaign.

References

[1] W. Petry, At. World 48 (5) (2003) 315.
[2] E. Gutsmiedl, et al., in: Proceedings of the International Symposium on Research Reactor and Neutron Science, Daejeon, Korea, 2005, p. 587.
[3] W. Gaubatz, et al., Physica B 276–278 (2000) 104.
[4] H. Aschauer, et al., Physica B 283 (2000) 323.
[5] MCNP, LANL-Report LA-12625-M, 1993.
[6] K. Lefmann, et al., Physica B 276–278 (2000) 152.
[7] K. Zeitelhack, et al., Annual Report ZWE FRM-II, 2003, pp. 6–7.
[8] W. Bernnat, et al., in: Proceedings of the International Conference on Nuclear Data for Science and Technlogy, Mito, Japan, 1988, p. 477.
[9] W. Wagner, et al., J. Neutron Res. 6 (1998) 249.

Available online at www.sciencedirect.com
ScienceDirect
Physica B 385–386 (2006) 1161–1163

PHYSICA B
www.elsevier.com/locate/physb

Horizontal ToF-neutron reflectometer REFSANS at FRM-II Munich/Germany: First tests and status

R. Kampmann[a,*], M. Haese-Seiller[a], V. Kudryashov[a], B. Nickel[b], C. Daniel[c], W. Fenzl[b], A. Schreyer[a], E. Sackmann[c], J. Rädler[b]

[a]GKSS-Forschungszentrum Geesthacht GmbH, D-21502 Geesthacht, Germany
[b]Lehrstuhl für Experimentelle Physik/Biophysik, Sektion Physik, Ludwig-Maximilians-Universität, D-80539 München, Germany
[c]Physik-Department E22, TU-München, D-85748 Garching, Germany

Abstract

The horizontal reflectometer REFSANS at FRM-2 in Munich/Germany has successfully been put into operation. It is dedicated to the comprehensive analysis of the air/water interface by means of specular and off-specular reflectivity as well as GISANS measurements [1,2]. In parts, novel components concerning the chopper system, the neutron optics, the detector and the data acquisition system have been developed to meet the requirements of the basic demands on REFSANS. An overview of the status of REFSANS as achieved in 2005 is presented.

Keywords: Neutron reflectometer; Specular and off-specular reflectivity; GISANS

1. REFSANS and its main components

High demands have been made on REFSANS; these are to provide excellent conditions for (i) specular reflectivity, (ii) grazing incidence (GI-)-SANS and (iii) to allow of performing comprehensive investigations on the air/water interface for biological applications [1,2]. REFSANS is expected to meet these demands due to its novel and expensive design as a ToF-reflectometer (Fig. 1).

REFSANS starts with the chopper chamber in which the slave chopper (SC) can be positioned in neutron guide gaps at distances between ~5 cm and ~2.1 m from the master chopper (MC). Both choppers have double discs to adjust the transmission window between 0° and 120° (Fig. 2). They are operated with windows of equal height and the SC opens at the time t_0 when the MC closes with the result that at t_0 the neutron guide between both choppers is filled with neutrons with wavelengths $\lambda<\lambda_0$ [3]. The latter can be chosen by adequate setting of the chopper window and the rotation speed of both choppers. For $\lambda<\lambda_0$ the wavelength resolution is $\Delta\lambda/\lambda\sim d_{MC,SC}/d_{C,Det}$ where $d_{MC,SC}$ and $d_{C,Det}$ denote the distances between MC and SC and that from the centre between them are the detector [3]. This expensive design (Fig. 2) is needed to meet the demands of specular reflectivity and of GI-SANS comprising high and low λ-resolution.

Neutron guide elements of REFSANS as well as their mechanical support in the chopper are in the beam guide chamber are designed for realizing very different beam geometries. Standard reflectivity measurements are performed with a horizontally slit height-smeared beam and incidence angles of the primary beam of $\pm$3, 12 and 48 (main beam settings; Fig. 1). The beam may be guided towards the sample surface from the air or through the substrate [1,2].

GISANS geometry demands to collimate the beam horizontally and vertically. In this geometry the intensity can strongly be increased by means of focusing 13 partial beams in the detector plane at a distance of ~9 m from the sample (Fig. 3). This focusing is performed by means of pre-collimating the beams in radially collimating neutron guide channels in the chopper chamber (NGE-3 and -4 in

*Corresponding author. Tel.: +49 0 4152 87 1316; fax: +49 0 4152 874 1316.
E-mail address: reinhard.kampmann@gkss.de (R. Kampmann).

0921-4526/$ - see front matter © 2006 Published by Elsevier B.V.
doi:10.1016/j.physb.2006.05.399

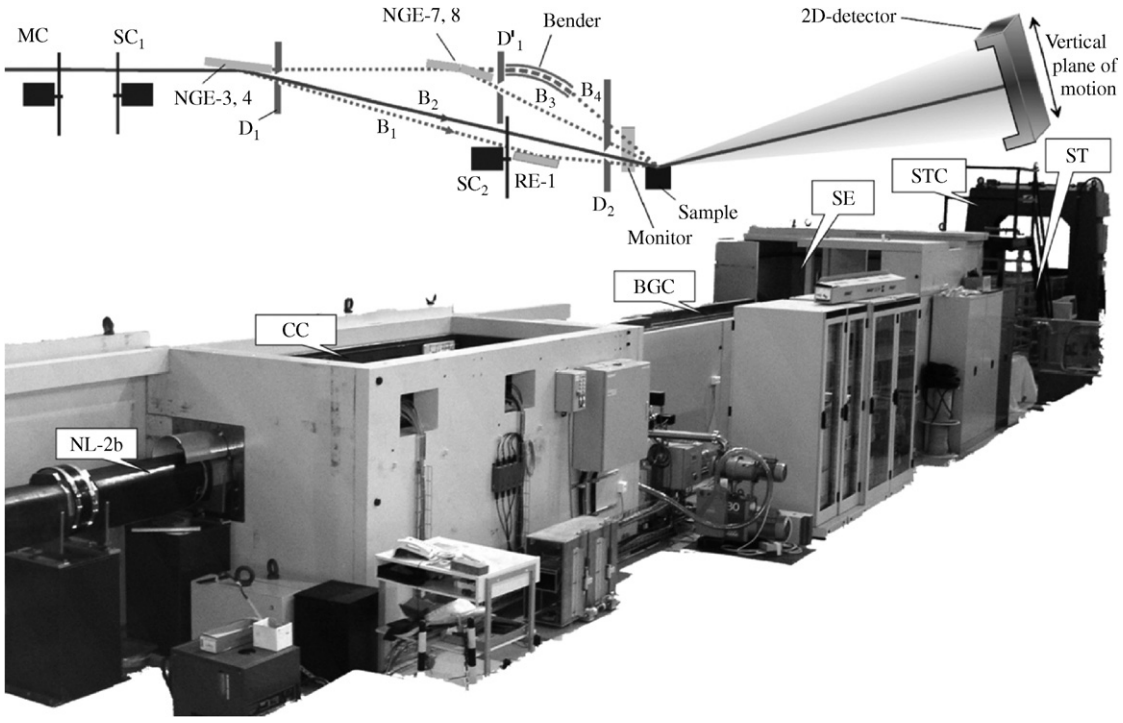

Fig. 1. The photo shows the tilted neutron guide NL-2b and REFSANS with its main components (CC and BGC: chopper and beam guide chamber; SE: sample environment; ST and STC: scattering tube and its crane). Covers and upper shieldings of the CC and the BGC are dismounted. Schematics of the chopper and main beam guides of REFSANS are shown in the upper chart.

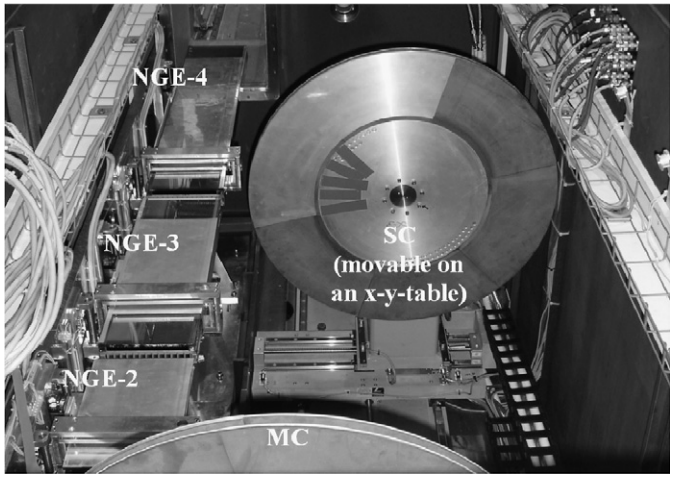

Fig. 2. View of neutron guide elements (NGE), master chopper and slave chopper in the chopper chamber.

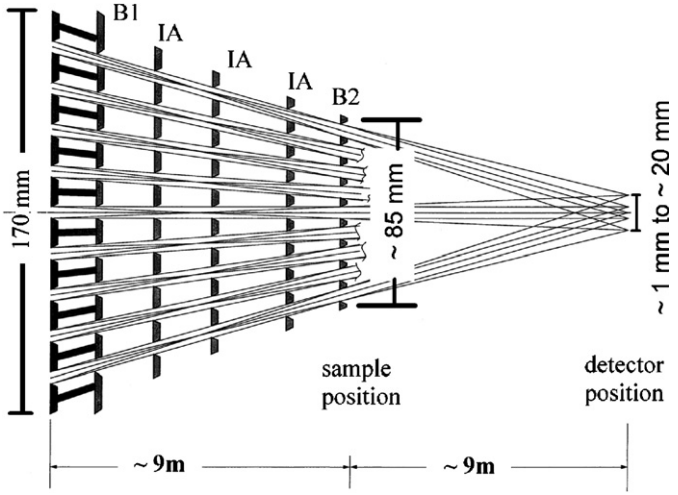

Fig. 3. Schematic view of the horizontal focusing of up to 13 beams in the detector plane. The beam is pre-collimated in the radial collimator (lower channels in the 0.6 and 1 m long NGE-3 and 4; see Fig. 2). In the beam guide chamber comb-like interim diaphragms (IA) are moved between NGEs in the beam to keep the partial beams separated before they pass the sample at ~9 m from the beginning of NGE-3.

Fig. 2) and by comb-like apertures which can be moved into the beam in between of neutron optical bodies (Fig. 3 and 4) preventing mixing of neutrons in different partial beams.

The sample environment is designed for experiments at the air/water interface as well as at the air/solid and liquid/solid interfaces. In all cases one can make use of a microscope in upright or inverted position either for preparation purposes or as a complementary measuring option (e.g. fluorescence techniques). The further equipment consists of a damping table, a temperature controlled film balance and a set of translational tables (x, y, z) together with a three-axis goniometer (X, Φ, Ω).

A 2D-position sensitive area detector with an active area of 500×500 mm and a position resolution of $\sim 2 \times 3$ mm has successfully been put into operation. With its high quantum efficiency for neutrons (~80% for $\lambda \sim 0.8$ nm) and a very low one for gammas ($< 10^{-6}$ for $E \sim 660$ keV) the

Fig. 4. View of neutron optical bodies (NOB) ready for being mounted into the beam guide chamber (NGE, UC and LC: neutron guide element and its upper (UC) or lower channel (LC); GFC: guide field coil; IA: interim aperture).

detector meets all requirements for measuring low reflectivity and weak GISANS contributions [4]. A new data acquisition based on the P7888 card from FAST ComTec GmbH has been developed and successfully tested for the delay-line-based 2D-detector. It allows maximum count rates of $\sim 10^6$ n/s and will significantly improve the performance of REFSANS for the case of fast time-dependent reflectivity measurements and special SANS investigations.

In the scattering tube the 2D-detector can be positioned at distances between ~2 and ~12 m from the sample. For positioning the detector at optimum height a special crane has been developed which allows aligning the scattering tube such that the specularly reflected beam passes its center for incidence angles between ~0 and −100 mrad (Fig. 1).

2. Current status

REFSANS has successfully been put into operation, all components (chopper system, neutron optics, sample environment, 2D-detector, shielding, scattering tube with lifting system and data acquisition system) meet or even surpass their requirements. Test beams have already been guided to the sample demonstrating that the shielding is sufficiently thick. First measurements will be performed at REFSANS in spring 2006 after repairing of some broken elements of neutron guide NL-2b.

Acknowledgements

The great contribution of the technical department of GKSS to constructing and manufacturing of REFSANS components is gratefully acknowledged. The development of REFSANS has been supported by the German Federal Ministry of Education, Research and Technology (BMBF) under contracts 03-KA5FRM-1 and 03-KAE8X-3.

References

[1] R. Kampmann, M. Haese-Seiller, M. Marmotti, J. Burmester, V. Deriglazov, V. Syromiatnikov, A. Okorokov, F. Frisius, M. Tristl, E. Sackmann, Appl. Phys. A 74 (2002) 249.
[2] R. Kampmann, M. Haese-Seiller, V. Kudryashov, V. Deriglazov, V. Syromiatnikov, M. Tristl, B. Toperverg, A. Okorokov, A. Schreyer, E. Sackmann, Physica B 335 (2003) 274.
[3] A.A. van Well, Physica B 180 & 181 (1992) 959.
[4] R. Kampmann, M. Marmotti, M. Haese-Seiller, V. Kudryashov, Nucl. Instrum. Methods A 529 (2004) 342.

Abbreviations

ADP	adenosindiphosphate
ATP	adenosintriphosphate
ATPase	adenosintriphosphatase
CCD	charge-coupled device
COOH	carboxyl group
DMF	dimethylformamide
DMPE	1,2-dimyristoyl-sn-glycero-3-phosphoethanolamine
DNA	desoxyribonucleic acid
F-actin	filamenteous actin
FLIC	Fluorescence Interference Contrast Microscopy
HMM	Heavy Meromyosin
LB	Langmuir-Blodgett
LC	low coverage
NBD	nitro-benzoxadiazole
NHS	N-hydroxysuccinimide
NR	Neutron Reflectometry
OTS (or VTS)	octenyltrichlorosilane
PEG	poly(ethyleneglycol)
RCA	Radio Corporation of America
SAM	Self-assembled monolayer
SOPC	1-stearoyl-2-oleoyl-sn-glycero-3-phosphocholine
XPS	X-ray Photoelectron Spectroscopy
XR(R)	X-ray Reflectometry

Bibliography

[Ahrens et al., 2000] Ahrens, H. Rosleff Baekmark, T., Merkel, R., Schmitt, J., Graf, K., Raiteri, R., and Helm, C.A. (2000). Hydrophilic/Hydrophobic Nanostripes in Lipopolymer Monolayers. *Chemical Physics and Physical Chemistry*, 2, 101–106.

[Albertorio et al., 2005] Albertorio, F., Diaz, A.J., Yang, T., Chapa, V.A. Kataoka, S., Castellana, E.T., and Cremer P.S. (2005). Fluid and Air-Stable Lipopolymer Membranes for Biosensor Applications. *Langmuir*, 21, 7476–7482.

[Almeida et al., 1992] Almeida, P. F. F., Vaz, W. L. C., and Thompson, T. E. (1992). Lateral Diffusion and Percolation in Two-Phase, Two-Component Lipid Bilayers. Topology of the Solid-Phase Domains In-Plane and Across the Lipid Bilayer. *Biochemistry* 31, 7198–7210.

[Atanasov et al., 2005] Atanasov, V., Knorr, N., Duran, R.S., Ingebrandt, S., Offenhäusser, A. Knoll, W. and Köper, I. (2005). Membrane on a Chip: A Functional Tethered Lipid Bilayer Membrane on Silicon Oxide Surfaces. *Biophysical Journal*, 89, 1780–1788.

[Bolze et al., 2002] Bolze, J., Takahasi, M., Mizuki, J., Baumgart, T. and Knoll, W. (2002). X-ray Reflectivity and Diffraction Studies on Lipid and Lipopolymer Langmuir-Blodgett Films under Controlled Humidity. *J. Am. Chem. Soc.,* 124, 9412–9421.

[Bunjes et al., 1997] Bunjes, N., Schmidt, E., Jonczyk, A., Rippmann, F., Beyer, D., Ringsdorf, H., P., G., Knoll, W., and Naumann, R. (1997). Thiopeptide-supported lipid layers on solid substrates. *Langmuir*, 13, 6188–6194.

[Campbell et al., 1999] Campbell, N.A, Reece, J.B., and Mitchell, L.G. (1999). Biology. Benjamin Cummings, 5th edition.

[de Gennes, 1987] de Gennes, P. G. (1987). Polymers at an interface; a simplified view. *Advances in Colloid and Interface Science*, 27, 189–209.

[Dietrich et al., 1997] Dietrich, C., Merkel, R. and Tampe, R. (1997). Diffusion measurement of fluorescence-labelled amphiphilic molecules with a standard fluorescence microscope. Biophysical Journal, 72, 1701–1710.

[Elender et al., 1996] Elender, G., Kühner, M., and Sackmann, E. (1996). Functionalisation of Si/SiO_2 and glass surfaces with ultrathin dextran films and deposition of lipid bilayers. *Biosensors & Bioelectronics*, 11, 565.

[Fick et al., 2004] Fick, J., Steitz, R., Leiner, V., Tokumitsu, S., Himmelhaus, M., and Grunze, M. (2004). Swelling Behavior of Self-Assembled Monolayers of Alkanethiol-Terminated Poly(ethylene glycol): A Neutron Reflectometry Study. *Langmuir*, 20, 3848–3853.

[Gibaud and Hazra, 2000] Gibaud, A. and Hazra, S. (2000). X-ray reflectivity and diffuse scattering. Current Science, 78 (12), 1467–1477.

[Hertrich, 2008] Hertrich, S.O. (2008). Röntgenreflektivitätsmessungen an substratgestützten Membranen. Diploma-Thesis, LMU München.

[Hochrein et al., 2006] Hochrein, M. B., Reich, C., Krause, B., Rädler, J. O., and Nickel. B., (2006). Structure and mobility of lipid membranes on a thermoplastic substrate. *Langmuir*, 22 (2), 538–545.

[Jossinet et al., 1995] Jossinet, J., McAdams, E.T., and Risacher, F. (1995). The Biophysical Interpretation of Tissue Multi-Frequency Loci. *Inov. Tech. Biol. Med.*, 16 (6), 706–716.

[Kern & Puotinen, 1970] Kern, W. and Puotinen, D. (1970). Cleaning solutions based on hydrogen peroxide for use in silicon semiconductor technology. *RCA Review*, 31, 187–206.

[Kiessling and Tamm, 2003] Kiessling, V. and Tamm, L. (2003). Measuring distances in supported bilayers by fluorescence interference-contrast microscopy: Polymer supports and SNARE proteins. *Biophys. J.*, 84, 408–418.

[Knoll et al., 2000] Knoll, W., Frank, C., Heibel, C., Naumann, R., Offenhäuser, A., Rühe, J., Schmidt, E., Shen, W., & Sinner, A. (2000). Functional tethered lipid bilayers. *Review in Molecular Biotechnology*, 74, 137–158.

[Kuhl et al., 1998] Kuhl, T. L., Majewski, J., Wong, J. Y., Steinberg, S., Leckband, D. E., Israelachvili, J. N., and Smith, G. S. (1998). A Neutron Reflectivity Study of Polymer-Modified Phospholipid Monolayers at the Solid-Solution Interface: Polyethylene Glycol-Lipids on Silane-Modified Substrates. *Biophysical Journal,* 75, 2352–2362.

[Li et al., 2002] Li, J. and Horton, J.H. (2002).A scanning probe study of some short chain self-assembled alkylsilane films. *J. Mater. Chem.*, 12, 1268–1273.

[Majewski et al., 2000] Majewski, J., Tony, U., Kuhl, L., Wong, J.Y., and Smith, G.S. (2000). X-ray and neutron surface scattering for studying lipid/polymer assemblies at the air-liquid and solid-liquid interfaces. *Reviews in Molecular Biotechnology,* 74, 207–231.

[Marsh et al., 2003] Marsh, D., Bartucci, R., Sportelli, L. (2003). Lipid membranes with grafted polymers: physicochemical aspects. *Biochimica et Biophysica Acta*, 1615, 33–59.

[Merkel et al., 1989] Merkel, R., Sackmann, E., and Evans, E. (1989). Molecular friction and epitactic coupling between monolayers in supported bilayers. *Journal de Physique II*, 50, 1535–1555.

[Moncelli et al., 1994] Moncelli, M.R., Becucci, L., and Guidelli, R. (1994). The Intrinsic pKa Values for phosphatidylcholine, phosphatidylethanolamine, and phosphatidylserine in monolayers deposited on mercury electrodes. *Biophysical Journal* 66, 1969–1980.

[Moulder et al., 1992] Moulder, J.F., Stickle, W.F., Sobol, P.E., and Bomben, K.D. (1992). Handbook of Photoelectron Spectroscopy. Perkin-Elmer Corporation, Eden Prairie MN, USA.

[Munro et al., 2004]] Munro, J.C. and Frank, C.W. (2004). Adsorption of lipid-functionalized poly(ethylene glycol) to gold surfaces as a cushion for polymer-supported lipid bilayers. *Langmuir*, 20, 3339–3349.

[Nagle et al., 2000]] Nagle, J.F., and Tristram-Nagle, S. (2000). Structure of lipid bilayers. *Biochimica et Biophysica Acta (BBA) - Reviews on Biomembranes*, 1469 (3), 159–195.

[Naumann et al., 2002] Naumann, C., Purrucker, O., Lehmann, T., Rühe, J., Knoll, W., and Frank, C. (2002). The polymer-supported phospholipid bilayer: Tethering as a new approach to substrate-membrane stabilization. *Biomacromolecules*, 3, 27–35.

[Parratt, 1954] Parratt, L. G. (1954). Surface Studies of Solids by Total Reflection of X-rays. *Phys. Rev.,* 95 (2), 359–369.

[Penfold and Thomas, 1990] Penfold, J., and Thomas, R.K. (1990). The application of the specular reflection of neutrons to the study of surfaces and interfaces. *J. Phys.: Condens. Matter*, 2, 1369–1412.

[Pershan, 1994] Pershan, P. S. (1994). X-ray or neutron reflectivity: Limitations in the determination of interfacial profiles. *Phys. Rev. E* 50, 2369–2372.

[Purrucker, 2004] Purrucker, O. (2004). Establishment of a New Plasma Membrane Model with Well-Defined Polymer-Spacer. PhD-Thesis, TU München.

[Reich, 2005] Reich, C. (2005). Structure, Fluidity and Phase Behavior of Supported Lipid Membranes: An Investigation by X-ray Reflectivity and Fluorescence Microscopy, PhD-Thesis, München.

[Reich et al., 2005a] C. Reich, M. B. Hochrein, B. Krause, and B. Nickel (2005). A microfluidic setup for studies of solid-liquid interfaces using x-ray reflectivity and fluorescence microscopy. *Rev. Sci. Instrum.,* 76(9), 95–103.

[Rief et al., 2000] Rief, M., Rock, M.S., Mehta, A.D., Mooseker, M.S., Cheney, R.E. and Spudich, J.A (2000). Myosin-V stepping kinetics: A molecular model for processivity. Proc. Natl. Acad. Sci. U S A, 97(17), 9482–9486.

[Sackmann, 1996] Sackmann, E. (1996). Supported membranes: Scientific and practical applications. *Science*, 271, 43–48.

[Sackmann & Tanaka, 2000] Sackmann, E. and Tanaka, M. (2000). Supported membranes on soft polymer cushions: Fabrication, characterization and application. *Trends Biotechnol.* 18(2), 58–64.

[Sackmann & Merkel, 2010] Sackmann, E and Merkel, R. (2010). Lehrbuch der Biophysik. Wiley VCH.

[Seifert et al., 2006] Merath, R.-J. and Seifert, U. (2006). Nonmonotonic fluctuation spectra of membranes pinned or tethered discretely to a substrate. *Am. Phys. Soc. / Physical review* E 73, 1–4.

[Seitz et al., 2000] Seitz, M., Ter-Ovanesyan, E., Hausch, M., Park, C. K., Zasadzinski, J. A., Zentel, R., & Israelachvili, J. N. (2000). Formation of tethered supported bilayers by vesicle fusion onto lipopolymer monolayers promoted by osmotic stress. *Langmuir*, 16, 6067–6070.

[Shen et al., 2001] Shen, W., Boxer, S., Knoll, W., and Frank, C. (2001). Polymer-supported lipid bilayers on benzophenone-modified substrates. *Biomacromolecules*, 2, 70–79.

[Wagner et al., 2000] Wagner, M. and Tamm, L. (2000). Tethered polymer-supported planar lipid bilayers for reconstitution of integral membrane proteins: Silanepolyethyleneglycol- lipid as a cushion and covalent linker. *Biophysical Journal*, 79(3), 1400–1414.

[Wong et al. 1999] Wong, J. Y., Majewski, J., Seitz, M., Park, C. K., Israelachvili, J. N., & Smith, G. S. (1999). Polymer-cushioned bilayers. I. A structural study of various preparation methods using neutron reflectometry. *Biophysical Journal*, 77, 1445–1457.

Publications

[Daniel et al., 2007] Daniel, C., Sohn, K.E., Mates, T.E., Kramer, E.J., Rädler, J.O., Sackmann, E. Nickel, B. Andruzzi, L. (2007). Structural characterization of an elevated lipid bilayer obtained by stepwise functionalization of a self-assembled alkenyl silane film. American Vacuum Society, Biointerphases, 2 (3), 109–118.

[Kampmann et al., 2006] Kampmann, R., Haese-Seiller, M., Kudryashov, V., Nickel, B., Daniel, Ch., Fenzl, W., Schreyer, A., Sackmann, E., Rädler, J. (2006). Horizontal ToF-neutron reflectometer REFSANS at FRM-II Munich/Germany: First tests and status. *Physica,* B 385–386, 1161–1163.

[Zeitelhack et al., 2006] Zeitelhack, K., Schanzer, C., Kastenmüller, A., Röhrmoser, A., Daniel, C., Franke, J., Gutsmiedl, E., Kudryashov, V., Maier, D., Päthe, D., Petry, W., Schöffel, T., Schreckenbach, K., Urban, A., Wildgruber, U. (2006). Measurement of neutron flux and beam divergence at the cold neutron guide system of the new Munich research reactor FRM-II. *Nuclear Instruments and Methods in Physics Research A,* 560, 444–453.

[Kampmann et al., 2004] Kampmann, R., Haese-Seiller, M., Kudryashov, V., Deriglazov, V., Tristl, M., Daniel, Ch., Toperverg, B., Schreyer, A., Sackmann, E. (2004). The potential of the horizontal reflectometer REFSANS/FRM-II for measuring low reflectivity and diffuse surface scattering. *Physica B,* 350, e763–e766.

Acknowledgements

Danke
an alle die zum Gelingen dieser Arbeit beigetragen haben:

- Prof. Dr. Erich Sackmann, der sich ohne zu zögern mit mir auf die Promotionsreise begeben hat. Es war eine schöne Reise und ich hab mich gerne von seiner Begeisterung für Neues angesteckt.
- Prof. Joachim Rädler, Dr. Bert Nickel und Dr. Luisa Andruzzi für viele interessante Diskussionen und die herzliche Aufnahme in ihren Arbeitsgruppen während meiner Zeit an der Ludwig Maximilians Universität.
- Reinhard Kampmann, Martin Haese-Seiller und insbesondere Dr. Valery Kudryashov für die Geduld und Ausdauer während des Aufbaus von REFSANS am Forschungsreaktor.
- Christian Reich, Kirstin Fritz, Dr. Kheya Sengupta, Dr. Laurent Limozin, Matthias Tristl für all die schönen Messzeiten.
- Zhang Junshan für die lehrreiche Unterstützung bei den Experimenten mit Motorproteinen, Dr. Michael Bärmann, Hulda Kirpal, Monika Rusp und Rudi Lehrhuber ohne deren Hilfe der experimentelle Alltag bei E22 sicher nicht so rund abgelaufen wäre.
- Den Mitarbeitern der mechanischen und elektronischen Werkstätten am Reaktor und der Fakultät sowie des Kristalllabors für das erfolgreiche Miteinander.
- Allen anderen bei E22 inklusive den Tanaka und Bausch Leuten für die gute Zusammenarbeit und die schöne Stimmung am Lehrstuhl, nach der Arbeit und nicht zuletzt auf der Winterschule.

Besonders will ich Tina danken, die in all der Zeit immer hinter mir gestanden ist, und auch meinem kleinen Sohn Milan, der dabei brav mitmachte.